GEOLOGICA ULTRAIECTINA

Mededelingen van de
Faculteit Aardwetenschappen
Universiteit Utrecht

No. 191

Surface deformation resulting from subduction and slab detachment

Susanne J. H. Buiter

GEOLOGICA ULTRAIECTINA

Mededelingen van de
Faculteit Aardwetenschappen
Universiteit Utrecht

No. 191

Surface deformation resulting from subduction and slab detachment

Susanne J. H. Buiter

Surface deformation resulting from subduction and slab detachment

Beweging en vervorming van het aardoppervlak ten gevolge van subductie en afbreken van gesubduceerde lithosfeer

(met een samenvatting in het Nederlands)

PROEFSCHRIFT

TER VERKRIJGING VAN DE GRAAD VAN DOCTOR
AAN DE UNIVERSITEIT UTRECHT
OP GEZAG VAN DE RECTOR MAGNIFICUS, PROF. DR. H.O. VOORMA,
INGEVOLGE HET BESLUIT VAN HET COLLEGE VOOR PROMOTIES
IN HET OPENBAAR TE VERDEDIGEN
OP MAANDAG 22 MEI 2000 DES OCHTENDS TE 10:30 UUR

DOOR

Susanne Janita Henriët Buiter

Geboren op 30 juli 1970, te Meppel

Promotor: Prof. Dr. M.J.R. Wortel
Co-promotor: Dr. R. Govers

The research described in this thesis was carried out at the Faculty of Earth Sciences, Utrecht University, Budapestlaan 4, 3584 CD Utrecht, the Netherlands. The investigations were supported by the Netherlands Geosciences Foundation (GOA/ALW) with financial aid from the Netherlands Organisation for Scientific Research (NWO).

ISBN 90-5744-048-2

En Johannes vroeg ook dikwijls, wat hij zag en hoorde.
Veel raadselachtigs. Domme vragen deed hij vaak;
hij vroeg waarom de wereld was zoals zij was,
en waarom dieren en planten dood moesten gaan,
en of er wonderen konden gebeuren.

Frederik van Eeden, De kleine Johannes

Contents

Chapter 1

General introduction

1.1 Motivation

Convergence of lithospheric plates is accommodated at subduction zones where one plate moves under the other into the Earth's mantle. Subduction leads to characteristic effects measurable at the Earth's surface. For example, mountains and sea-floor depressions mark the location of active plate margins, while deep seismicity delineates the downgoing lithospheric plate. More insight in the relation between a subduction process and its surface effects formed the overall motivation for the research described in this thesis. Knowledge of surface effects, and their magnitudes, which may be expected at active plate margins may help in the interpretation of the geological history of a specific region. Alternatively, surface data contribute to understanding the physics of subduction.

The observables of subduction vary depending on the stage of the subduction process. Three phases can be distinguished during the evolution of a subduction zone system: initiation of subduction, ongoing subduction and the subsequent terminal stage when subduction stops. The focus of this thesis lies on the phases of ongoing subduction and on the last stages of a subduction process.

The topography of the Earth's surface at a convergent plate margin reflects the surface displacements associated with subduction (Fig. 1.1). Changes in a subduction process may lead to variations in this topography. Surface motions may be caused by, for example, variations in driving or resistive forces associated with subduction, erosion, sedimentation, and variations with time in the strength of the lithospheric plates. The subject of this thesis is the relation between variations in the subduction process and surface displacements which occur at the surface near the convergent plate margin. Using numerical models, the effects of changes in a subduction zone system on surface displacements are quantified. Specific attention is paid to the final stages of subduction when subducted lithosphere may detach from the lithosphere at the surface. This study was inspired by tomographic images of the Mediterranean region [*Spakman et al.*, 1988; *Spakman*, 1990] which show that subducted lithosphere may have become detached at depth. It is expected that slab detachment induces

surface motions at the convergent plate margin [*Wortel and Spakman,* 1992; *Chatelain et al.*, 1992; *Westaway*, 1993]. Signals of the surface motions may be found in the stratigraphy of (former) sedimentary basins near the plate margin. This can provide data sets against which the models can be tested.

1.2 Surface motions at convergent plate margins

In general, an ocean-continent convergent plate margin has a characteristic surface topography with a forebulge, foredeep, accretionary wedge and, possibly, a back-arc basin (Fig. 1.1). As it moves into the mantle the subducting plate is bent. The forebulge is an inherent feature of this plate bending process and generally has a height on the order of several hundreds of meters. The foredeep lies at the contact between the overriding and the subducting lithosphere. This basin is usually filled with sediments which mainly derive from the continent. Therefore, its bathymetry partly depends on sediment supply. As the plate subducts, sediments and upper crust material may be scraped off from the subducting plate and accreted to the overriding plate to form an accretionary wedge. This process can contribute to the formation of a thrust belt on the continental side of the system. Roll-back of the subducting plate, in the direction away from the overriding plate, may lead to extension in the overriding lithosphere and the creation of a back-arc basin. These retreating plate margins generally have lower mountains and a deeper foredeep [*Royden,* 1993].

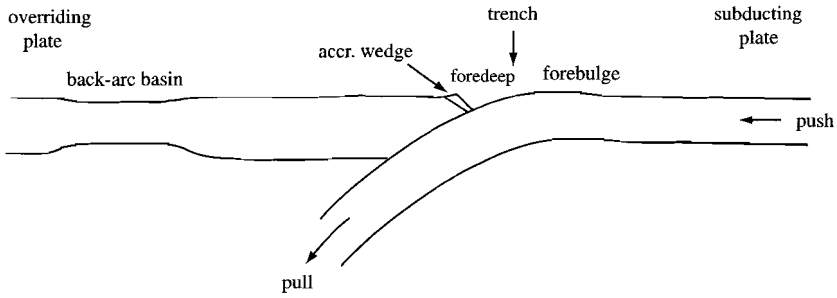

Figure 1.1: Generalised structure of a convergent plate margin.

Evidently, horizontal and vertical motions at convergent plate margins are closely linked. Horizontal convergence velocities of lithospheric plates are on the order of several centimetres per year. Vertical movements are typically an order of magnitude smaller. Rapidly subsiding foredeeps have subsidence rates on the order of 1 mm/yr [e.g. *Audley-Charles*, 1986a; *Doglioni*, 1993]. This velocity consists of a contribution of tectonic origin which is amplified by the loading effect of sediments and water filling the basin. In general, the depth to basement in foredeeps is on the order of a few kilometres. Uplift at a convergent plate margin may reach the same order of magnitude. Examples are an uplift of 5 km for the island of Timor from the Middle Pliocene to present, which implies an average rate of uplift of 1.5 mm/yr [*Audley-Charles,* 1986b], and an uplift of eastern Taiwan of around 5 km since

the Early Pleistocene, which implies an uplift rate of approximately 5 mm/yr [*Lundberg and Dorsey,* 1988; see also *Pirazzoli et al.,* 1993]. In Calabria coastal terraces have been uplifted by 400 to 700 m with rates of 0.7 to 1.0 mm/yr [*Westaway*, 1993; *Cucci and Cinti,* 1998]. Both subsidence and uplift can, therefore, reach magnitudes of several hundreds of meters to even a few kilometres, while rates can vary from less than 0.1 mm/yr up to 0.5 cm/yr.

1.3 Slab detachment

Observations from sites of past and present plate convergence point to the possibility that subducted lithosphere detaches from the lithosphere at the surface. This may occur, for example, after closing of an oceanic basin. In the final stages of subduction, convergence of the lithospheric plates involved will slow down. Subducted lithosphere usually is denser than the surrounding mantle material and, therefore, exerts a pull force that contributes to the continuation of the subduction process. In this stage, the subducted plate is then held back at the Earth's surface, but still experiences a downward directed slab pull force. In such a situation the slab might break off [see also *Yoshioka and Wortel*, 1995]. Failure is likely to occur near the transition between continental and oceanic material [*McKenzie,* 1969; *Davies and Von Blanckenburg,* 1995; *Wong a Ton and Wortel,* 1997]. An example of slab detachment after closure of an ocean can be found in the Siberian region where slab remnants have been identified at depths of 1200 km and deeper [*Van der Voo et al.*, 1999]. Indications for more recent detachment of subducted lithosphere exist, among others, for the New Hebrides Islands, Timor, the Aegean region and Italy [*Chatelain et al.,* 1992; *Price and Audley-Charles*, 1987; *Spakman et al.,* 1988; *Wortel and Spakman,* 1992]. Detachment has been suggested on the basis of a gap in the hypocentra distribution associated with subduction [e.g. *Ritsema,* 1972; *Pascal et al.,* 1973] and from tomographic images [*Oncescu et al.,* 1984; *Spakman et al.,* 1988]. The process of detachment of subducted lithosphere is thought to be associated with distinctive surface effects: 1) vertical and horizontal surface motions [*Wortel and Spakman,* 1992; *Westaway*, 1993; *Davies and Von Blanckenburg,* 1995], 2) changes in stress regime [*Hippolyte et al.,* 1994; *Sorel et al.,* 1988; *Meijer and Wortel,* 1996], and 3) magmatism and metamorphism [*Davies and Von Blanckenburg,* 1995; *Von Blanckenburg and Davies,* 1995]. The observation of such effects can support the interpretation of a detached slab.

Detachment probably will not occur at the same time along all of a subduction zone. *Wortel and Spakman* [1992] formulated a hypothesis in which slab detachment propagates laterally along strike of a convergent plate margin (Fig. 1.2). Not only will the surface effects of detachment migrate along strike of the plate margin for a laterally migrating slab detachment, but the three-dimensional character of the process will also modify the surface signals. This is illustrated in Fig. 1.2. The redistribution of gravitational pull forces results in an along strike migration of a deepening of the foredeep followed by uplift, or rebound.

The hypothesis of lateral migration of slab detachment was inspired by the regional tomographic images of the Mediterranean region by *Spakman et al.* [1988] and *Spakman* [1990], in which gaps are seen in subducted lithosphere below the Apennine, Carpathian and Dinaride/Hellenide mountains. These tomographic images do not form the decisive

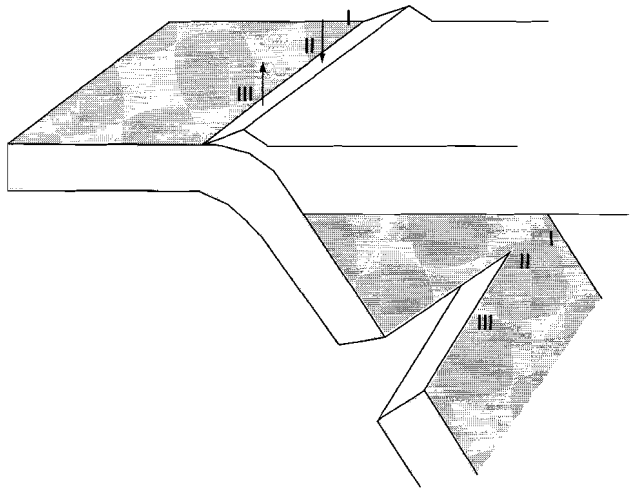

Figure 1.2: Schematic illustration of the process of lateral migration of slab detachment: I) continuous subducting plate, II) tip of the detachment tear, the transfer of slab pull forces from the detached part to the still continuous slab is reflected at the surface by a deeper deflection, III) detached slab, the decrease in slab pull forces leads to an uplift of the surface.

proof that the subducted lithosphere has indeed become detached. For example, *Piromallo and Morelli* [1997] and *Amato et al.* [1998] show a continuous subducted slab below North Italy, whereas the model of *Spakman* [1990] shows a detached slab. An independent support of the hypothesis comes from analyses of stratigraphic data. *Van der Meulen et al.* [1998] found a lateral component in the shift of depocentres (which can be related to the regional deepest deflection) for the Apennines region, which is in agreement with a migrating tear in the subducted lithosphere. A similar lateral shift in depocentres has also been found for the Carpathian region [*Meulenkamp et al.*, 1996]. Here the rate of lateral migration of foredeep depocentres increased from 5.5 cm/yr in the Late Oligocene to 47 cm/yr in the early Middle Miocene.

1.4 Tectonic evolution of the Italian region

The Italian region (Fig. 1.3) is selected as an area for the study of the process of slab detachment. It is expected that the subduction zone system on the eastern side of Italy is in the final stages of its evolution. This is indicated by the lack of subduction-related earthquakes, the low convergence rate between Italy and the Adriatic plate, the continental nature of the Adriatic lithosphere and the observation that the Adriatic plate has almost been subducted completely. In addition, tomographic images of the area [*Spakman*, 1990; *Spakman et al.*, 1993] display evidence for a gap in the subducted lithosphere in the depth range of approximately 150 to 250 km.

Italy lies in the middle of the Mediterranean area where the convergence between the Eurasian and African plates is accommodated. Africa has been moving roughly northward relative to Eurasia since the Middle Cretaceous [*Savostin et al.,* 1986; *Dewey et al.,* 1989], thereby closing the Tethyan ocean in between. Subduction zones developed around Adria (beneath the Apennines, Alps and Dinarides), to the west of Adria along the north coast of Africa, beneath the Carpathians and in the Aegean region. On a large scale the Mediterranean is a convergent area, and, therefore, expected to be in compression. However, several young extensional basins are present (Fig. 1.3): the Provençal (Late Oligocene-Middle Miocene), Tyrrhenian (Middle Miocene-recent) and Southern Aegean (Late Miocene-recent) basins. These are located in the back-arc area of the subduction zones. In the western Mediterranean the Tyrrhenian basin was formed after the Provençal basin. The islands of Corsica and Sardinia form the boundary between both basins. The islands rotated anti-clockwise with the opening of the Provençal basin, but remained at their present location from approximately 16 Ma (transition Early-Middle Miocene) onward [*Dewey et al.,* 1989; *Boccaletti et al.,* 1990b]. The Tyrrhenian basin opened as future Italy rotated anti-clockwise towards the east. Adriatic lithosphere has been subducting westward beneath Italy along a subduction system that is continuous from North Italy to Calabria in the south. Clear evidence for subduction beneath Calabria comes from the distribution of hypocentres of earthquakes that occur down to depths of 500 km [e.g. *Ritsema,* 1972; *Anderson and Jackson,* 1987; *Giardini and Velonà,* 1991] and the calc-alkaline volcanism of the Aeolian islands [*Barberi et al.,* 1973]. A well resolved feature of tomographic images of the region [*Amato et al.,* 1993; *Spakman et al.,* 1993] is the presence of several hundreds of kilometres of subducted lithosphere beneath Calabria and along all of Italy. Forward modelling from surface tectonic reconstructions confirms that the anomalies in the tomographic images correspond with subducted lithosphere [*De Jonge et al.,* 1994]. In this thesis the Tyrrhenian basin is considered as the back-arc basin of the Adriatic subduction zone, opened by the eastward roll-back of the subduction system [e.g. *Boccaletti et al,* 1976; *Malinverno and Ryan,* 1986; *Laubscher,* 1988; *Doglioni,* 1991,1993].

1.5 Modelling

Because geodynamic processes which occur at depth in the Earth can generally not be observed directly, it is difficult to determine the relation between these processes and their surface effects. In this thesis numerical experiments are used to study surface effects of variations in the subduction process. With numerical models more insight in the physics of this process can be obtained through quantification and identification of important parameters and discriminative data. The term model is used here to denote a representation of a physical process. With a model this process is simulated with the aim to study its behaviour, for example, for different material properties or forces. A model is a tool for the interpretation of geological and geophysical data. It can be used to investigate whether a specific process or hypothesis will indeed lead to the kind of data that were measured. Alternatively, model results can be used as an indication of which data are descriptive of a process and should, therefore, be searched for. Modelling can also identify sensitivity of data to various

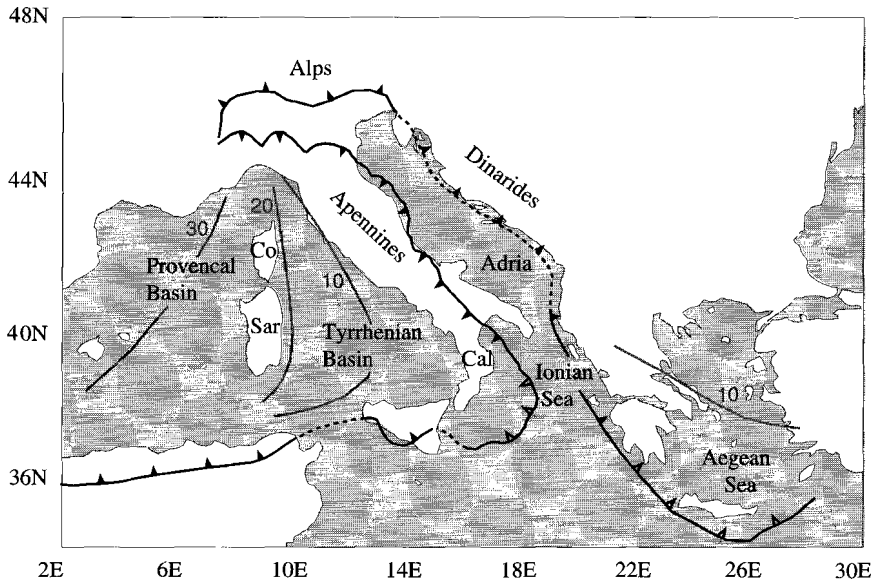

Figure 1.3: Map of the central Mediterranean area. Co = Corsica, Sar = Sardinia, Cal = Calabria. Barbed line indicates convergent zones (filled = inactive, open = active, note, however, that subduction near Calabria might have become inactive). Gray lines are schematic indication of evolution through time of the convergent zones, numbers are Ma.

parameters in the process. The advantages of a computer model over an analogue laboratory model mainly lie in the larger range of material properties which can be used and the possibility to study the reaction of the system to conditions difficult to achieve with a physical model. In general, quantification of model results like strain, topography and stress orientation is more straightforward in a numerical model.

A basic requirement for a model of subduction is a concept of how this process takes place. The physics of subduction has to be described and the relative importance of various effects has to be estimated. Together with the aim of the model, this concept determines which aspects are to be incorporated and how. For example, an approximation of stationary subduction can be obtained by describing its shape with flexure (bending) of a plate under end loads that basically simulate the slab pull force (e.g. *Caldwell et al.*, 1976; *Turcotte et al.*, 1978]. This is analogous to the engineering model of the bending of a beam on an elastic foundation [*Hetényi*, 1946] and, hence, similar modelling methods can be applied. The applicability of such a model is limited to stationary subduction. A model requires a description of the initial situation, material properties and boundary conditions. This part of the modelling procedure incorporates data and concepts from various disciplines from the Earth sciences, for example, seismology, seismic reflection studies, rheological experiments, paleomagnetic analyses and tectonics.

In this thesis two different modelling approaches are used. In the first, the deflection of

a subducted plate is calculated and compared with stratigraphic data. It is assumed that the model that best fits the data gives the best result for the variables that are to be quantified, in this case the loads acting on the plate. In the second approach the temporal evolution of subduction and eventually slab detachment is simulated in order to predict what the effects will be at the Earth's surface. The aim is to obtain insight in the evolution of these processes. In this case no fit to geological data is sought. Surface data can be used a posteriori to determine whether the concept that underlies the numerical model applies to a particular region or not.

1.6 Outline of thesis

Displacements of the Earth's surface which occur during ongoing subduction and in the final stages of a subduction process are the focus of this thesis. The relation between subduction and surface displacements is studied using numerical models. Since the bending of a lithospheric plate during subduction is essentially a flexural process, the numerical models that are used have to be able to simulate lithospheric flexure. Methods for solving flexure of the lithosphere are examined in **Chapter 2**. These form the basis of the models used in the later chapters.

In the final stages of subduction, subducted lithosphere may detach from the lithosphere at the surface. Detachment may occur by lateral propagation of a tear in the subducted slab along strike of the convergent plate margin. In that case, variations in vertical loads are to be expected. In **Chapter 3** it is investigated whether such variations can be inferred from the deflection date recorded in the Plio-Pleistocene foredeep on the eastern side of Italy.

Whether or not slab detachment migrates laterally, it is expected that detachment leads to vertical displacements of the Earth's surface. These are referenced to displacements which can occur during the phase of ongoing subduction. In **Chapter 4** the effects of variations in a subduction zone system on vertical surface displacements are investigated. Surface uplift resulting from slab detachment is quantified in **Chapter 5**. In **Chapter 6** an application of modelling of slab detachment to Northern Italy is described.

Chapter 2

Flexure of the lithosphere: modelling methods

2.1 Flexure of the lithosphere

In principle, the Earth's lithosphere will respond to a loading event by either local or regional isostatic compensation. In local isostasy, compensation takes place directly under the load, while regions away from the load are not affected. However, since the lithosphere possesses lateral strength, it is more likely that a load will be compensated over a wider region than the actual extent of the load itself. The lithosphere will, therefore, react to loading by regional isostasy, or flexure. Different flexural processes affect the lithosphere. For example, mountains, and also sediments deposited in a basin, constitute a vertical load depressing the surface of the lithosphere. At a subduction zone, the subducting plate bends flexurally while underthrusting the overriding plate. A model describing the flexure of a lithospheric plate can be obtained by requiring the plate to be in mechanical equilibrium under all forces exerted on it. In a general way this can be written as:

$$\nabla \cdot \sigma + X = 0 \tag{2.1}$$

where σ is the stress tensor and X denotes the body forces. From this requirement of equilibrium a differential equation describing the flexural behaviour of the plate can be derived. To achieve this, the following approximations are commonly made (see Fig. 2.1 for orientation of coordinate axes): 1) the plate is thin compared with its width (the thin plate approximation), 2) the deflections are small compared with the width of the plate, 3) the bending is plane strain ($\epsilon_{yy} = \epsilon_{xy} = \epsilon_{zy} = 0$), 4) the principal stress normal to the surface of the plate is zero ($\sigma_{zz} = 0$), 5) plane sections of the plate remain plane. With these approximations, the one-dimensional differential equation for the bending of plates is given by:

$$\frac{d^2}{dx^2} D(x) \frac{d^2 w(x)}{dx^2} - S \frac{d^2 w(x)}{dx^2} + k w(x) = p(x) \quad + \text{ boundary conditions} \tag{2.2}$$

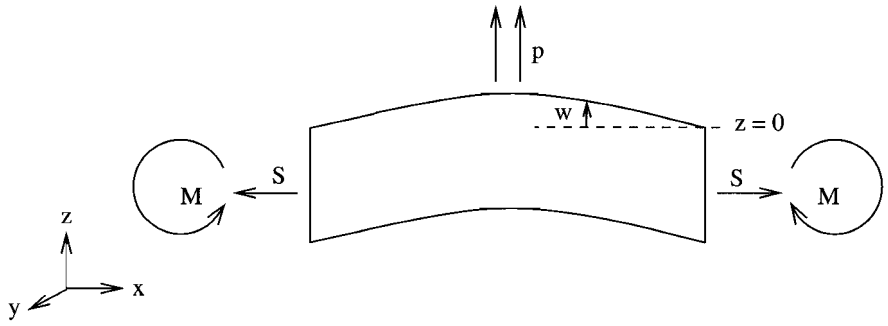

Figure 2.1: Sign convention for forces, moments and displacements (all arrows in positive direction).

where w is deflection, S a (constant) horizontal force, p the vertical load, D flexural rigidity and k the hydrostatic restoring force. The sign convention for these variables is illustrated in Fig. 2.1. The loads acting on the plate are supported by the strength of the plate and the hydrostatic restoring force. This force arises due to the effective replacement of mantle material underlying the plate by material of a lower density overlying the plate. The hydrostatic restoring force per unit area is equal to:

$$kw = (\rho_m - \rho_o)gw \tag{2.3}$$

with ρ_m and ρ_o the densities of the mantle and of material overlying the lithosphere, respectively, and g the gravitational acceleration. Flexural rigidity is a measure of the stiffness of the lithosphere and, therefore, of the plate's resistance to flexure under loading. For a completely elastic plate the flexural rigidity D is defined as:

$$D = \frac{Eh^3}{12(1-\nu^2)} \tag{2.4}$$

where E is Young's modulus, ν Poisson's ratio and h the elastic plate thickness. These last three variables completely determine the flexural response of an elastic plate. For an elastic plate, the bending moment M:

$$M(x) = \int_{-\frac{h}{2}}^{\frac{h}{2}} \sigma z dz \tag{2.5}$$

with bending stress $\sigma = \sigma_{horz} - \sigma_{vert}$, is given by:

$$M(x) = -D\frac{d^2w}{dx^2} \tag{2.6}$$

The shear force V relates to the deflection following:

$$V(x) = \frac{dM}{dx} + S\frac{dw}{dx} \tag{2.7}$$

The flexural rigidity which is used in the differential flexure equation (2.2) is only defined for an elastic plate. In defining the rigidity of a not completely elastic plate use is made of the effective elastic thickness of the lithosphere. This is purely a modelling parameter representing the thickness of an equivalent elastic plate which adequately simulates the observed bending behaviour. The effective elastic thickness is usually smaller than the lithospheric thickness. The effective flexural rigidity that is obtained from the effective elastic thickness can be used to solve the differential flexure equation for plates with a non-elastic rheology. More sophisticated models for the rheology of the lithosphere include elastic-plastic or viscoelastic rheologies. A plate with an elastic-plastic rheology behaves elastically until the bending stresses exceed the yield stress; the material then deforms plastically. Yielding reduces the flexural rigidity. In a viscoelastic model, stresses, which were built up in the lithosphere, relax with time, leading to a decrease in flexural rigidity.

The equation for bending of plates (equation 2.2) can be solved analytically or numerically, depending on the problem at hand. For an elastic plate with laterally constant flexural rigidity and simple boundary conditions, an analytic solution can be obtained. The advantages of analytic methods are that they are accurate and do not involve much computational time. Analytic elastic solutions can give a good first order match to observed lithospheric deflection profiles [e.g. *Watts and Cochran*, 1975; *Caldwell et al.*, 1976]. However, only a very limited amount of flexure problems can be solved with analytic methods. The lithosphere is too complex to be approximated by a laterally homogeneous elastic model. For a model with, for example, a more complex rheology, lateral variability in loading, or different boundary conditions, an analytic solution can no longer be obtained and numerical methods have to be used. In this thesis, subduction processes are examined by the use of numerical modelling. The numerical methods that are used, therefore, have to be capable of simulating lithospheric flexure. This chapter gives an outline of two different methods that are used in this thesis: the finite difference and the finite element method. It is shown that both methods yield reliable solutions to flexure problems. The dependence of the accuracy of the methods on model aspects and (numerical) approximations is examined. Special attention is paid to the effect of intraplate stress on the effective elastic flexural rigidity.

2.2 Solving flexure with the finite difference method

2.2.1 Finite difference approximation

The first step in solving the flexure equation (2.2) with a finite difference method is to discretise the horizontal x-dimension of the model. Here an equidistant grid is used. For each point in this grid a finite difference approximation of the one-dimensional flexure equation is made, resulting in a linear equation for the deflection. The simultaneous solution of this system of equations yields the solution to the bending problem. Derivatives in the differential equation are replaced by central finite difference approximations:

$$\frac{\partial w_n}{\partial x} \approx \frac{w_{n+1} - w_{n-1}}{2d}$$

$$\frac{\partial^2 w_n}{\partial x^2} \approx \frac{w_{n+1} - 2w_n + w_{n-1}}{d^2} \tag{2.8}$$

The subscript on w denotes the grid point involved and d is the stepsize (the distance between grid points). Central finite difference approximations are order (d^2) accurate, while forward and backward difference approximations are only order (d) accurate. Substituting these approximations into the equation for one-dimensional bending of a plate (equation 2.2) leads to the following difference equations:

$$\begin{aligned} &D_{n-1}w_{n-2} + (-2D_{n-1} - 2D_n - Sd^2)w_{n-1} + \\ &(D_{n+1} + 4D_n + D_{n-1} + 2Sd^2 + kd^4)w_n + \\ &(-2D_n - 2D_{n+1} - Sd^2)w_{n+1} + D_{n+1}w_{n+2} = d^4 p_n \end{aligned} \tag{2.9}$$

which may be written in matrix notation as:

$$A_{ij}w_j = q_i \tag{2.10}$$

The matrix A is a five-diagonal banded matrix. A solution can only be obtained for appropriate boundary conditions. Four boundary conditions need to be defined:

- Continuous plate:
  1) for $x \to \infty$, $w \to 0$, so $w_n = 0$ (for total n grid points)
  2) for $x \to \infty$, $dw/dx \to 0$, so $w_{n+1} = w_{n-1}$
  3) for $x = 0$, $w \to 0$, so $w_1 = 0$
  4) for $x = 0$, $dw/dx \to 0$, so $w_0 = w_2$.

- Broken plate:
  1,2) for $x \to \infty$ the same boundary conditions apply as for the continuous plate
  3) at $x = 0$ the bending moment M_0 applied to the end of the plate is fixed:

$$M_0 = -D_{(x=0)} \left(\frac{d^2 w}{dx^2} \right)_{(x=0)} \tag{2.11}$$

  which leads to:

$$w_0 = -M_0 \left(\frac{d^2}{D_1} \right) - w_2 + 2w_1$$

  4) the other boundary condition at $x = 0$ can either be a fixed deflection:

$$w_1 = C \tag{2.12}$$

  or a fixed vertical shear force applied to the end of the plate:

$$-\frac{d}{dx}\left(D\frac{d^2 w}{dx^2} \right)_{(x=0)} + \left(S\frac{dw}{dx} \right)_{(x=0)} = V_0 \tag{2.13}$$

which gives:

$$w_{-1} = \frac{1}{D_0}\left(2V_0d^3 + (2D_0 + Sd^2)w_0 - (D_0 - D_2)w_1 \right.$$
$$\left. -(2D_2 + Sd^2)w_2 + D_2w_3\right)$$

Incorporation of the boundary conditions changes the system of equations (2.10). Naturally, no equation is set up for grid points where the value of the deflection is defined by a boundary condition. The pre-defined values for the deflection are incorporated in the system of equations on the right hand side, in q. The equations are solved by backward substitution [*Conte and de Boor,* 1965].

2.2.2 Comparison with analytical results

Three cases

A test of the solution method is the comparison of numerical deflection profiles with analytical solutions. The finite difference results are compared with the analytical solutions of the following three problems:

1. A continuous elastic plate bending under a lineload.
   The lineload F is applied at $x = 0$, therefore the solution is symmetric around $x = 0$. With the boundary conditions $w \to 0$ as $x \to \pm\infty$, $dw/dx = 0$ at $x = 0$, and the shear force$= -1/2\ F$ at $x = 0$, the solution to the flexure equation is:

   $$w = \frac{F\alpha^3}{8D}e^{-\frac{x}{\alpha}}\left(cos\frac{x}{\alpha} + sin\frac{x}{\alpha}\right) = \frac{F}{2\alpha k}e^{-\frac{x}{\alpha}}\left(cos\frac{x}{\alpha} + sin\frac{x}{\alpha}\right) \tag{2.14}$$

   The flexural parameter α:

   $$\alpha = \sqrt[4]{\frac{4D}{k}} \tag{2.15}$$

   measures the wavelength of the flexure.

2. A broken elastic plate bending under a fixed moment and shear force (trench profile of *Turcotte and Schubert* [1982]).
   The moment M_0 and shear force V_0 act at the origin, which is located at the trench. With the boundary conditions $w \to 0$ as $x \to \infty$, $M = M_0$ at $x = 0$ and $V = V_0$ at $x = 0$, the equation describing the deflection is:

   $$w = \frac{\alpha^2}{2D}e^{-\frac{x}{\alpha}}\left(-M_0sin\frac{x}{\alpha} + (V_0\alpha + M_0)cos\frac{x}{\alpha}\right) \tag{2.16}$$

3. A broken elastic plate loaded by a horizontal force S (universal elastic trench profile of *Caldwell et al.* [1976]).
   The origin is located at the point nearest the trench where the deflection equals zero. The boundary conditions are: $w \rightarrow 0$ as $x \rightarrow \infty$ and $w = 0$ at $x = 0$. The trench profile is given by:

$$w = Asin\left(\frac{x}{\alpha}\sqrt{1+\epsilon}\right) e^{-\frac{x}{\alpha}\sqrt{1-\epsilon}} \tag{2.17}$$

   where A is a constant and ϵ a dimensionless parameter defined by $\epsilon = S/2\sqrt{kD}$. A solution does not exist for ϵ greater than one. The location and height of the point of maximum positive deflection, i.e. the bulge, are given by x_b and w_b, respectively:

$$x_b = \frac{\alpha}{\sqrt{1+\epsilon}} arctan\left(\sqrt{\frac{1+\epsilon}{1-\epsilon}}\right)$$

$$w_b = \frac{A\sqrt{1+\epsilon}}{\sqrt{2}} e^{-\frac{x_b}{\alpha}\sqrt{1-\epsilon}} \tag{2.18}$$

   The constant A can be derived from these two expressions.

For the three cases distinguished above, Fig. 2.2 shows both the analytical and numerical deflection profiles, as well as the difference between the two. In all cases the elastic thickness is 10 km. The results of the two different solution methods agree very well. In general, the difference between the finite difference and the analytical solution is related to curvature, the difference being greater with larger magnitude of curvature.

Accuracy

The use of a numerical method poses constraints on the accuracy that can be reached. A main restriction on the accuracy of the finite difference solution is formed by the discretisation of the solution domain. The discretisation is important in that only solutions at specific points are obtained, but it also enters the solution through the central difference approximations (equation 2.8) to the derivatives in the differential flexure equation (2.2). Whereas plate bending is essentially a non-linear process, linear approximations were used. A smaller stepsize is expected to reduce the error associated with these approximations and, therefore, to lead to a more accurate solution. This is confirmed by the results shown in Fig. 2.3, where the finite difference solution is compared with the analytical solution to the problem of a broken plate bending under a bending moment and shear force (case 2). The error is parameterised by the L_2-norm of the difference between the two solutions:

$$(\sum_n (w_{num} - w_{an})^2)^{\frac{1}{2}} \tag{2.19}$$

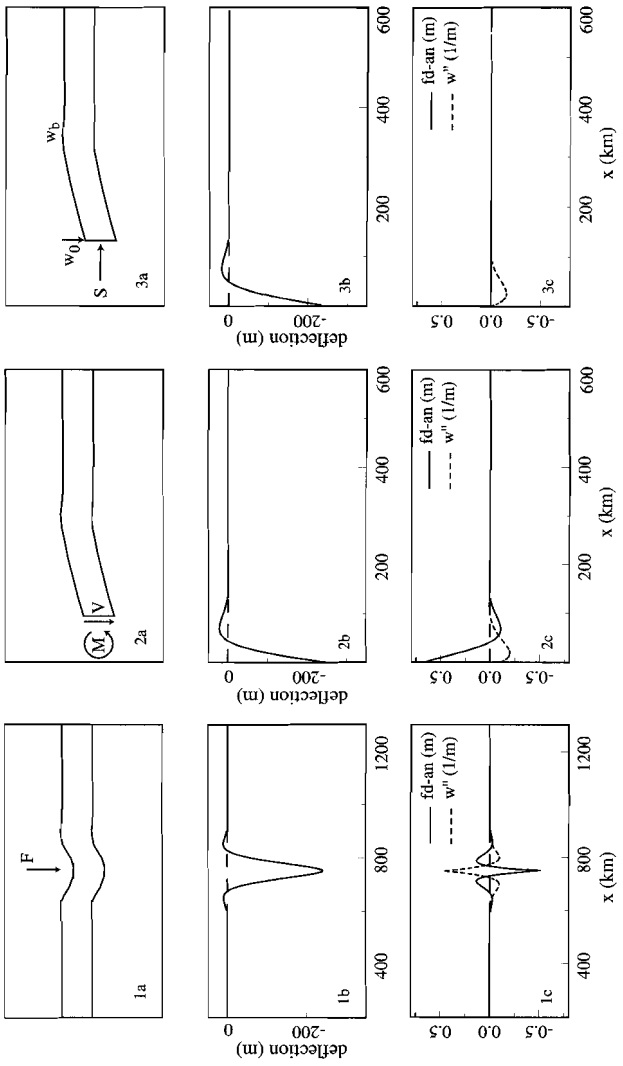

Figure 2.2: Comparison between finite difference and analytical solutions. For all figures the elastic plate thickness is 10 km, $E = 1 \times 10^{11}$ Pa, $\nu = 0.25$ and density of the mantle ρ_m = 3250 kg m^{-3}. a figures: cartoon showing loading situation. b figures: deflection profiles obtained with finite difference (drawn line) and analytical (dotted line) method. Dashed line indicates zero deflection. c figures: difference between finite difference and analytical (drawn line) solution compared with curvature $\times 10^{12}$ (dotted line). 1) continuous plate for a lineload of 5×10^{11} N m^{-1}, 2) broken plate with $M_0 = 1 \times 10^{15}$ N and $V_0 = -1 \times 10^{11}$ N m^{-1}, 3) broken plate with w_b = 18.5 m and a horizontal compression of 100 MPa. This profile is shifted to have the origin at the trench, in agreement with case 2. For the finite difference solution w_0 = -250 m and M_0 = 0.

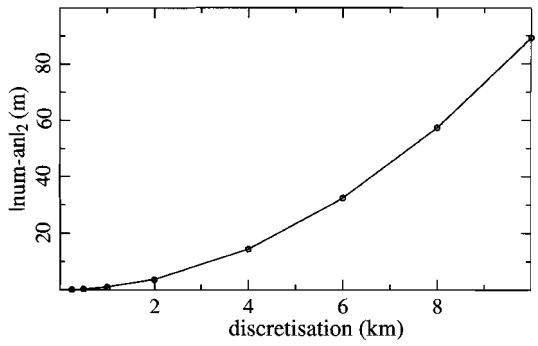

Figure 2.3: Difference in L_2-norm between finite difference and analytical solution versus step size for a case 2 bending problem. Plate thickness = 20 km, M = 2×10^{16} N, V = -1 $\times10^{12}$ N m^{-1}.

The error increases with stepsize d as order (d^2), which is the error made in approximating derivatives with central finite differences. Stepsizes greater than 3000 m are not used in this chapter and the following.

The analytical solutions are derived under the assumption of a plate extending infinitely in the horizontal x-direction, while numerical models are, of course, always finite. The length of the numerical model can potentially influence the accuracy of the solution. If, for a particular problem, plate length is not chosen large enough, the direct influence of the boundary conditions can deteriorate the numerical solution. Fig. 2.4 shows the effect of decreasing the plate length on the fit of the finite difference to the analytical solution. For plate lengths smaller than 400 km the error rapidly increases. The apparently improving fit for plate lengths around 260 km is caused by the boundary condition of zero deflection at the plate end coinciding with an actual point of zero deflection in the analytical solution.

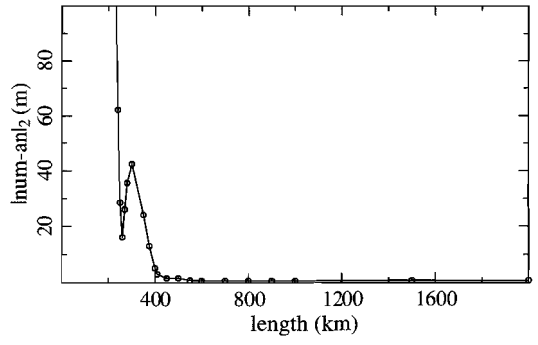

Figure 2.4: Difference in L_2-norm between finite difference and analytical solution versus plate length of the finite difference model for a case 2 bending problem. Plate thickness = 20 km, M = 2×10^{16} N, V = -1 $\times10^{12}$ N m^{-1}.

The finite difference method solves the flexure equation (2.2), which is derived under different assumptions. The effects on the accuracy of not completely satisfying these constraints cannot be evaluated by a comparison with the analytical solution, since this is a solution to the same equation. Two constraints, those of small deflections and a small plate thickness, can potentially be important. The other constraints are automatically fulfilled by applying the flexure equation. To evaluate the influence of not (rigidly) adhering to the constraints of small deflections or a thin plate, an independent method, which does not solve the flexure equation 2.2, has to be used. *Comer* [1983] gives an analytical solution for thick plate flexure. For thick plates the vertical principal stress no longer vanishes ($\sigma_{zz} \neq 0$) and the deflection is a function of depth as well: w(x,z). The example of Fig. 2.5 shows that the thin plate solution tends to underestimate the maximum deflection. Overall, however, it can be stated that the thin plate theory gives a good approximation to the more exact thick plate solution. The solution of *Comer* [1983] neglects the effects of gravitation within the plate. *Wolf* [1985; see also *Comer,* 1986] shows that including gravitational body forces in flexure of an incompressible plate reduces the difference with the thin plate solution. The effects of large deflections and plate thickness on accuracy are further discussed in the second part of this chapter (section 2.3.2), where solutions to bending problems obtained with a finite element method are compared with analytical solutions.

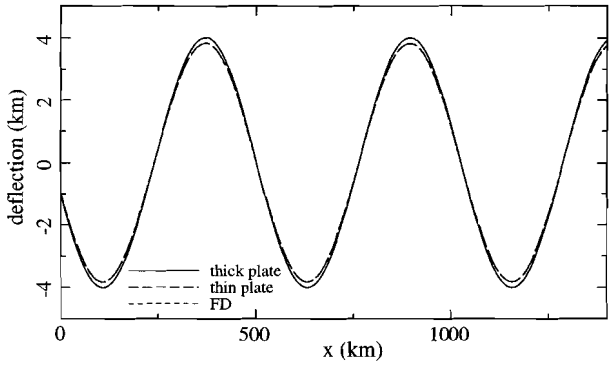

Figure 2.5: Thick plate flexure. The plate is loaded by a periodic load $q\ cos(k_w x)$, amplitude q = 2.1 $\times 10^8$ N, wavenumber $k_w = 1.2 \times 10^{-5}$ m^{-1}. Plate thickness 50 km, E = 1 $\times 10^{11}$ Pa, ν = 0.25, ρ_m = 3250 kg m^{-3}. Drawn line: analytical thick plate solution (solution of *Comer* [1983]), dashed line: analytical thin plate solution, dotted line: finite difference thin plate solution (coincides with analytical thin plate solution). Solutions are for the midplane of the plate.

2.2.3 Brittle-plastic rheology

In the previous section solutions to flexure problems for a completely elastic plate have been examined and compared with analytical solutions. In this section a non-elastic rheology is introduced. The rheology considered here is an elastic-plastic rheology, meaning that the

plate behaves elastically until the bending stresses exceed the yield stress. In those regions of the plate where the yield stress has been reached the material deforms as a perfectly plastic material, not supporting stresses greater than the yield stress. Time dependent effects are explicitly not included. For the variation of yield stress with depth, two cases are distinguished: a single yield envelope and a double yield envelope (Fig 2.6). A single yield envelope describes yielding by brittle and plastic failure in the upper and lower parts of the plate, respectively. In general, the central region of the plate remains elastic; this region is termed the elastic core [*Bodine,* 1981]. The upper envelope of a double yield envelope characterises yielding in the crust, the lower in the mantle. The convention is adopted that compression is negative and $\sigma_1 < \sigma_3$.

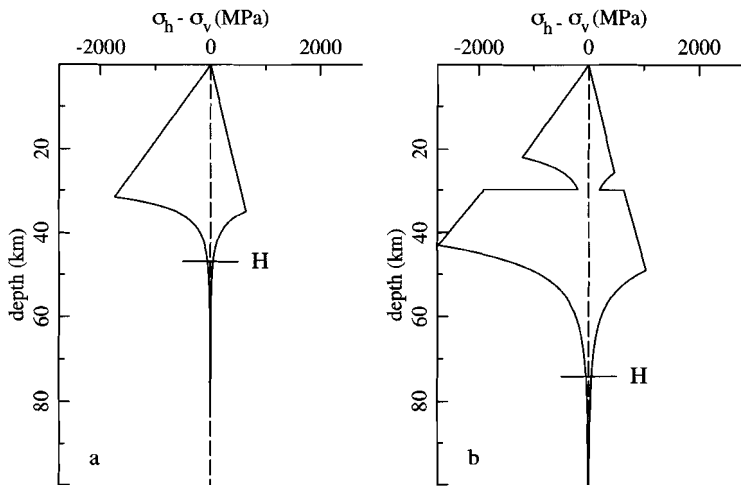

Figure 2.6: Yield rheologies for $\dot{\epsilon} = 10^{-14}$ s^{-1}. Compression is negative. a: single 'oceanic' envelope (*Crough* [1975] geotherm, lithosphere thickness 80 km), b: double 'continental' envelope (*Chapman* [1986] geotherm, surface heat flow 55 mW m^{-2}, Moho depth 30 km). In both figures H indicates the mechanical thickness (where the ductile strength is 50 MPa [*Bodine*, 1981]).

The yield stress in the brittle regime follows the linear frictional failure criterion [*Byerlee,* 1978], referred to as Byerlee's law:

$$\tau = \mu' \sigma_n + S_0 \approx \mu \sigma_n \tag{2.20}$$

where τ and σ_n are the shear and normal stresses acting on the surface under consideration, S_0 is the cohesion, and μ is the coefficient of friction. Byerlee's law can be rewritten in terms of the principal stresses σ_1 and σ_3 [*Jaeger and Cook,* 1979]. For vertical σ_3 material is in the thrust fault regime, for vertical σ_1 it is in the normal fault regime [c.f. *Anderson,* 1951; *Sibson,* 1974]. In terms of principal stresses Byerlee's law becomes:

$$compressive: \quad (\sigma_1 - \sigma_3) = \frac{2\mu}{\sqrt{1+\mu^2} - \mu} \sigma_v$$

$$tensile: \qquad (\sigma_1 - \sigma_3) = \frac{2\mu}{\sqrt{1+\mu^2}+\mu}\sigma_v \tag{2.21}$$

The effective pressure σ_v is given by:

$$\sigma_v = \rho_r g z(1 - \lambda) \tag{2.22}$$

where ρ_r is rock density and λ the pore-fluid factor:

$$\lambda = \frac{P}{\rho_r g z} \tag{2.23}$$

with P pore-fluid pressure. The presence of pore fluids can lead to a reduction of the strength of the lithosphere. If the pore pressure is hydrostatic, then $P = \rho_{fluid}$gz and $\lambda = \rho_{fluid}/\rho_r \approx 0.38$. In the finite difference code used in this chapter values of stresses and strains relative to the cartesian coordinate system are used. For deflections typically encountered in lithospheric bending problems, where $\frac{\partial w}{\partial x} < 10^{-2}$, the stresses $\sigma_{xx}, \sigma_{yy}, \sigma_{zz}$ can be considered to be equal to the principal stresses $\sigma_1, \sigma_2, \sigma_3$. Taking into account also the fact that the differential flexure equation (2.2) is only valid for $\sigma_{zz} = 0$, Byerlee's law can be written relative to the cartesian coordinate system:

$$\begin{aligned} compressive: \quad \sigma_{xx} &= \frac{2\mu}{\sqrt{1+\mu^2}-\mu}\sigma_v \\ tensile: \quad \sigma_{xx} &= \frac{-2\mu}{\sqrt{1+\mu^2}+\mu}\sigma_v \end{aligned} \tag{2.24}$$

In the lower part of the lithosphere or in the lower crust, the plastic yield stress is described by the flow law for power law creep:

$$\dot{\epsilon_1} = A(\sigma_1 - \sigma_3)^n e^{\frac{-Q_{pl}}{RT}} \tag{2.25}$$

where $\dot{\epsilon_1}$ is strain rate, T temperature, R the universal gas constant, Q_{pl} activation energy, and n and A are constants. This form of the flow law is valid for uni- or tri-axial stress states only and, therefore, needs to be extended to a general state of stress. Since the general flow law should also be valid under any coordinate transformation, it is expressed in terms of invariants of the stress and strain rate tensors. For a homogeneous, isotropic, incompressible medium the generalised flow law is [*Ranalli,* 1987]:

$$\dot{\epsilon_{ij}} = \frac{3^{\frac{(n+1)}{2}}}{2} A {\sigma'_E}^{(n-1)} \sigma'_{ij} e^{\frac{-Q_{pl}}{RT}} = A_{pl} {\sigma'_E}^{(n-1)} \sigma'_{ij} e^{\frac{-Q_{pl}}{RT}} \tag{2.26}$$

where $\dot{\epsilon_{ij}}$ is the strain rate tensor, σ'_{ij} the deviatoric stress tensor and σ'_E the effective shear stress:

$$\sigma'_E \equiv \left(\frac{1}{2}\sigma'_{ij}\sigma'_{ij}\right)^{\frac{1}{2}} \tag{2.27}$$

With $\sigma_{zz} = 0$ and $\dot{\epsilon_{xx}} = -\dot{\epsilon_{zz}}$ ($\epsilon_{yy} = 0$ (plane strain) and incompressibility), the general flow law can be expressed relative to the cartesian coordinate system:

$$\dot{\epsilon_{xx}} = \frac{1}{2} A_{pl} {\sigma'_E}^{(n-1)} e^{\frac{-Q_{pl}}{RT}} \sigma_{xx} \tag{2.28}$$

An expression for the effective shear stress σ'_E in cartesian coordinates needs thus to be found for the adopted geometry. With the following relations:

$$\begin{aligned} \sigma_{yy} &= \nu\sigma_{xx} && \text{(from Hooke's law and } \epsilon_{yy} = 0) \\ \sigma_{yz} &= \sigma_{xy} = 0 \\ \sigma_{xz} &= \tfrac{E}{2(1+\nu)} \tfrac{\partial w}{\partial x} && \text{(from Hooke's law and } \epsilon_{ij} = \tfrac{1}{2}(\tfrac{\partial w_i}{\partial x_j} + \tfrac{\partial w_j}{\partial x_i})) \end{aligned}$$

the effective shear stress can be expressed as:

$$\begin{aligned} \sigma'_E &= \left(\frac{1}{3} {\sigma_{xx}}^2 (\nu^2 - \nu + 1) + \left(\frac{E}{2(1+\nu)} \frac{\partial w}{\partial x} \right)^2 \right)^{\frac{1}{2}} \\ &\approx \left(\frac{1}{3} (\nu^2 - \nu + 1) \right)^{\frac{1}{2}} \sigma_{xx} \end{aligned} \tag{2.29}$$

The approximation is valid for $\frac{\partial w}{\partial x} < 10^{-4}$. Inserting this expression in equation 2.28, the flow law becomes:

$$\dot{\epsilon_{xx}} = \frac{1}{2} \left(\frac{1}{3} (\nu^2 - \nu + 1) \right)^{\frac{n-1}{2}} A_{pl} e^{\frac{-Q_{pl}}{RT}} {\sigma_{xx}}^n = A'_{pl} e^{\frac{-Q_{pl}}{RT}} {\sigma_{xx}}^n \tag{2.30}$$

The flow laws which are used in this chapter are for dry anorthosite [*Shelton and Tullis,* 1981] for the lower crust and for wet Aheim dunite [*Chopra and Patterson,* 1981] for the mantle. These flow laws are intermediate between the various flow laws reported in literature. Table 2.1 lists values for the parameters in the brittle and power law creep yield laws. For the variation of temperature with depth the thermal gradient of *Crough* [1975] is used for oceanic lithosphere and the gradient of *Chapman* [1986] for continental lithosphere. The depth at which the ductile strength has decreased to 50 MPa is termed the mechanical thickness H [*Bodine,* 1981] and determines the bottom of the mechanically strong part of the lithosphere (Fig. 2.6).

2.2.4 Effective elastic flexural rigidity and effects of intraplate stress

Derivation of the effective elastic flexural rigidity

Single yield envelope

The deflection of a plate with a yield envelope rheology can be obtained by solving the flexure equation with an effective elastic flexural rigidity, which is derived by requiring that the bending moment supported by the plate with the yield envelope rheology equals the bending moment of an elastic plate. Since the effective rigidity is now also a function of deflection, $D = D(x,w)$, the flexure equation (2.2) has to be solved iteratively. In this paragraph the

parameter	symbol	value	unit
coefficient of friction	μ	0.577	
pore fluid factor	λ	0	
universal gas constant	R	8.31	J K^{-1} $mole^{-1}$
densities			
crust	ρ_{crust}	2800	kg m^{-3}
mantle	ρ_{mantle}	3250	kg m^{-3}
Power law creep - crust			
pre-exponent	A	2.06×10^{-23}	s^{-1} $Pa^{-3.2}$
	A'_{pl}	1.23×10^{-23}	s^{-1} $Pa^{-3.2}$
activation energy	Q_{pl}	238.6	kJ $mole^{-1}$
power	n	3.2	
Power law creep - mantle			
pre-exponent	A	5.50×10^{-25}	s^{-1} $Pa^{-4.48}$
	A'_{pl}	2.87×10^{-25}	s^{-1} $Pa^{-4.48}$
activation energy	Q_{pl}	498	kJ $mole^{-1}$
power	n	4.48	

Table 2.1: Yield envelope parameters

effective elastic flexural rigidity for a plate with a single yield envelope rheology is derived. The total bending moment supported by the plate with the yield envelope rheology is calculated by integrating the vertical stress profile of the plate over the mechanical thickness H:

$$M_{tot} = \int_{-H/2}^{H/2} \sigma(z) z dz \tag{2.31}$$

where $\sigma = \sigma_{horz} - \sigma_{vert}$. In order to facilitate the numerical integration, the ductile parts of the yield envelope are fitted to a linear regression line (Fig. 2.7). According to *Bodine* [1981] the effect of neglecting the lower part of the yield envelope is small for all loads. The total bending moment of the plate is the sum of the bending moments of the elastic core M_{ec} and the yielded parts M_{br} and M_d: $M_{tot} = M_{ec} + M_{br} + M_d$, where br and d indicate brittle and ductile, respectively (Fig. 2.7). The bending moment of the elastic core is related to the rigidity of the elastic core D_{ec} by the curvature:

$$M_{ec} = -D_{ec} \frac{d^2 w}{dx^2} = -D_{ec} w''. \tag{2.32}$$

The rigidity of the elastic core can be calculated by (see equation 2.4):

$$D_{ec} = \frac{E(e_1 - e_2)^3}{12(1 - \nu^2)} \tag{2.33}$$

e_1 and e_2 denote the top and bottom of the elastic core, respectively (Fig. 2.7). The value of

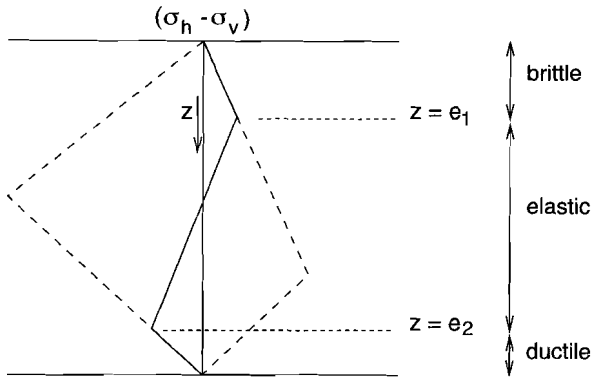

Figure 2.7: Elastic and yielded portions of a plate with a single yield envelope (plastic yield stress is approximated by a linear line)

e_2 is found by Newton-Raphson search on the function $f(e_2)$:

$$f(e_2) = \int_{e_2}^{e_1} \sigma(z) z dz - w'' \frac{E(e_1 - e_2)^3}{12(1-\nu^2)} = 0 \tag{2.34}$$

and e_1 is determined from e_2 by requiring that the horizontal force S equals:

$$S = \int_{-H/2}^{H/2} \sigma(z) dz \tag{2.35}$$

For a purely elastic plate the bending moment M_e is related to curvature by $M_e = -D_e w''$. Equating the total bending moment of the plate with the yield envelope rheology with the bending moment of an elastic plate yields the effective elastic flexural rigidity:

$$D_{eff} = \frac{M_{tot}}{-w''} = \frac{M_{tot}}{M_{ec}} D_{ec} \tag{2.36}$$

Double yield envelope
The effective elastic flexural rigidity for a plate with a double yield envelope rheology is the sum of the effective rigidities of the two separate yield envelopes, which are derived in the same way as above:

$$D_{eff} = D_{eff}(crust) + D_{eff}(mantle) \tag{2.37}$$

Effect of intraplate stress on effective flexural rigidity

Since intraplate stresses can lead to a change in the total bending moment of a plate, these stresses may affect the effective elastic flexural rigidity of the plate (see equation 2.36). In this paragraph the variation of effective elastic flexural rigidity with intraplate stress is

evaluated for the following rheologies: elastic, elastic-perfectly plastic, a symmetric and a non-symmetric single yield envelope.

Elastic
The rigidity of a purely elastic plate does not change with intraplate stress σ_h, since the bending moment remains the same:

$$M_{tot} = \int_{-H/2}^{H/2} (\sigma z + \sigma_h z) dz = \int_{-H/2}^{H/2} \sigma z dz \tag{2.38}$$

The stress profile translates in the direction imposed by the sign of the intraplate stress (Fig. 2.8a).

Elastic-perfectly plastic
An elastic-perfectly plastic rheology is defined by a yield stress $\pm\sigma_y$ which is constant with depth. For small curvatures the plate remains completely elastic, while for curvatures exceeding the threshold value yielding will take place in the upper and/or lower parts of the plate. For a plate with yielding at the top and bottom, an applied horizontal stress σ_h translates the stress profile in the elastic core vertically over $(H\sigma_h)/(2\sigma_y)$, while outside the elastic core the stress remains equal to the yield stress (Fig. 2.8b). In this case the bending moment for $w'' < 0$ is given by [*McAdoo et al,* 1978]:

$$M_{ep} = \frac{\sigma_y H^2}{4} - \frac{(H\sigma_h)^2}{4\sigma_y} - \frac{\sigma_y}{12}\left(\frac{-2\sigma_y(1-\nu^2)}{Ew''}\right)^2 = M_{ep}^{(\sigma=0)} - \frac{(H\sigma_h)^2}{4\sigma_y} \tag{2.39}$$

for $w'' > 0$ the bending moment is -M_{ep}. Tension or compression thus reduces $|M_{ep}|$, leading to a small decrease in the effective elastic flexural rigidity.

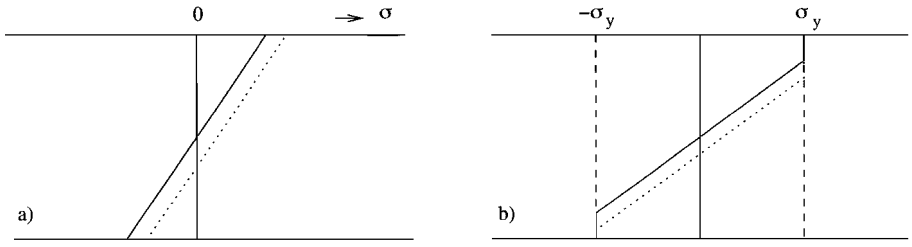

Figure 2.8: Stress profiles for $w'' < 0$ without (drawn line) and with (dotted line) intraplate tension. a) elastic rheology, b) elastic-perfectly plastic rheology.

Symmetric single yield envelope
For a plate with a rheology determined by a yield envelope, which is symmetric relative to the midplane of the plate and relative to $\sigma = 0$, an intraplate stress does not have the effect of translating the stress profile in the elastic core; instead the stress profile changes non-linearly (Fig. 2.9). Figs. 2.10 and 2.11 illustrate the effects on rigidity and bending

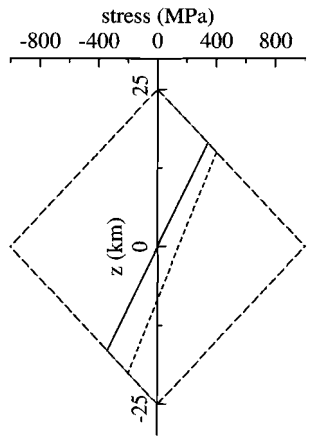

Figure 2.9: Stress profiles for a yield rheology with a symmetric yield envelope. Mechanical thickness is 50 km, $w'' = -1 \times 10^{-7}$ m^{-1}. Drawn line: without intraplate stress, dotted line: 100 MPa tension.

moments of applying 100 MPa tension to a plate with a rheology governed by a symmetric yield envelope. The effective rigidity is the sum of the elastic, brittle and ductile parts:

$$D_{eff} = \frac{M_{tot}}{-w''} = \frac{M_{br}}{-w''} + \frac{M_{ec}}{-w''} + \frac{M_d}{-w''} \tag{2.40}$$

In case no horizontal stresses are applied and $w'' = 0$, the stress is zero throughout the whole plate. Since the whole plate is elastic, the rigidity of the elastic core is equal to the effective rigidity which is determined by the mechanical thickness of the plate. All bending moments are zero at zero w''. With increasing $|w''|$, yielding takes place over an increasing depth interval, leading to a decrease in the rigidity of the elastic core and in the effective rigidity. These effects are illustrated in Fig. 2.10a and b. Due to the symmetric form of the yield envelope, the brittle and ductile bending moments are equal.

Horizontal tension or compression induces, for $w'' = 0$, a stress profile that is not constant with depth. The top and bottom of the central elastic part determine the rigidity of the 'elastic core' (equations 2.32 and 2.33). The different parts of the total bending moment sum to zero (Fig. 2.11b). Since the yield envelope is symmetric, the stress is constant in the elastic depth interval and the elastic bending moment is zero. The brittle and ductile bending moments are equal in magnitude and opposite in sign. For the case of an applied tension, the brittle bending moment decreases with increasing positive curvature. For $M_{br} = 0$ the top of the elastic core lies at the top of the plate (Fig. 2.12). For all values of curvature shown in Fig. 2.11a, the effective rigidity is greater than its maximum value for the situation without horizontal stresses. The effective elastic flexural rigidity is merely a parameter which is used to simulate the deflection of a plate with a yield envelope rheology, its value is thus not limited by the maximum value for the rigidity of the plate with this rheology.

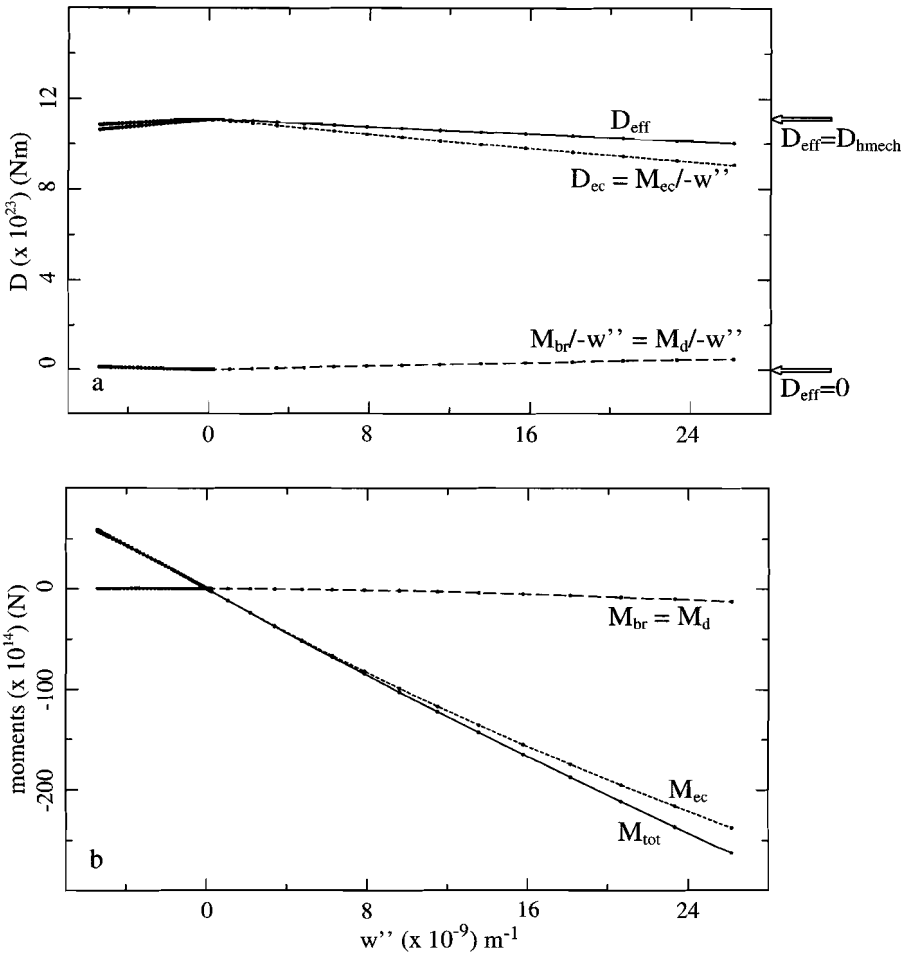

Figure 2.10: a) Flexural rigidity versus curvature of the plate. b) Bending moments versus curvature. Quantities are evaluated for a plate with a symmetric single yield envelope rheology, $\sigma_h = 0$ and a mechanical plate thickness of 50 km. Dots indicate for which curvature values moments and rigidities have been computed. br = brittle, d = ductile, ec = elastic core, D_{hmech} = rigidity defined using the mechanical thickness of the plate.

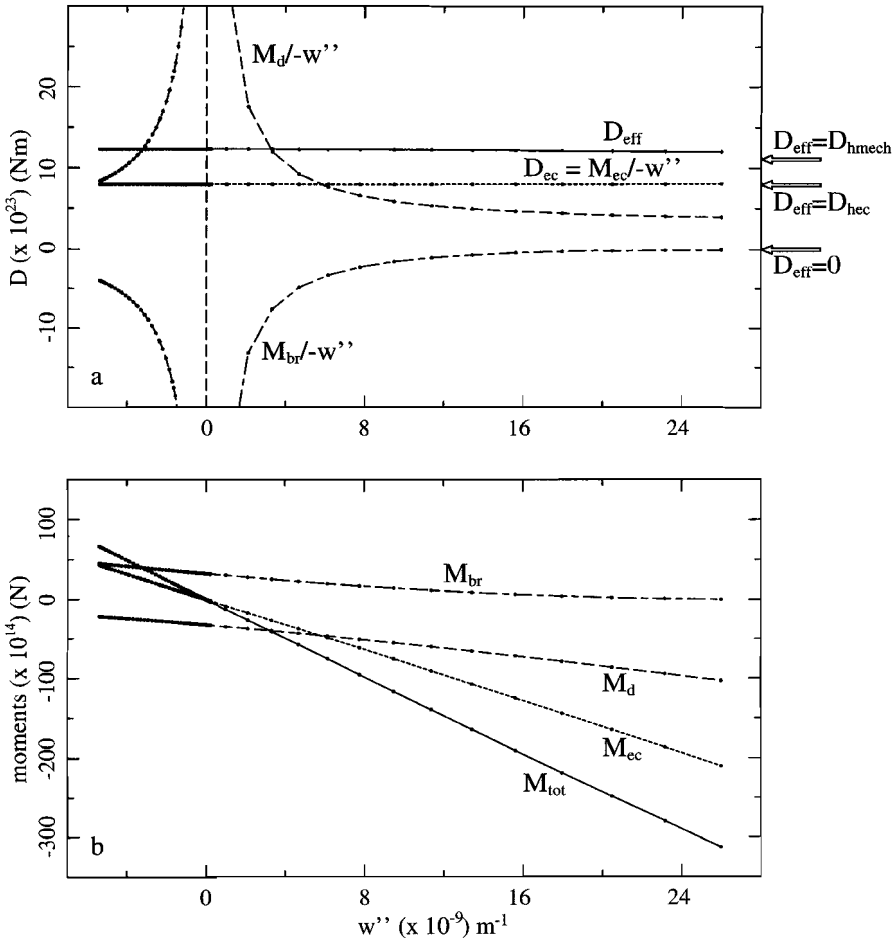

Figure 2.11: a) Flexural rigidity versus curvature. b) Bending moments versus curvature. σ_h = 100 MPa, all other parameters as in Fig. 2.10. D_{hec} = rigidity of the elastic core at $w'' = 0$.

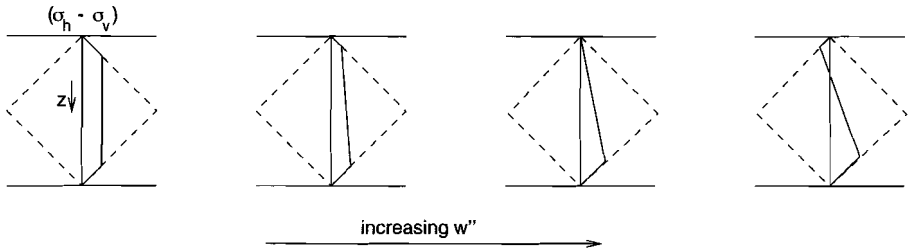

Figure 2.12: Schematic representation of changes in stress profile with increasing positive curvature for $\sigma_h > 0$.

Thus for a fixed value of curvature, the effect of a horizontal force on a plate with a yield envelope rheology is to increase the effective elastic flexural rigidity of the plate. Since the effective rigidity of a purely elastic plate does not change with stress, it can be expected that the increase in effective rigidity for a plate with a yield envelope rheology will reduce if the plate more resembles an elastic plate. That this is indeed the case is shown in Fig. 2.13, where the increase in flexural rigidity with intraplate stress is shown for three different values for the slopes of the yield envelope. A greater value for the slope (a 'wider' yield envelope) indicates a more elastic behaviour of the plate. The rigidities are all derived for $w'' = 10^{-11}$ m^{-1}, for this low value of curvature the rigidity for a plate without intraplate stress is determined by the thickness of the plate (equation 2.4).

Non-symmetric single yield envelope

For a yield envelope which is symmetric around the midplane of the plate the total bending moment is zero for $w'' = 0$ also in case of intraplate stresses (see previous paragraph). For a non-symmetric yield envelope, however, intraplate stresses lead to a non-zero bending moment, M_h, even for $w'' = 0$. If this bending moment is not accounted for, the effective elastic rigidity can possibly become negative, which is physically unrealistic. This can be corrected by subtracting the bending moment due to intraplate stress from the total bending moment in the following way:

$$M_{tot,new} = M_{tot} - M_h = \int_{-H/2}^{H/2} \sigma(z)(z - z_{gr})dz \tag{2.41}$$

z_{gr} is the depth relative to which the bending moment is zero for $w'' = 0$ [*Kooi*, 1991] and is found by Newton-Raphson search on:

$$f(z_{gr}) = M_{tot} - M_h = \int_{-H/2}^{H/2} \sigma(z)zdz - \int_{-H/2}^{H/2} \sigma(z)z_{gr}dz = 0 \tag{2.42}$$

for $w'' = 0$. The effective elastic flexural rigidity for a plate with a yield envelope rheology acted upon by horizontal forces is now given by:

$$D_{eff} = \frac{M_{tot} - M_h}{M_{ec} - M_{ec,h}} D_{ec} \tag{2.43}$$

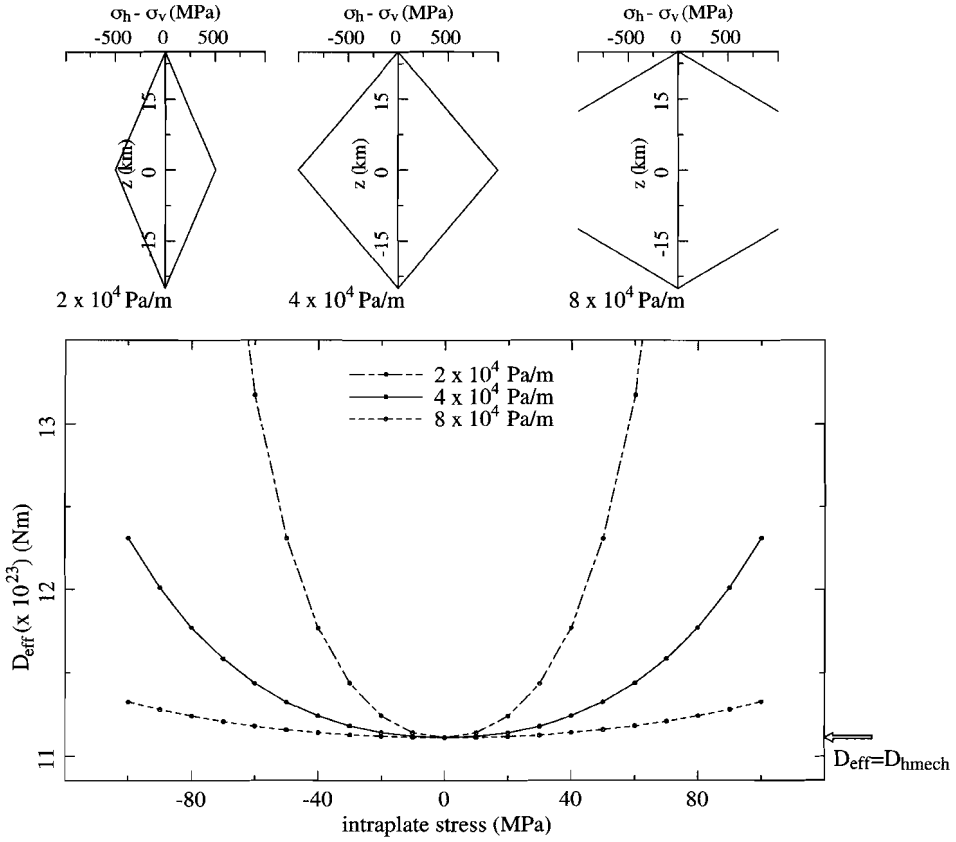

Figure 2.13: Effective rigidity versus intraplate stress for three different symmetric yield envelopes parameterised by the slope values indicated in the figure. The yield envelopes are shown above. $w'' = 10^{-11}$ m^{-1}. In Figs. 2.10 and 2.11 the slope of the yield envelope is 4×10^4 Pa m^{-1}.

Taking into account the intraplate stress-bending moment in this way amounts to writing the flexure equation (2.2) as:

$$-\frac{d^2M}{dx^2} + \frac{d^2M_h}{dx^2} - S\frac{d^2w(x)}{dx^2} + kw(x) = p(x) \tag{2.44}$$

which is equivalent to:

$$-\frac{d^2M}{dx^2} - S\frac{d^2w(x)}{dx^2} + S\frac{d^2z_{gr}}{dx^2} + kw(x) = p(x) \tag{2.45}$$

If the whole plate has the same rheology (i.e. M_h does not vary laterally), these equations show that calculations with the adjusted effective rigidity give exactly the same results as with the original effective rigidity.

Due to the symmetric form of the yield envelope, the rigidities in Fig. 2.13 were equal for a compression or tension of the same magnitude. For a yield envelope which is not symmetric (relative to the middle of the plate and to $\sigma = 0$), the curve of effective rigidity against intraplate stress is not symmetric relative to the line $\sigma_h = 0$ (Fig. 2.14a). In Fig. 2.14b is shown z_{gr}, the depth used in determining the moment generated by the intraplate stresses for $w'' = 0$.

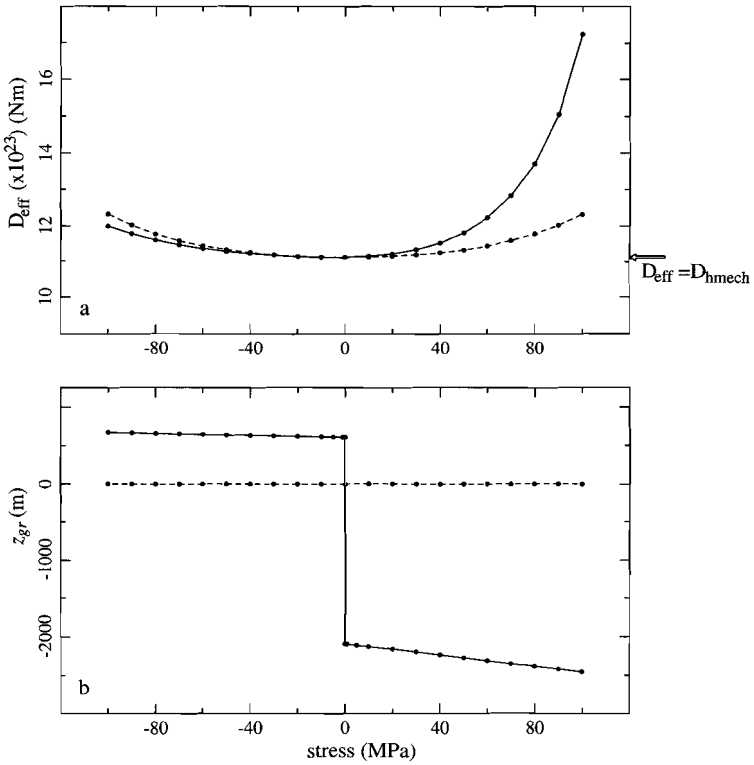

Figure 2.14: A) Effective rigidity against intraplate stress. B) z_{gr} against intraplate stress. Drawn line: non-symmetric yield envelope, dotted line: symmetric yield envelope, $w'' = 10^{-11}$ m^{-1}.

2.3 Solving flexure with the finite element method

2.3.1 The finite element method

In the previous sections a finite difference code is described which explicitly solves the flexure equation. This equation is derived under different approximations and assumptions (section 2.1) which have to be fulfilled for the problem under consideration. The class of

problems which can be solved with this method is thus limited. The finite element method allows for a more flexible code. In this thesis the finite element program TECTON is used which was originally developed by *Melosh and Raefsky* [1980, see also *Melosh and Raefsky*, 1983; *Melosh and Williams,* 1989]. The code does not explicitly solve the flexure equation, but can well be applied for solving bending problems, as is shown by the comparison of numerical with analytical solutions in the next section. Restrictions like the thin plate approximation now no longer apply. In this paragraph the basic steps in the finite element method will be shortly outlined, focussing on tectonic problems. More detailed information can, among others, be found in *Hughes* [1987], *Zienkiewicz* [1977] and *Owen and Hinton* [1980].

The equations governing a tectonic problem are the equations of mechanical equilibrium (equation 2.1):

$$\nabla \cdot \sigma + X = 0$$

where σ is the stress tensor and X denotes the body forces. These are supplemented with constitutive equations, which describe the rheology of the material:

$$\dot{\epsilon} = f(\dot{\sigma}, \sigma) \tag{2.46}$$

where ϵ is strain. A superdot indicates differentiation with respect to time. In this thesis an elastic rheology is used and $\epsilon = f(\sigma)$.

The main step in the finite element method, of which the method derives its name, is the discretisation of the solution domain into elements. Basic elements like three node triangles and four node quadrilaterals are frequently used. Solutions for the displacements are obtained at the nodes of the elements and interpolated, by the use of shape functions, to obtain displacements in the elements. For each element a shape function, therefore, needs to be specified:

$$u \approx u^h = \Sigma_i N_i d_i \tag{2.47}$$

where u is the displacement, u^h its approximation on the finite element mesh, d_i the nodal displacements and N_i the shape functions. From the element displacements, strains and stresses can be derived. The strain:

$$\epsilon_{ij} = \frac{1}{2}(u_{i,j} + u_{j,i}) \tag{2.48}$$

where a comma denotes differentiation, can be directly written as a function of the nodal displacements:

$$\epsilon^h = Lu^h = LNd = Bd \tag{2.49}$$

The matrix B is the strain-displacement matrix. The stresses are obtained from the strains:

$$\sigma = D(\epsilon - \epsilon_0) + \sigma_0 \tag{2.50}$$

where ϵ_0 and σ_0 are initial strain and stress, respectively. An element is called isoparametric if the same nodal points are used to define the shape functions as are used to describe

the geometry of the element. In isoparametric triangular and quadrilateral elements the displacement functions are linear and stress and strain are thus constant in each element.

For each element a set of finite element equations is obtained. These can be constructed with the displacement method, in which the external and internal work done by various forces and stresses during an arbitrary virtual nodal displacement are equated. The displacement formulation is equivalent to minimisation of the total potential energy of the system [*Zienkiewicz,* 1977]. The potential energy is minimum for a body in a state of equilibrium. The general form of the set of equations is:

$$K_e u = F_e \tag{2.51}$$

where F_e is the force vector and K_e the stiffness matrix:

$$K_e = \int_e B^T D B \tag{2.52}$$

The subscript e indicates element. The set of equations can thus be written:

$$\int_e B^T D B u = \int_e B^T \sigma = F_e \tag{2.53}$$

The equations for each element are assembled into a set of equations for the whole body. In the direct stiffness method this assembly is achieved by matching the displacements at the nodes, while loads and stiffnesses are added. The resulting system of equations is solved for displacements, whereafter strains and stresses can be obtained (equations 2.49 and 2.50).

To obtain time-dependent solutions the set of finite element equations has to be solved for each time step. The time stepping can be done with an explicit or an implicit solution algorithm. The explicit algorithm [*Zienkiewicz and Cormeau,* 1974], is not stable for all time steps. In contrast, the implicit algorithm [*Zienkiewicz,* 1977; *Hughes and Taylor,* 1978] is unconditionally stable, and, therefore, allows larger timesteps. With the latter method, however, the stiffness matrix needs to be recalculated in each time step, while with the explicit method the stiffness matrix is just formulated once, saving computational time.

2.3.2 Comparison with analytical results

Incompatible elements

To test the validity of using the finite element code TECTON for solving flexure problems, results are compared with the analytical solution for the problem of a continuous elastic plate bending under a lineload (see section 2.2.2). The analytical deflection profile is obtained by solving the differential flexure equation (2.2), which is derived under the following assumptions (see also section 2.1): 1) the plate is thin, 2) the deflections are small, 3) the bending is plane strain (ϵ_{yy} = 0, see Fig. 2.15 for orientation of coordinate axes), 4) the principal stress normal to the plate surface is zero (σ_{zz} = 0), and 5) plane sections remain plane. The resulting solution describes the deflection of the midplane of the plate. This means that in the finite element models also the deflection of the midplane has to be monitored. For all finite element results shown in this section the left and right hand side of the

parameter	symbol	value	unit
plate density	ρ	2800	kg m^{-3}
mantle density	ρ_m	3250	kg m^{-3}
Young's modulus	E	10^{11}	Pa
Poisson's ratio	ν	0.25	
gravitational acceleration	g	9.81	m s^{-2}

Table 2.2: Modelling parameters

models are held fixed. With the density-stripping method [*Braun,* 1988] gravity is removed from the mechanical equilibrium equations (2.1) and replaced by Winkler restoring pressures at the top and bottom of the plate [*Williams and Richardson,* 1991]. This method is a good approximation to a full stress model as long as the slopes of density interfaces do not change too much. The finite element grid is rectangular with 4-node elements. Modelling parameters which remain the same for all models are shown in Table 2.2, while the values of variable parameters are given in the captions of the related figures. Fig. 2.15 compares the analytical with the plane strain numerical solution for a plate thickness of 1 km and a lineload of -2×10^{10} N m^{-1}. The difference between the numerical and the analytical solution is on average very small and becomes largest, ≈ 0.4 m, near the point of application of the lineload. From a comparison of solutions of TECTON with an analytical solution of *Hetényi* [1946], *Beekman* [1994] concluded that the finite element model shows an overly stiff behaviour. This is caused by the fact that the element of which the mesh is composed, a simple four node quadrilateral, cannot correctly represent pure bending. In contrast, a stiffer behaviour of the numerical solution is not observed in the comparison made here. The improvement can be explained by referring to the dimensions of the finite element mesh: with smaller element widths the numerical results will better approach the correct bending solution (see also next part of this section). However, since a finer grid leads to a larger system of equations, this approach is not always the most practicable. For a coarser grid correct bending behaviour can be obtained by introducing incompatible elements [*Wilson et al,* 1973; *Taylor et al,* 1976; *Beekman,* 1994]. An improvement of the element is obtained by adding two extra displacement modes with which internal degrees of freedom are associated. The unknowns associated with these incompatible displacement modes are eliminated at the element level. Therefore, only the element stiffness matrix has to be modified, while the structure of the rest of the finite element program remains unaltered. The main advantage of incompatible elements is that correct bending behaviour is obtained for a reduced number of nodal points in the finite element mesh; this is illustrated in Fig. 2.16.

Accuracy

The difference between numerical and analytical solution is related to curvature (Fig. 2.15b). It increases with (absolute value of) curvature. This arises because the finite element method employed here results in linear displacements, which are less well able to reproduce high curvature deflections. It can, therefore, be expected that the fit of the numerical to the

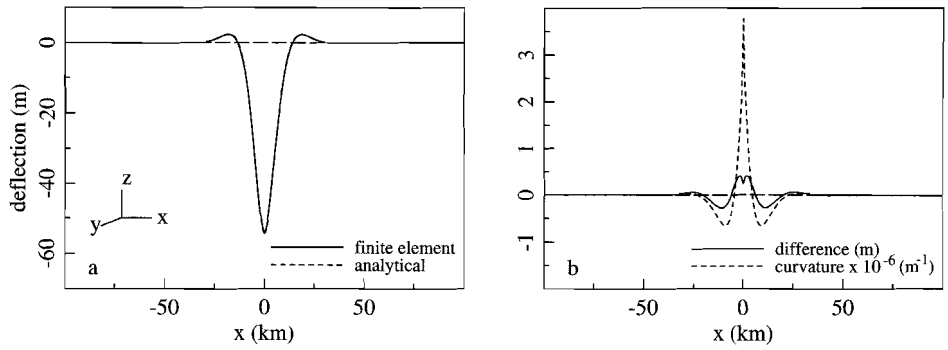

Figure 2.15: Comparison of finite element and analytical solutions for a continuous plate (thickness of 1 km) bending under a lineload of -2×10^{10} N m^{-1}. The finite element mesh consists of 10 cells vertical and 998 cells horizontal over a length of 400 km. Regularly dashed line denotes zero value. a) Computed deflections (of the midplane of the plate), b) Difference between the two solutions.

analytical solution will improve with smaller and deteriorate with larger element widths. Fig. 2.17 shows that this is indeed the case. The improvement obtained with incompatible elements is illustrated in the same figure. The model with incompatible elements shows an optimum in performance in the studied element width range. The observed increase in the difference with the analytical solution with decreasing element width after the optimum appears to be related to the aspect ratio of the elements. The remedy of adding incompatible displacement modes to improve the bending behaviour of the elements works best for elements which have a large width relative to their height. The results of Fig. 2.15 were generated with compatible elements with a width of 400.8 m.

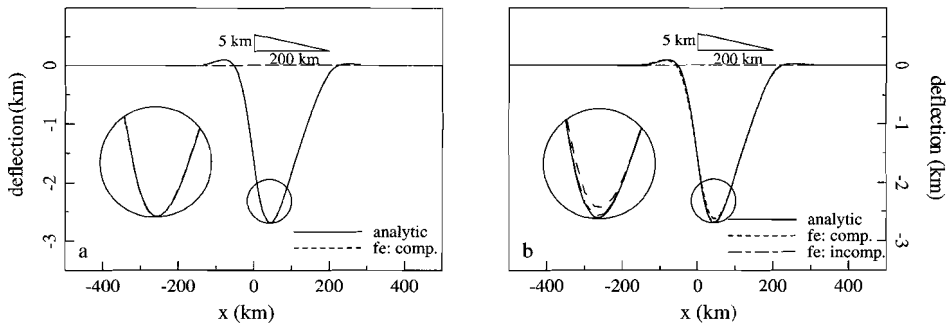

Figure 2.16: Comparison of finite element with analytical solutions for an elastic plate loaded by a triangular wedge. Analytical solution is of *Hetényi* [1946]. Plate thickness = 10 km, dimensions of the wedge are shown in the figure. Regularly dashed line denotes zero deflection. a) Element height $\times$ width = 100 $\times$ 1202.4 m, L_2-error compatible elements = 67.8 m. b) Element dimensions: 100 $\times$ 10000 m, L_2-error compatible elements = 127.9 m, incompatible = 10.5 m.

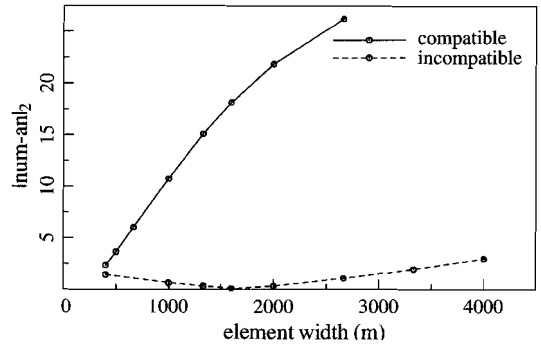

Figure 2.17: Difference in L_2-norm between the finite element and analytical solutions as a function of element width. Solutions are for a continuous elastic plate bending under a lineload. Plate thickness = 1 km (10 cells vertical), F = -2 $\times 10^{10}$ N m^{-1}, horizontal length of model = 400 km.

The number of elements in the vertical direction also influences the accuracy of the finite element solution. Since the stress in each element is constant (section 2.3.1), a model of one element layer thick cannot reproduce the stress state in a bending plate (where, for example, compression at the top of the plate changes to extension at the bottom, for a region bending downward). Increasing the number of elements allows a better approximation of the vertical stress profile. Fig. 2.18 shows that already with only four element layers the accuracy of the numerical solution is much improved.

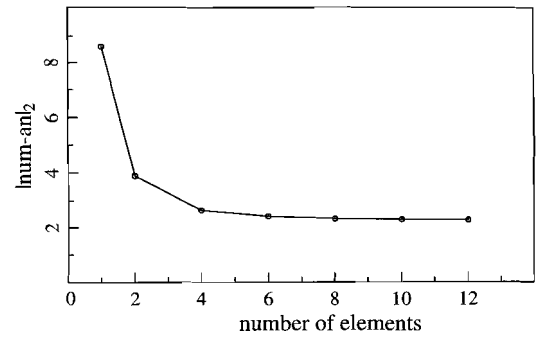

Figure 2.18: Difference in L_2-norm between the finite element and analytical solutions as a function of the number of elements in the vertical direction. Plate thickness = 1 km, plate length 400 km, fixed cell width = 400.8 m, F = -2 $\times 10^{10}$ N m^{-1}.

The analytical solution, with which the finite element solution is compared, is derived under the assumption that the plate extends infinitely in the horizontal x-direction. This condition can, of course, never be fulfilled by a numerical method. As the length of the numerical model decreases, the influence of the boundary conditions on the solution will increase, and the fit of the numerical to the analytical solution will deteriorate. This is

illustrated in Fig. 2.19. For plate lengths around 30 km, the numerical solution only shows negative deflections, it does not generate the positive flexural bulges. The misfit in the region of the flexural bulges can, therefore, not be taken into account, causing the apparently improving fit for these plate lengths.

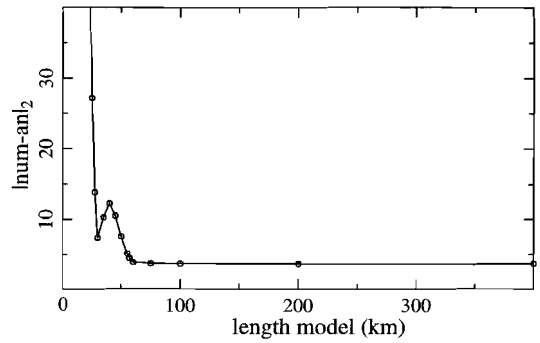

Figure 2.19: Difference in L_2-norm between the finite element and analytical solutions as a function of plate length. Plate thickness = 1 km (10 elements vertical), F = -2 $\times 10^{10}$ N m^{-1}, fixed element width = 500 m.

The accuracy of the finite element solution is thus influenced by the configuration of the model: the element width, element height and the length of the model are important. The accuracy of its fit to the analytical solution is also influenced by the ability of the finite element method to fulfill the approximations made in obtaining the differential equation that leads to the analytical solution. Of these approximations, the conditions of a thin plate, a plane strain situation and small deflections were fulfilled in the previous examples. The question is how well the numerical solution approximates the condition of zero vertical stress (σ_{zz} = 0). Fig. 2.20 shows that, for the case considered in Fig. 2.15, overall $\sigma_{zz} \ll \sigma_{xx}$, with which for this case the condition of vanishing vertical principal stress is reasonably well approximated. This could also be expected on the basis of the good fit of the numerical to the analytical solution.

Thick plates and large deflections

From this comparison of solutions of the finite element code with an analytical solution, it can be concluded that, for not too wide elements and a reasonably long plate, the numerical method gives reliable solutions to flexure problems. Since this method solves flexure problems without explicitly solving the differential flexure equation (equation 2.2), the influence of violating the approximations of a thin plate and large deflections can now be investigated. This is particularly of importance in the next chapter (3), where the finite difference method will be used to solve flexure problems involving relatively thick plates and large deflections. Since the finite difference method solves the same differential equation that is solved to obtain the analytical solution considered in this section, it is assumed that possible effects on

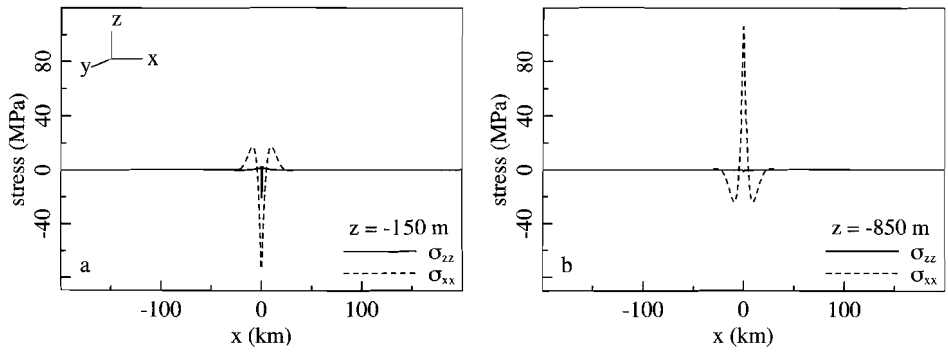

Figure 2.20: σ_{xx} and σ_{zz} versus horizontal distance for the finite element solution shown in Fig. 2.15. Plate thickness is 1 km. The stresses are shown at two levels: a) z = -150 m, b) z = -850 m.

the difference between the finite element and the finite difference solutions will be comparable to effects on the difference between the finite element and the analytical solutions. In the following part, it is also assumed that, for a model with small element widths and a long plate, a possible misfit between the finite element and the analytical solution is caused by not fulfilling one of the constraints of the differential flexure equation.

Fig. 2.21 shows the effect of increasing the maximum deflection on the difference between the finite element and the analytical solution. This difference is expressed in a stabilised relative L_2-norm:

$$\sqrt{\Sigma(\frac{w_{num} - w_{an}}{1 + |w_{an}|})^2} \tag{2.54}$$

where w is deflection and the summation is over all grid points on the midplane. The maximum absolute value of deflection, wmax, is divided by a measure L for the length of the plate (L is the length of that part of the profile that shows a significant deflection). The analytical solution is only correct for deflections much smaller than the length L of the plate. With increasing deflections, the analytical solution is, therefore, expected to less well approximate the real solution of the flexure problem. This is expressed in the increasing difference between the analytical and the numerical solution (Fig. 2.21). For large values of wmax/L, this difference seems to approach a constant value. It is, however, very probable that for these large deflections the finite element solution will not approximate the real solution very well either. This is due to limitations associated with the applicability of Winkler restoring forces for the high slopes associated with the large deflections. For very large deflections a comparison between the finite element and the analytical solution is, therefore, probably not very meaningful.

The other main limitation associated with the differential flexure equation is the constraint that the plate has to be thin compared with its length. In general, the thin plate solution is expected to give a good approximation to thick plate flexure (section 2.2.2). The effect of increasing plate thickness on the difference between the analytical and the finite

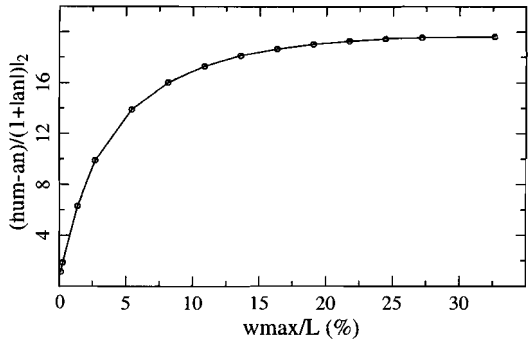

Figure 2.21: Difference between finite element and analytical solutions in a stabilised relative L_2-norm versus maximum deflection. The maximum deflection is given relative to a measure L for the length of the plate (see text). Plate thickness = 1 km, plate length = 400 km, 10 vertical elements and 998 horizontal.

element solution is shown in Fig. 2.22: the difference increases with plate thickness. The plate thicknesses in this figure may seem rather large, but relative to the plate length L the values are not larger than 4.2%.

For analytic and finite difference models that solve the differential flexure equation and, therefore, are subject to the constraints of small deflections and a thin plate, the following conclusions can now be drawn. Firstly, for the elastic plate thicknesses employed in models (usually around 10-40 km, but 100 km at most), the constraint of a plate thin relative to its length is easily fulfilled. Secondly, for models with large deflections the accuracy of the solution will become less. However, for moderately large deflections, with wmax/L $< 5\%$, the effect on the accuracy of the solution is not expected to be very large.

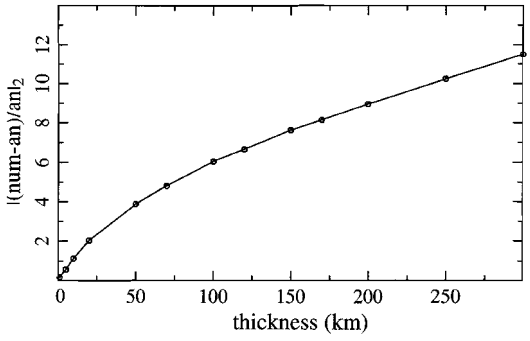

Figure 2.22: Difference between finite element and analytical solutions in a relative L_2-norm versus plate thickness. wmax/L = 0.001, length of numerical model divided by the flexural parameter = 30, 10×998 elements.

2.4 Conclusions

Both numerical methods that are discussed in this chapter, the finite difference and the finite element method, yield reliable solutions to lithosphere flexure problems. With the finite difference method the differential flexure equation is solved and the method is, therefore, subject to the assumptions associated with this equation. Only the assumptions of a thin plate and small deflections are not automatically fulfilled and care, therefore, has to be taken to adhere to these restrictions. The accuracy of the method is influenced by the chosen discretisation (the stepsize) and the plate length. For a plate with an elastic-perfectly plastic rheology the effective elastic rigidity decreases with intraplate stress. However, the effect of intraplate stresses on a plate with an elastic-plastic rheology characterised by a yield stress envelope is to increase the effective elastic rigidity: the plate thus behaves stiffer.

The finite element procedure solves the mechanical equilibrium equation for displacements using linear shape functions. As a consequence, the accuracy of the method is determined by element width and number of elements in the vertical direction for reasonable plate lengths (approximately 10 times the flexural parameter). For large element widths the bending behaviour improves with incompatible elements. By comparing analytical solutions with the independently obtained finite element solutions, the consequences of not rigidly adhering to the constraints of a thin plate and small deflections were evaluated. It can be concluded that, for the values of plate thickness and deflections typically used in models for flexure of the lithosphere, the effect of not strictly keeping to these restrictions will be very small.

Chapter 3

The role of subduction in the evolution of the Apennines foreland basin

3.1 Introduction

The Mediterranean region is the locus of convergence between Africa and Europe. This results in a complex pattern of subduction- and collision zones, part of which is formed by the Tyrrhenian-Apennines system (Fig. 3.1). The origin of this system, with compression in the Apennine thrust belt adjacent to extension in the Tyrrhenian Sea, is related to the westward subduction of the Adriatic plate beneath Italy. In Calabria, in the south, subducted lithosphere is delineated by the hypocentra of earthquakes below the Tyrrhenian basin [e.g., *Ritsema,* 1972; *Anderson and Jackson,* 1987; *Giardini and Velona,* 1991], but the presence of several hundreds kilometres of subducted lithosphere can be inferred along all of the Italian-Adriatic plate boundary [*Spakman,* 1990; *De Jonge and Wortel,* 1990; *Amato et al.,* 1993; *Spakman et al.,* 1993]. The extensional Tyrrhenian basin is created by roll-back of the subduction zone [*Boccaletti et al.,* 1976; *Malinverno and Ryan,* 1986; *Laubscher,* 1988; *Doglioni,* 1991,1993; a.o.]. The extensional effect of the roll-back process can be intensified by second order processes, such as the convergence of Africa and Europe [*Boccaletti et al.,* 1982; *Mantovani et al.,* 1993] and gravitational collapse of the post-collisional Alpine crustal wedge [*Channell and Mareschal,* 1989; *Faccenna et al.,* 1996].

The foreland basin of the Apennine mountains lies along the eastern side of the mountain belt. In this paper the term 'foreland basin' is used to denote the sedimentary basin that lies on the subducting Adriatic plate in front of the advancing Apennine thrust belt (Fig. 3.2). Although a foreland basin is usually not associated with a subduction zone set-

[1]Reprinted from *Tectonophysics, 296,* S.J.H. Buiter, M.J.R. Wortel and R. Govers, The role of subduction in the evolution of the Apennines foreland basin, p. 249-268, 1998, with permission from Elsevier Science.

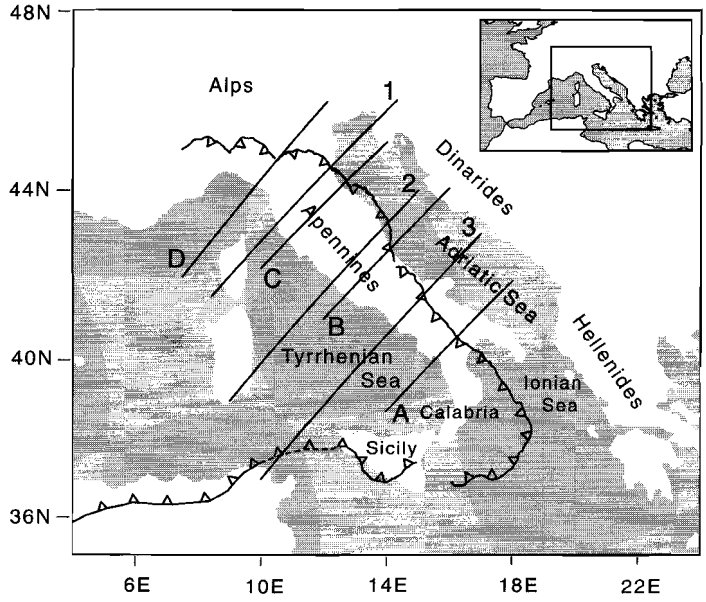

Figure 3.1: Map of Italy, barbed line: outermost thrust front, straight lines: the modelled sections (1,2,3: this study, A-D: data from *Royden* [1988]).

ting, this terminology is in agreement with existing literature on this region. The basin is a rather deep basin adjacent to a moderately high mountain belt: the Plio-Pleistocene foreland basin locally contains up to 9 km of sediments, whereas the Apennine mountains are at most 2 km high. Previous studies have shown that the topographic load is insufficient to cause such a deep basin and that additional subsurface loads must be present [*Karner and Watts,* 1983; *Royden and Karner,* 1984; *Royden et al.,* 1987]. The subsurface loads are most likely associated with subducted Adriatic lithosphere. We consider the Apennine foreland basin to result from flexural downbending of the subducting Adriatic lithosphere, combined with the subsidence caused by the surface loads, i.e. the load of the thrust belt, water and sediments. Variations, in space and/or time, in the load associated with the subducted plate (the slab pull) will, therefore, affect the configuration of the foreland basin. The hypothesis of lateral migration of slab detachment of *Wortel and Spakman* [1992] predicts such variations in slab pull along strike of the Apennines. This hypothesis is based on tomographic studies of the Mediterranean region [*Spakman,* 1990], which show evidence for a gap in the subducted Adriatic lithosphere at 100-200 km depth. According to *Wortel and Spakman* [1992], this detachment of the slab started in the north and migrated south/southeastward with time, causing temporal and spatial variations in the slab pull. The process is illustrated in Fig. 3.3. As detachment proceeds, the gravitational pull of the detached part of the slab is transferred to the undetached part. This leads to an increase in the effective slab pull exerted by the undetached slab. A deepening of the foreland basin and a more pronounced outward

migration of the trench, relative to the situation where only the roll-back process is active, are, therefore, expected above the undetached slab. Where and when the slab is detached, the slab pull decreases, leading to a shallowing of the foreland basin.

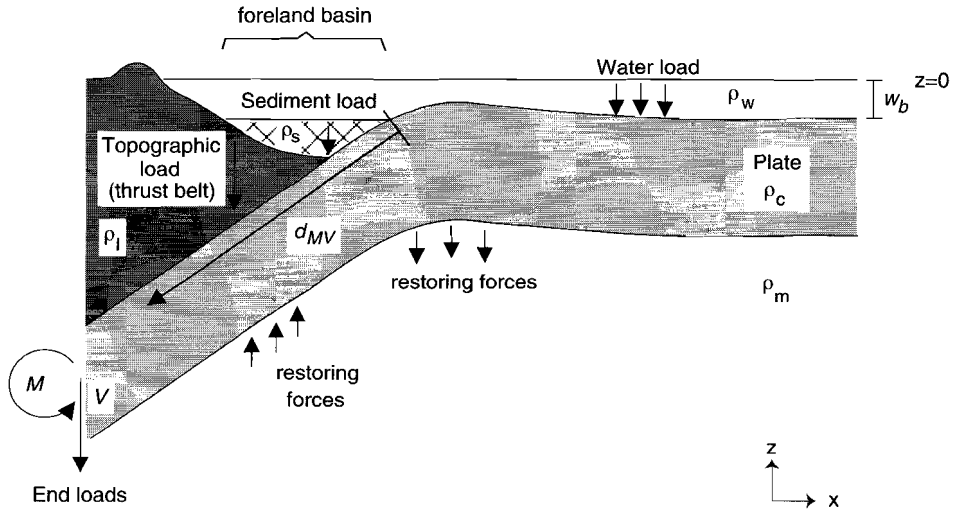

Figure 3.2: Loads involved in plate flexure; densities of the different materials are indicated: m mantle, w water, c crust, s sediment, l topography. w_b is the height of the layer above the surface of the flexing plate, in this figure this layer is a water layer, but it can also partly or completely consist of sediments. d_{MV} denotes the location for which values for the end loads are reported. Figure is not to scale.

It is the aim of this paper to test whether the effects of a laterally propagating tear in the subducting plate are in accordance with observations from the Plio-Pleistocene foreland basin. In particular, we study variations in the vertical loads along the convergent plate margin of Italy. To this purpose the flexural response of the foreland basin is studied in two-dimensional sections perpendicular to the strike of the Apennines (Fig. 3.1). In this way, NW-SE trends can be investigated. By incorporating published geophysical data, for example, crustal thickness and topography, and constraining the model to fit deflection and gravity anomaly data, the unknown slab pull is quantified for each section. Rather than an attempt to discriminate between various proposed tectonic scenarios for the Italian region, our study should be viewed as an attempt to test the predictions of one of these scenarios, the hypothesis of lateral migration of slab detachment. The implication of this approach is that the hypothesis will be rejected if the results of our work fail to match the predictions. If, however, the hypothesis survives our test, we recognise the possibility that alternative scenarios may also explain the observations we use. In that case, further tests will have to be developed to discriminate between competing hypotheses.

In a similar study, *Royden* [1988] matched results from a two-dimensional, elastic model to observations of plate flexure and gravity anomalies, for four sections across the Apennine

foreland basin. The values reported by *Royden* [1988] for the deep load can, however, not be compared between the different sections, since the load was not measured at the same point along the deflection profiles. As such, these results give no indication of spatial variations in slab pull. We will, therefore, re-evaluate the models of *Royden* [1988], making improvements and extensions on the modelling approach.

Figure 3.3: Illustration of vertical motions resulting from lateral migration of slab detachment. A tear in the slab propagates from north to south. I: Undisturbed situation; II: The tip of the tear. The weight of the detached part of the slab is transferred to the undetached part, this leads to an increase in the effective slab pull. This is reflected in a deeper deflection of the surface. III: Detached slab. The slab pull decreases, leading to a rebound of the surface.

The main conclusion that can be drawn from the results of the present study is that the hypothesis of lateral migration of slab detachment cannot be shown to be consistent or inconsistent with the flexural response recorded in the Plio-Pleistocene foreland basin.

3.2 Modelling method

3.2.1 Geometry

The origin of the Apennine foreland basin is related to the flexural downbending of the Adriatic lithosphere, which is maintained by the deep load associated with the subducting plate in combination with the load of material overlying the plate. To obtain a quantification of all vertical loads, we employ a two-dimensional model (Fig. 3.2) to sections perpendicular to the strike of the Apennines. Along strike variations can then be detected by comparing the results for the different sections.

There are various arguments for a continental character of the Adriatic lithosphere. It has a crustal thickness of approximately 30 km [*Nolet et al.,* 1978; *Meissner et al.,* 1987; *Ravnik et al.,* 1995] and a lithospheric thickness of about 100 km [*Calcagnile and Panza,* 1981; *Suhadolc and Panza,* 1989]. Also, the low to normal heat flow values are in agreement with a continental lithosphere [*Čermák,* 1979; *Loddo and Mongelli,* 1979]. The continental character is also supported by it probably originating from the former passive continental margin of Africa [*Channell et al.,* 1979]. There are indications that the continental lithosphere is involved in the Adriatic subduction. From tectonic reconstructions for the Mediterranean region [*Dewey,* 1989], we deduce that the depth of the ocean-continent boundary is well below our model. Subduction of a continental Adriatic lithosphere may have taken place by a delamination process, in which the upper crustal parts and the sediments are sheared off to form thrust sheets, while the lower crust with the lithospheric part of the mantle subducts [*Bally et al.,* 1986; *Panza and Suhadolc,* 1990; *Serri et al.,* 1993]. In agreement with this scenario, the Apennines are for the greatest part composed of continental rocks, only the uppermost units (Ligurides) are oceanic.

The Adriatic plate is covered by Mesozoic-Cenozoic sediments of variable thickness; on average the sedimentary layer is 10 km thick [*Morelli et al.,* 1969; *Nolet et al.,* 1978; *Calcagnile et al.,* 1982; *Mostardini and Merlini,* 1986]. In this study these old sediments are considered to be part of the crust.

3.2.2 Lithospheric flexure

For each section, the deflection of the Adriatic lithosphere is calculated from the one-dimensional flexure equation:

$$\frac{d^2}{dx^2} D \frac{d^2 w}{dx^2} + (\rho_m - \rho_o) g w = q \tag{3.1}$$

in which w is the deflection, q the vertical load, D the flexural rigidity, ρ_m and ρ_o the densities of the mantle and of material overlying the lithosphere, respectively, and g the gravity

acceleration. In our frame of reference, forces are positive upward and moments are positive counterclockwise. The equation is solved with a finite difference method. By using this equation, we implicitly assume that the length scale of variations in loads and rheology out of the plane of our section is significantly larger than the horizontal extent of the section. Also, the thickness of the model plate has to be much smaller than the wavelength of the flexure (thin plate approximation). The deflection of the top of our model plate is fitted to the base of the Plio-Pleistocene foreland basin of the Apennines. Model parameters (e.g. loads, densities, rheologies), which are not closely constrained by observations are being varied systematically in the modelling. A grid search technique is adopted to identify those model parameters which minimise the rms-difference between observed and computed deflections. We report the resulting best-fitting model parameters. We also show results of additional experiments where we fix all parameters, except one, to give the reader a sense of the sensitivity of our results to that specific parameter.

3.2.3 Loads and restoring forces

Fig. 3.2 summarises the vertical loads involved in lithospheric flexure at a convergent plate boundary. The surface loads are the topography, the sediments filling the basin and a water and/or sediment layer. It is assumed that these loads are completely supported by the subducting plate, which implies that an overriding plate is either not present in the studied region or mechanically too weak to support vertical loads. The boundary between the thrust belt and sediments is often diffuse, since sediments of former foreland basins can be incorporated in the advancing thrust belt. The deflected surface is covered by a layer of water and/or sediments of thickness w_b. Whether the sediments are deposited after or prior to flexure does not make a difference in our end-situation modelling (Fig. 3.4). The subsurface load (or deep load) is associated with the subducting plate. To limit the size of the model, this load is simulated by applying a bending moment M and a vertical force V at an artificial slab end; M and V are here referred to as 'end loads'. The unknown end loads are constrained in the modelling procedure. Besides vertical loading, the flexing plate can also be subject to (changes in) horizontal tension or compression [*Cloetingh et al.,* 1985; *Peper,* 1993]. For reasonable values of intraplate stress (tens of MPa) [*Bott,* 1991, 1993; *Wortel et al.,* 1991] and thick plates, the effect on the calculated deflection is, in general, not very large. In this study intraplate stress is, therefore, not taken into account.

Restoring forces arise from buoyancy, resulting from the replacement of mantle material underlying the plate by material of a lower density overlying the plate ($(\rho_m - \rho_o)gw$ in Eq. 3.1).

The main difference between the elastic model of *Royden* [1988] and the elastic model employed in this study is expressed in the way densities or density differences are handled (Fig. 3.5). *Royden* [1988] assumes that, initially, the top of the plate lies at a depth w_0 and that the plate is covered with water. The water overlying the plate is taken into account in the flexural calculations. Therefore, her restoring force equals $(\rho_m - \rho_w)gw$ and the topographic and sedimentary contributions to the loading of the plate below sea level are determined by the density difference with water (e.g. $(\rho_s - \rho_w)$). However, according to her Fig. 1 and the description of the load of the infilling material, *Royden* [1988] employs

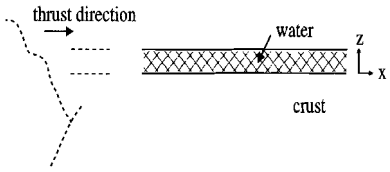

1. Initial situation

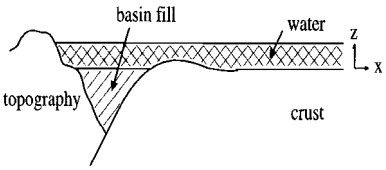

2. Plate flexure, basin is filled with sediments

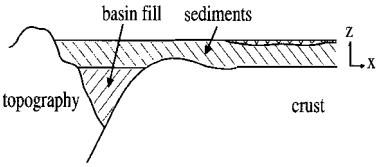

3. Sediments cover whole area

a

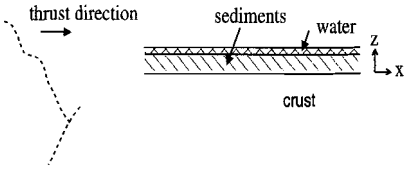

1. Initial situation

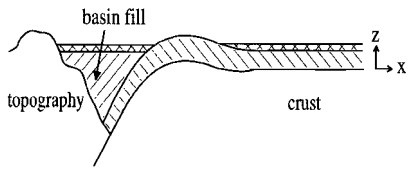

2. Plate flexure, basin is filled with sediments

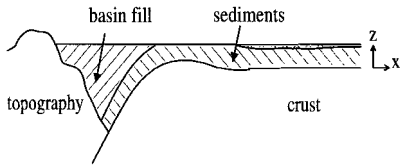

3. Sedimentation and erosion of bulge

b

Figure 3.4: The flexing plate is covered by a layer of sediments, these can be deposited after flexure (a) or prior to flexure (b). If it is assumed that the densities of the sediments are equal on average, the end situation of both figures is the same.

the density difference with water for material between sea level and w_0, and not for material below w_0 (Fig. 3.5). This approach is not consistent. It results in a higher density for the infilling material and, therefore, a larger load. Likewise, it is assumed in the study of *Royden* [1988] that the plate is covered with material with a crustal density ρ_c towards the subduction zone. In this case the restoring force equals $(\rho_m - \rho_c)gw$ and the loads on the plate are determined by the density difference with the crustal material. For material between sea level and w_0, *Royden* [1988], however, still uses the density difference with water [see also *Kruse and Royden,* 1994]. This again results in a load which is too large. In the model employed in this study we do not incorporate the material covering the plate through the restoring force, but explicitly include the load of all material above the plate in the loading term. In our case, the restoring force equals $\rho_m gw$. In this way we avoid an inconsistent treatment of the loads.

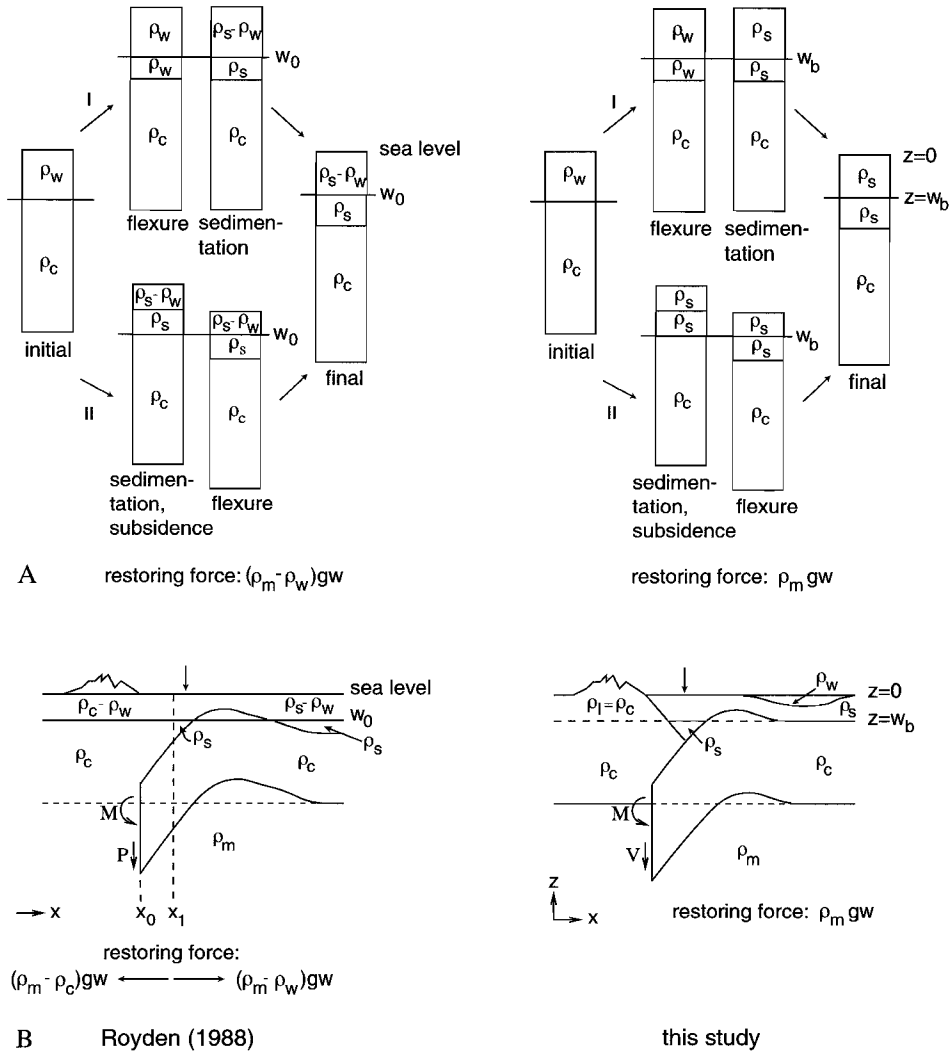

Figure 3.5: Schematic representation of two models, left: *Royden* [1988], right: this study; a) Densities in the initial and final situation. The two scenarios (I and II) lead to the same final situation. The last column includes the subsidence caused by sediments added in the previous step. The left figure shows that *Royden* [1988] is not consistent with the densities used in determining the loads and the restoring force; b) The models. The arrow at the top indicates the location of the column shown in a). The left figure is taken from *Royden* [1988]. Densities of the different materials are indicated: m mantle, c crust, s sediment, l topography, w water.

3.2.4 Rheology

We first model the configuration of the foreland basin with an elastic plate rheology; this facilitates a comparison with the results of *Royden* [1988]. Models employing an elastic plate can, in general, match first order characteristics of observed deflection profiles [e.g., *Caldwell et al.,* 1976; *Jordan,* 1981; *Karner and Watts,* 1983]. Combined with the relatively simple calculations, this explains the frequent usage of an elastic plate model. However, the representation of continental lithosphere by an elastic plate of constant thickness means a substantial approximation, although relations between effective elastic plate thickness and lithospheric parameters can be derived [*Burov and Diament,* 1992; *Ranalli,* 1994].

Therefore, we approximate the rheology for the continental Adriatic lithosphere (hereafter referred to as 'continental rheology') by an elastic-plastic rheology (Fig. 3.6). The

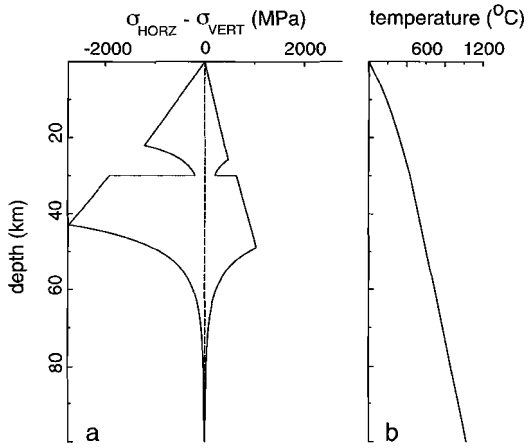

Figure 3.6: a) Continental yield rheology for $\dot{\epsilon} = 10^{-14}$ s^{-1} and geotherm as in b. Compression is negative. b) Continental geotherm following *Chapman* [1986] (surface heatflow 55 mW m^{-2}, Moho depth 30 km).

yield stress in the brittle regime follows Byerlee's law, ductile yielding is described by power law creep. The deflection of a plate with a continental rheology is obtained by iterative solution of the flexure equation (Eq. 3.1) with an effective elastic flexural rigidity:

$$D_{eff}(w) = \frac{M_{tot}}{-w''} = \frac{\int_H \sigma(z) z dz}{-w''} \tag{3.2}$$

where $-w''$ is curvature, $\sigma = \sigma_{horz} - \sigma_{vert}$, z is depth and H is the thickness of the mechanically strong part of the lithosphere [e.g. *Burov and Diament,* 1992; see also *Bodine et al.,* 1981; *McAdoo et al.,* 1985 for the case of an oceanic rheology]. This is purely a modelling parameter representing the rigidity of an elastic plate which adequately simulates the observed bending behaviour. In general, D_{eff} will vary laterally. The effective elastic flexural rigidity depends on the variation of yield stress with depth, and therefore, on the

parameter	symbol	value	unit
Moho depth[a]		30	km
surface heat flow[b]	Q_s	55	mW m^{-2}
Young's modulus	E	10^{11}	Pa
Poisson's ratio	ν	0.25	
strain rate	$\dot{\epsilon}$	10^{-14}	s^{-1}
coefficient of friction	μ	0.577	
pore-fluid factor	λ	0	
densities			
crust	ρ_{crust}	2800	kg m^{-3}
mantle	ρ_{mantle}	3250	kg m^{-3}
universal gas constant	R	8.31	JK^{-1} $mole^{-1}$
power law creep - crust[c]			
pre-exponent[d]	A_{pl}	1.23×10^{-23}	s^{-1} $Pa^{-3.2}$
activation energy	Q_{pl}	238.6	kJ $mole^{-1}$
power	n	3.2	
power law creep - mantle[e]			
pre-exponent[d]	A_{pl}	2.87×10^{-25}	s^{-1} $Pa^{-4.48}$
activation energy	Q_{pl}	498	kJ $mole^{-1}$
power	n	4.48	

[a] [*Nolet et al.,* 1978; *Meissner et al.,* 1987; *Ravnik et al.,* 1995]
[b] [*Čermák,* 1979]
[c] dry anorthosite [*Shelton and Tullis,* 1981]
[d] modified to ensure validity of PL creep for a general state of stress [*Ranalli,* 1987] and for a thin flexing plate
[e] wet Aheim dunite [*Chopra and Patterson,* 1981]

Table 3.1: Parameters defining lithospheric rheology.

thermal state, crustal thickness and strain rate, and on plate curvature and stress [*Karner et al.,* 1983; *McNutt et al.,* 1988; *Burov and Diament,* 1992, 1995]. Increased yielding through an increase in curvature or horizontal stresses will lead to a decrease in effective rigidity. Mechanical decoupling of the crust and mantle at substantial amounts of bending [*De Rito et al.,* 1986; *McNutt et al.,* 1988; *Burov and Diament,* 1995] is implicitly incorporated in our simulations. Rheological parameters that were used in this study are listed in Table 3.1.

3.2.5 Gravity anomalies

An additional constraint on the different models can be provided by requiring calculated gravity anomalies to fit observational gravity data. Bouguer gravity anomalies are calculated using the polygon method of *Talwani et al.* [1959]. As a reference model, the undisturbed situation, i.e. the foreland in the models, is used. We do not a priori incorporate slab

detachment in our models and, therefore, we use a continuous subducted plate in the calculation of gravity anomalies. In this aspect our method differs from *Royden* [1988], where a fit to the gravity data is obtained by varying the location of an effective end of the subducted lithosphere. The contribution to the gravity anomaly of slab material that is possibly present beyond the effective slab end is neglected in Royden's approach.

3.3 Data

3.3.1 Model input data and constraints

The calculated deflection is fitted to the base of the Plio-Pleistocene foreland basin. The thickness of the Plio-Pleistocene sediments is taken from the map 'The neotectonic model of Italy' [*Ambrosetti et al.,* 1987] for sections 1, 2 and 3. The data are averaged over an interval of 0.2 degrees and recalculated to depth below the surface z = 0 (Fig. 3.2). The loads of the thrust belt and the water layer are constrained by topographic and bathymetric data, respectively (ETOPO5), while the sediment load is constrained by the base of the Plio-Pleistocene foredeep. For sections A through D, deflection and gravity data from *Royden* [1988] are used.

3.3.2 Regional considerations

It is assumed that the horizon that at present forms the base of the Plio-Pleistocene foredeep was initially deposited horizontally. In this case, the present shape of the base of Pliocene level is the result of processes acting from the Early Pliocene to present. If the process of slab detachment would be occurring at present, differences in slab pull along strike of the Apennines could be expected. However, it is possible that the slab has already been detached along most of Italy from Late Miocene to present [*Wortel and Spakman,* 1992]. Also, detachment possibly occurred very recently (Quaternary) beneath the southern Apennines and Calabria [*Westaway,* 1993; *Hippolyte et al.,* 1994]. Therefore, depending on the timing of slab detachment, the base of Pliocene level at different locations along the coast of Italy, was deposited before, during or after slab break-off. The base of Pliocene level experienced a different tectonic history in these different settings, which influences the present configuration of this level. Therefore, different loads are necessary to reproduce a post- or a pre-slab detachment deposited level. Along strike differences in slab pull and/or surface loads (i.e. sediments, topography and water) are therefore expected. Since slab detachment probably occurred relatively recent in south Italy, it can be expected that in the south the base of Pliocene level has been deposited before slab break-off, while in the north this same level may have been deposited after slab detachment occurred.

The Apennine thrust belt-foreland basin system migrates eastward with time, the amount of migration increases towards the south [*Bally et al.,* 1986; *Boccaletti et al.,* 1990a]. The cause of roll-back could be an increase in slab pull, in which case the effects of changes in vertical loads and of horizontal migration are coupled, or it could be escape tectonics [*Mantovani et al.,* 1993]. Outward migration will cause a deepening of the sediment horizons in

parameter	symbol	value	unit
Moho depth		30	km
gravity acceleration	g	9.81	$m\ s^{-2}$
densities			
crust	ρ_c	2800	$kg\ m^{-3}$
mantle	ρ_m	3250	$kg\ m^{-3}$
water	ρ_w	1000	$kg\ m^{-3}$
topography	ρ_l	2800	$kg\ m^{-3}$
sediment	ρ_s	2300	$kg\ m^{-3}$

Table 3.2: Fixed input parameters

the basin. If this effect is not taken into account, it can be expected that a larger amount of migration will be reflected in a larger modelled loading. Since we do not include roll-back in our models, we have to bear this in mind when interpreting the results.

We also have to keep in mind that in the modelling it is implicitly assumed that the base of Pliocene is only deformed by flexure. It is, however, possible that this level is also disturbed by thrusting [*Ricci Lucchi,* 1986; *Ori et al.,* 1986].

3.4 Results

3.4.1 Elastic rheology

Deflection

To determine the best fit to the base of the Plio-Pleistocene foredeep for each of the seven sections shown in Fig. 3.1, the following quantities were varied: elastic plate thickness, sediment density, the depth of the baseline, and the end loads, *M* and *V*. In most of the models a sediment density of 2300 kg/m^3 gave the best results. This agrees with the average density found for Plio-Pleistocene sediments, which is around 2250-2350 kg/m^3 [*Mostardini and Merlini,* 1986]. Therefore, all figures will show results for a sediment density of 2300 kg/m^3. Values of fixed input parameters are shown in Table 3.2. The results of modelling with a completely elastic plate are shown in Fig. 3.7. For these best fits, the values of plate thickness, baseline, the end loads and the surface load are given in Table 3.3. In this study, these end loads are always measured at the same location to allow a comparison between different model results. Values are given for a point located at a fixed distance, measured along the plate, from the first point of zero deflection (d_{MV} in Fig. 3.2). Since the magnitude and sign of bending moment and shear force vary with distance along the bending plate, it is possible that the sign of the measured values differs from that of the applied end loads. A measure for the surface load is obtained by integrating the loads of topography, sediments and water over plate length.

For sections 1, C and D a reasonable fit to the base of the foredeep can be obtained with different elastic plate thicknesses. From the values in Table 3.3 it can be seen that a trade-off

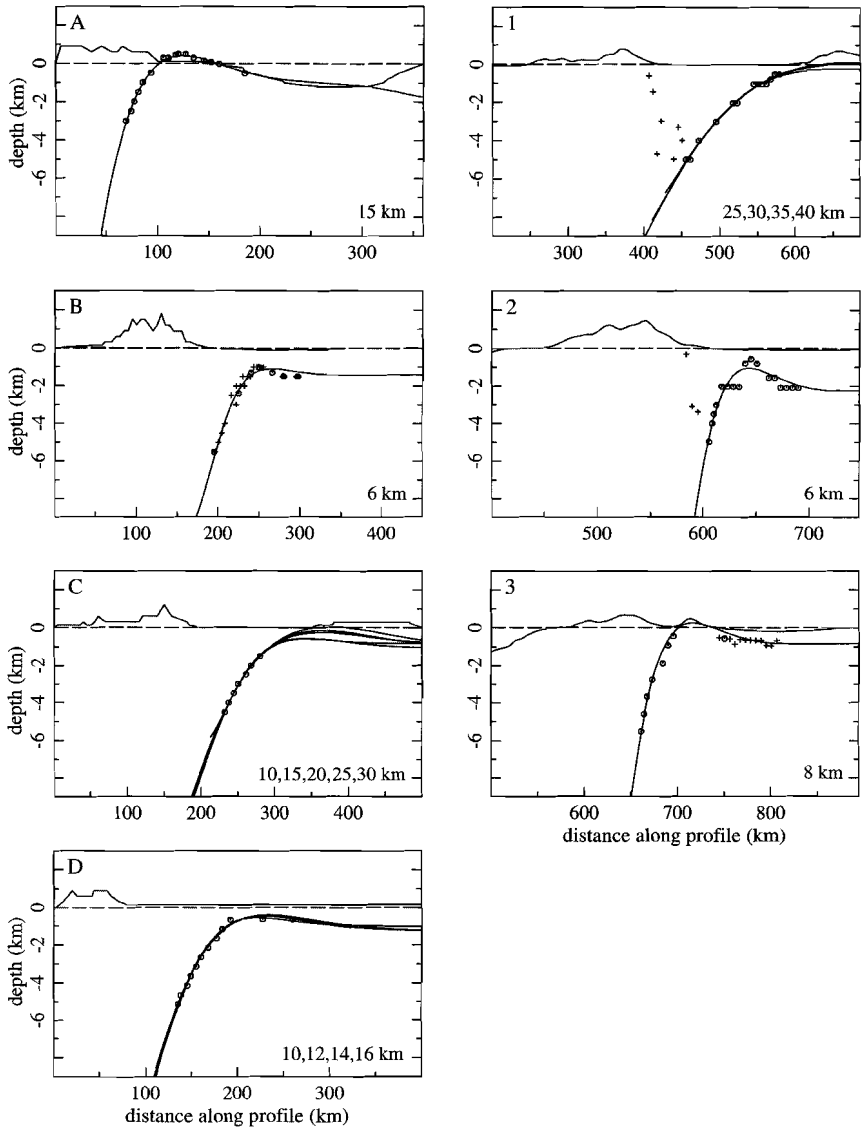

Figure 3.7: Solutions with an elastic rheology for each of the sections shown in Fig. 3.1. The values for elastic plate thickness are shown in each frame. The base of the Plio-Pleistocene foredeep is indicated with small circles. The crosses also indicate base of Pliocene: on section B for parallel profiles, on 1 and 2 the overthrusting side and on 3 values which were not used in calculating the rms-difference with the modelled deflection.

Section	elastic thickness (km)	baseline (m)	V (10^{11} Nm^{-1})	M (10^{16} N)	surface load ($\int q_{surf} dx$) (10^{13} Nm^{-1})	rms-diff[a] (m)
A	15	2200	33.4	35.5	-3.78	99
B	6	1400	-6.39	-0.48	-0.52	232
C	10	800	-4.41	0.54	-0.42	74
	15	1000	-2.91	3.34	-0.84	63
	20	800	-0.41	6.79	-1.51	57
	25	1000	3.49	14.6	-2.62	56
	30	1000	7.77	23.0	-3.26	58
D	10	1000	-7.80	1.06	-0.37	152
	12	1000	-6.70	2.54	-0.43	144
	14	1200	-5.34	5.02	-0.59	148
	16	1200	-3.68	6.90	-0.73	147
1	25	600	1.35	6.16	-0.65	133
	30	400	2.91	9.01	-0.75	133
	35	400	5.56	14.5	-1.03	131
	40	600	8.72	22.4	-1.79	130
2	6	2200	-5.92[b]	2.01[b]	-0.52	338
3	8	800	0.80	6.50	-1.78	320

Table 3.3: Results for modelling with an elastic plate (V and M measured at d_{MV} = 60 km, see Fig. 3.2), [a]) $(\frac{1}{n}\sum_n (y_n - y_{dn})^2)^{\frac{1}{2}}$, [b]) d_{MV} = 45 km.

relation between elastic plate thickness and the end loads exists. For these sections the deep load can thus not be constrained from modelling with an elastic plate. In the next section it is demonstrated that this situation does not improve by incorporating gravity data in the models. For sections 2 and B the calculated deflection fails to fit the high in the data, even for a very low value of elastic plate thickness of 6 km. The issue of the sharp highs will be considered in more detail in the Discussion. The calculated deflection well fits the data for sections A and 3.

The best fitting model for each plate thickness is determined by the lowest value for the rms-difference between the calculated deflection and the base of Pliocene level. This method allows a good determination of the values of the end loads (Fig. 3.8). The values for the rheological parameters had to be adopted in the modelling ($E = 1 \times 10^{11}$ Pa, $\nu = 0.25$). In general, variation of these values either hardly affects the fit or leads to a worse fit. The results are most sensitive to the choice of Young's modulus E.

Gravity anomalies

By two-dimensional modelling of gravity anomaly data besides deflection data, it may be possible to distinguish between different elastic models that fit the deflection data (e.g. sections 1, C and D). While the data describing the base of the foredeep constrain a laterally limited portion of the calculated deflection profile, observed gravity anomalies are available

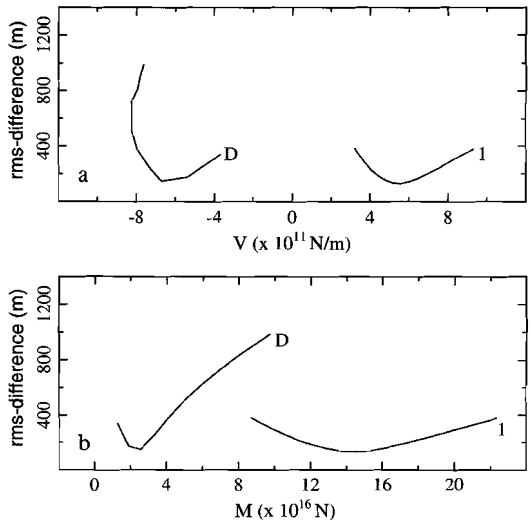

Figure 3.8: Minimum in rms-difference between calculated and observed deflection for two elastic models: D (plate thickness 12 km) and 1 (35 km). The values for the end loads, M and V, are measured at d_{MV} = 60 km. a) rms-difference against shear force V, b) rms-difference against moment M.

for a wider region, thus possible allowing a further constraint on the model. On average the range of the measured bouguer anomalies is from -80 to 40 mGal. If we assume an uncertainty in the order of 20 mGal (due to errors in the density for the bouguer correction, instrumental and reading errors) [see also *Wessel and Watts,* 1988; *Keating,* 1995] the data contain a significant signal. The bouguer gravity signal over this subduction zone is for the greatest part determined by the bending of the subducting plate. This bending determines the sedimentary basin and causes lateral density differences (e.g. between crust and mantle, sediment and crust). Similar deflection profiles will, therefore, lead to similar gravity anomalies. For example, for profile 1 the difference in calculated bouguer anomaly between the models with an elastic plate thickness of 30 and 40 km is at most 10 mGal. Assumptions concerning the values of densities, thickness of the crust and lithosphere and extrapolation of the deflection profile to greater depths have a much larger effect on the calculated anomaly than small differences in deflection. Fig. 3.9 illustrates this argument for variations in crustal thickness and extrapolation. *Royden* [1988] obtained a fit to the gravity data by varying the location of the effective end of the subducted lithosphere; slab material that is possibly present beyond the effective slab end does not contribute to the calculated anomaly. In the case of our example (Fig. 3.9) this approach leads to a reasonable fit. However, the presence of subducted material down to large depths in this region is apparent from tomographic studies [*Spakman,* 1990; *Spakman et al.,* 1993; *Amato et al.,* 1993]. It is not clear why slab material beyond the slab end should not contribute to the bouguer anomaly. The calculated bouguer gravity anomalies include the effect of the relatively thin crust of the Tyrrhenian Sea (related to its extensional origin). This positive contribution was calculated

using the depth of the Moho from the map 'The neotectonic model of Italy' [*Ambrosetti et al.*, 1987].

Straightforward calculation of bouguer gravity anomalies from the obtained deflection models does not lead to a fit to the observed gravity data. We examined reasonable variations in different parameters: sediment density, crustal thickness, density of the lithospheric mantle, extrapolation of the deflection profile to greater depths and location of the boundary between thrust belt and sediments. Since similar deflection profiles lead to similar gravity anomalies, their difference is insignificant compared to the much larger effect of these variations. Therefore, it is concluded that including gravity data in the analysis does not help to discriminate between the different elastic models that fit the deflection data.

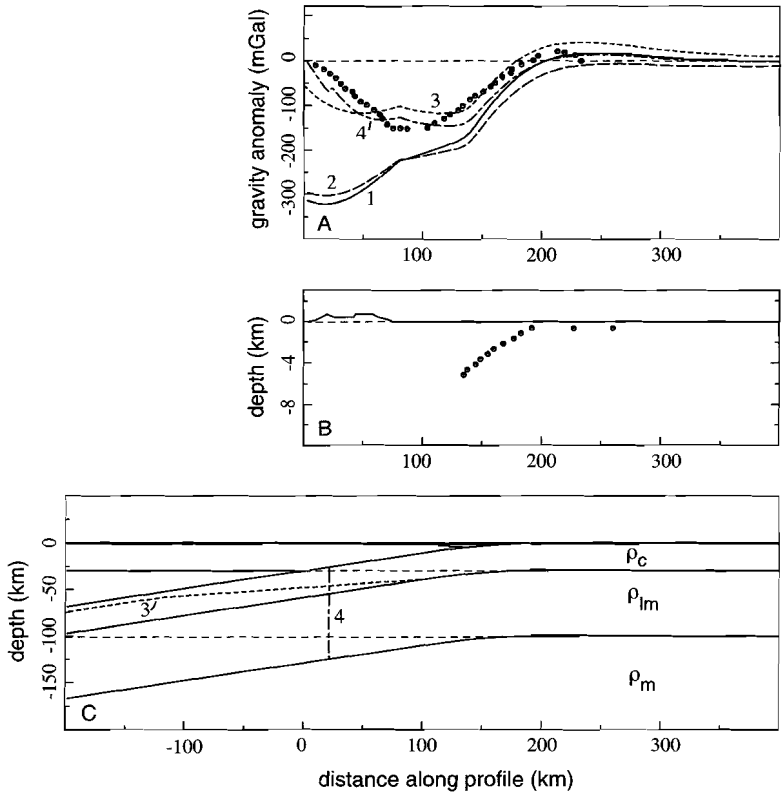

Figure 3.9: Effect of variations in crustal thickness, extrapolation and density of the lithospheric mantle on the bouguer gravity anomaly for section D. a) Bouguer gravity anomaly, small circles: data from *Royden* [1988], lines: calculated (elastic thickness 14 km, crustal thickness 30 km). $\rho_c/\rho_{lm}/\rho_m$: densities of crust/ lithospheric mantle/mantle. 1) $\rho_c/\rho_{lm}/\rho_m$=2800/3450/3250 kg m^{-3}), 2) $\rho_c/\rho_{lm}/\rho_m$=2800/3250/3250 kg m^{-3}), 3) decreasing crustal thickness, 4) effective end of subducted lithosphere. b) Deflection data. c) The (extrapolated) models.

3.4.2 Continental rheology

From the results of modelling with an elastic rheology we concluded that for some sections a fit to the deflection data can be obtained for a range in elastic plate thicknesses, while for other sections a fit can only be obtained for a very thin plate. Employing a more realistic continental rheology may possibly further constrain the solution and allow us to quantify the end loads. For each of the seven sections the best fit to the base of Pliocene level for a model with a continental rheology is shown in Fig. 3.10. The modelling parameters are given in Table 3.4.

Overall it can be stated that the plate with a continental rheology gives a worse fit to the deflection data than an elastic plate. For the large curvature values associated with the base of the foreland basin the effective elastic plate thickness locally rapidly reduces, this leads to an increase in bending. For smaller amounts of bending a flexing continental lithosphere is mechanically stiff. The continental model can, therefore, not reproduce the sharp highs on some of the sections (e.g. B, 2 and 3). A good fit is obtained for those sections which also allowed multiple elastic solutions (i.e. C, D and 1). However, due to the large difference in the quality of the fit to the data between the different sections (Table 3.4) a comparison of the obtained loads is not very meaningful. This implies that it cannot be shown whether laterally propagating slab break-off beneath Italy is compatible or incompatible with Plio-Pleistocene deflection data.

Our solutions are sensitive to the choice of values for the different rheological parameters, since these determine the variation of yield stress with depth (and therefore affect the effective elastic flexural rigidity). We considered variations in geothermal gradient (determined by surface heatflow), crustal thickness and ductile flow laws. The plate behaves stronger for an higher ductile yield stress or a smaller crustal thickness (the latter through a reduction of the lower crust ductile zone). This results in a worse fit in all cases. For a number of sections an improved fit could be obtained with a weakened plate. This is the case for sections 2, A, B and D with an higher surface heatflow and for sections B and D with a lower ductile yield stress. This agrees with our observation that the continental plate behaved too stiff to simulate the deflection data of central Italy. Considering the best fits from these variations does not significantly change the results of Fig. 3.10. Therefore, we conclude that the hypothesis of lateral migration of slab detachment cannot be shown to be consistent nor inconsistent with the flexural response recorded in the Plio-Pleistocene foreland basin.

3.5 Discussion

3.5.1 Causes for discrepancies between model results and data

The sharp highs observed in the deflection data for three of the sections (2, 3 and B) pose a problem in the modelling. For models with an elastic rheology a more or less reasonable fit could only be obtained for very thin plates; however, a small elastic plate thickness is not immediately expected on the basis of the continental character of the Adriatic lithosphere. The bending behaviour of the continental plate model is too stiff to simulate an

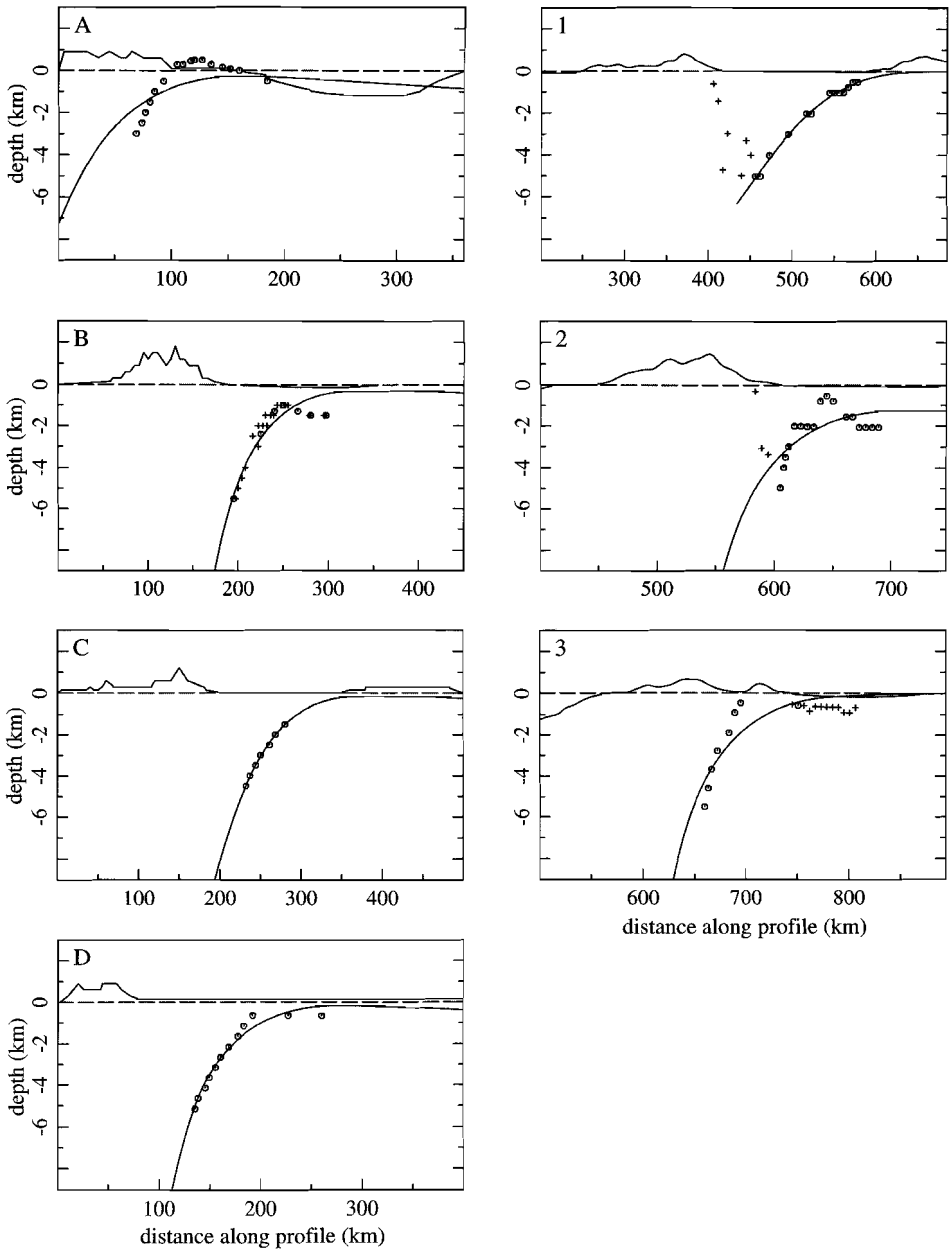

Figure 3.10: Solutions with a continental rheology for each of the sections shown in Fig. 3.1. Symbols as in Fig. 3.7.

Section	baseline (m)	V (10^{11} Nm^{-1})	M (10^{16} N)	surface load (10^{13} Nm^{-1})	rms-difference (m)
A	800	2.67	21.3	-3.52	687
B	800	5.86	21.7	-3.42	533
C	600	5.52	20.4	-1.93	53
D	800	6.51	21.9	-2.01	277
1	200	3.78	12.7	-0.75	131
2	1800	5.84	21.8	-4.11	788
3	200	8.16	5.34	-2.76	891

Table 3.4: Results for modelling with a continental plate (V and M measured at d_{MV} = 60 km, see Fig. 3.2).

high and sharp bulge. Nevertheless, a sharp high is observed in these sections and different explanations are possible. One explanation is that an high flexural bulge is maintained by intraplate compressive stresses. For purely elastic plates reasonable intraplate stresses (order of magnitude tens of MPa [*Bott,* 1991, 1993; *Wortel et al.,* 1991]) can lead to higher sharp bulges if the plate thickness and, therefore, the flexural wavelength is small. The flexural wavelength of models with a continental rheology is too large to lead to such small bulges. Also, intraplate compression only needs to be invoked for the sections through mid Italy, it is not clear what could be the mechanism that causes compression only in this region. Alternatively, a local weak zone in the foreland may localise and uplift the flexural bulge [*Waschbusch and Royden,* 1992]. For example, for section 2 a reduction in elastic plate thickness by a factor of 2 over a few tens of kilometres gives an acceptable fit to the high in the data. The same holds for section B (Fig. 9 of *Waschbusch and Royden,* 1992). For a plate with a continental rheology a local weak zone can also uplift the flexural bulge, but the plate remains too stiff to form such an high and small bulge as suggested by the data for sections 2, 3 and B. Therefore, we do not prefer introducing the undetermined feature of local weak zones in the models, but instead prefer a third explanation of the sharp highs in the data. This explanation is related to the implicit assumption in the modelling that the base of Pliocene level is only deformed by flexure and that the present shape of this level can thus be represented by a flexural model. However, the Plio-Pleistocene Adriatic foreland basin is affected by thrust deformation [*Ricci Lucchi,* 1986; *Ori et al.,* 1986; *Bally et al.,* 1986]. It is, therefore, very likely that in some regions the base of Pliocene level has been distorted by thrusting. The structure that has been implicitly interpreted as a flexural bulge on sections 2 and B is probably caused by a major fault structure (like the Struttura Costiera or the Contessa or Colosseo faults [*Ori et al.,* 1986, 1991]), and is not, or not completely, a flexural bulge. This would explain the difficulties that were met in modelling these sections. Also in the case of section 3 it is likely that the high is not only caused by flexure related to the Adriatic subduction zone. At the present location of the high an high structure has existed since at least the Oligocene [*Boccaletti et al.,* 1990b]. This cannot have been a flexural bulge of the Adriatic subduction zone at that time, since the outermost thrust front (and hence the trench) was then still located further to the west.

In this study only the westward directed subduction of the Adriatic plate beneath Italy has been considered; the Adriatic plate, however, also subducts eastward beneath the Dinarides and Hellenides (Fig. 3.1). These opposite vergent subduction systems can potentially influence one another [*Moretti and Royden,* 1988]. This may play a role in the southern Adriatic Sea, where the distance between the Apennine/Calabrian and the Hellenides subduction zones is decreasing southward (to approximately 300 km for section A). The deflection data for the different sections do, however, not show indications for influence of the eastern subduction system, not even for the southernmost section (A). *Moretti and Royden* [1988] modelled three sections through South Italy with an elastic plate subject to double sided subduction. Their fit for section A (their section 1) was obtained for a slightly thinner plate than in *Royden* [1988].

3.5.2 Comparison with Royden [1988]

For sections A through D data from Royden (1988) were used and, therefore, a comparison of results from the modelling with an elastic rheology to the results of Royden should, in principle, be possible. This is, however, not the case for sections C and D, since it was shown in this study that for these profiles a trade-off relation between elastic plate thickness and the end loads exists, which cannot be eliminated by the inclusion of gravity data. For both sections A and B the fit obtained in this study is for a slightly thinner plate than in *Royden* [1988]. A comparison of the values obtained for the end loads is therefore not very meaningful, even if these had been measured at the same position along the flexing plate in both studies. The visual fit for these two sections is quite similar.

3.5.3 Lateral migration of slab detachment

Remarkably, the three northernmost sections (D, 1 and C) can be modelled quite well, both with an elastic and a continental rheology, while the sections to the south (2, B, 3 and A) pose more difficulties. This may be caused by differences in the time at which slab detachment occurred in relation to the time at which the horizon that at present forms the base of the foredeep was deposited. Independent evidence in support of lateral migration of slab detachment below the Italian region, is the fact that the predicted lateral component in the migration of the deepest part of the foreland basin, the depocentre, has been found from stratigraphic analyses [*Van der Meulen et al.,* 1998]. From Late Miocene to Pleistocene the depocentre shifted from north to south Italy. If this depocentre shift is accepted as the surface effect of a migrating slab detachment, it follows that for sections in the north the base of the Plio-Pleistocene foredeep was deposited after slab detachment (and rebound), while for sections in the south this same horizon was deposited before detachment. Consequently, the base of Pliocene level on these southern sections experienced the effects of slab detachment: increased subsidence followed by rebound. These sections are most difficult to explain with the purely flexural model used in this study. The base of Pliocene level appears more distorted, an indication that these regions experienced more, post-base Pliocene, structural activity. This might be related to effects of slab detachment.

If it is accepted that slab detachment had already occurred in the north before the horizon that at present forms the base of the Plio-Pleistocene foreland basin was deposited, the question arises why this horizon at present lies as deep as 6-8 km. An explanation in the form of an increase in slab pull with time is in contradiction with the postulated timing of the slab detachment. A different explanation is that the outward migration of the trench system since the early Pliocene has caused the observed deep location of the horizon. We found that for an outward migration of approximately 60 km [*Boccaletti et al.,* 1990b], an initially horizontal sediment level can be forced to the observed depths. The eastward migration of the Apennine thrust fronts and the foreland basin increases from north to south [*Bally et al.,* 1986; *Boccaletti et al.,* 1990a]. However, since the base of the Plio-Pleistocene foredeep is slightly younger towards the south (mid E-Pliocene for sections 3 and A), the amount of migration that the base of the foredeep experienced is approximately equal from north to south. It is uncertain what drives the observed eastward migration if the subducted plate in north Italy is detached and the remaining short plate is continental. It is possible that the roll-back in the north is related to the roll-back in south Italy, as suggested by *Wortel and Spakman* [1992] and indicated by numerical modelling by *Negredo et al.* [1997].

3.6 Conclusions

On the basis of the hypothesis of lateral migration of slab detachment [*Wortel and Spakman,* 1992] variations in loads are expected along strike of the Apennine mountains. From the results of modelling with an elastic plate no conclusions related to the pattern of the loads along strike of the Apennines can, however, be drawn. This is due to two different causes. First, for three sections (1, C and D) a trade-off relation between elastic thickness and the deep load exists. The inclusion of gravity data in the modelling process does not make an effective discrimination between the different models possible. This contrasts with the findings of *Royden* [1988]. She, however, employed an hypothetical slab end, beyond which slab material does not contribute to gravitational anomalies. We do not consider this approach in agreement with the presence of several hundreds kilometres of subducted lithosphere [*Spakman,* 1990; *Spakman et al.,* 1993; *Amato et al.,* 1993]. Second, for the sections with a sharp high in the deflection data (2, 3 and B), a more or less reasonable fit could only be obtained for very thin plates. A small elastic plate thickness is, however, not reasonable for the continental Adriatic lithosphere.

The results of modelling with a continental rheology also did not allow a comparison of the values of loads between the sections, due to the large difference in the quality of the fit to the data between the different sections. A good fit was obtained for those sections (1, C and D) for which a good fit could also be obtained for different elastic thicknesses in the modelling with an elastic plate. It especially proved difficult to obtain a reasonable fit to the deflection data for the profiles with a sharp high (2, 3 and B), due to the stiff flexural behaviour of the continental plate model.

The sharp highs in the data for sections 2 and B, which posed difficulties in the modelling with both an elastic and a continental rheology, are most probably not (only) caused by flexure, but likely are a consequence of thrust activity, which is not included in the flex-

ural models. The base of Pliocene level appears more distorted on the southern, than on the northern sections.

Along strike variations in vertical loads could not be resolved from the Plio-Pleistocene foreland basin of the Apennines by modelling deflection and gravity data in two-dimensional sections. We conclude, therefore, that the hypothesis of lateral migration of slab detachment can neither be shown to be consistent nor inconsistent with the observations. Evidence in support of the hypothesis can be found in the lateral component in the depocentre shifts [*van der Meulen et al.,* 1998]. It is likely that the base of Pliocene level in the south experienced the effects of slab detachment. In the north this level was probably deposited after slab detachment occurred, the present (deep) flexure is in this case for the greatest part caused by the outward migration of the trench system.

Chapter 4

A modelling study of vertical surface displacements at convergent plate margins

4.1 Introduction

Observations show that vertical displacements of the Earth's surface near convergent plate margins may reach magnitudes on the order of hundreds of metres to some kilometres [e.g. *Audley-Charles*, 1986; *Lundberg and Dorsey,* 1988; *Westaway,* 1993; *Doglioni,* 1993]. These displacements may be caused by various processes which are related to plate convergence. For example, initiation of subduction may induce subsidence of the overriding plate on the order of a few kilometres [*Gurnis*, 1992], while termination of subduction will probably lead to uplift [*Chatelain et al.*, 1992; *Westaway*, 1993]. In this study, we concentrate on vertical displacements during the phase of ongoing subduction between the first (initiation) and final (termination) stages of a subduction zone system. The aim of our study is to quantify vertical surface displacements near convergent plate margins resulting from variations in a subduction zone system on a time scale of a few million years. It is not our purpose to reproduce the characteristics of a specific subduction zone, but to predict which observable effects may be expected from imposed variations in a subduction zone system. Such variations are more likely rule than exception. For example, with time there will be changes in age of the subducting lithosphere, in velocities of the lithospheric plates due to larger scale plate reorganisations and in mantle flow patterns. We study the effect of variations in the subduction zone system on the flexural behaviour of the lithospheric plates involved on a regional scale. To this purpose we use a two-dimensional elastic model. We present a method for modelling subduction zone dynamics on a time scale of a few million years with a lithosphere model in which the asthenosphere is not explicitly included.

[1]This chapter has been submitted for publication to *Geophysical Journal International*

The lithospheric plates with an effective elastic thickness adequately simulate the surface deflection behaviour at a subduction zone of lithosphere with a more appropriate rheology [e.g. *Watts and Talwani,* 1974; *Caldwell et al.*, 1976]. We examine the effects of variations in buoyancy of the subducting plate, velocity of the surface plates, friction along the interplate contact and slab retrograde motion. Processes like underplating, magmatism, erosion, sedimentation or thrusting are not included in our analysis.

Our choice for a numerical elastic model to study subduction zone dynamics is motivated by a number of considerations. First, in comparison with analogue models, numerical experiments have a larger freedom in choice of material parameters, while stress and topography can be determined at all stages of the experiment. Second, the bending behaviour of a subducting plate at the trench may well be approximated by an elastic flexural process in our view. Therefore, we incorporate elasticity in our lithospheric rheology. We recognise that bending will be accompanied by inelastic deformation [*Chapple and Forsyth,* 1979; *Conrad and Hager,* 1999]. Third, in purely viscous models subducting slabs tend to steepen with time and a non-vertical slab may be obtained by introducing additional factors as trench migration or horizontal mantle flow [*Christensen,* 1996; *Becker et al.*, 1999]. In (visco)elastic models shallow slab dip angles result without the need to invoke these factors [*Hassani et al.*, 1997]. Finally, the development of surface topography is an integral part of the method in mechanical models. In viscous models [e.g. *Zhong and Gurnis,* 1994; *Gurnis et al.*, 1996] dynamic topography is derived from the normal stress at the surface of the model. In the following paragraphs we discuss viscoelastic models of subduction zone dynamics. Our limitation to this category of models is motivated partly by the importance we attribute to elasticity in subduction models and partly by the work of *Gurnis et al.* [1996] who show that topography near a convergent plate margin is overall remarkably similar for viscous and viscoelastic models. The viscoelastic models have a wider and deeper trench, and a more prominent forebulge.

Whittaker et al. [1992] examined intraplate stresses and plate boundary forces resulting from the density difference between the subducting plate and the surrounding mantle (slab pull) with a two-dimensional elastic-viscoelastic model. They show that the interplate contact needs to be (partly) unlocked in order to enable back-arc stretching. Extending on this approach, *Giunchi et al.* [1996] matched horizontal and vertical surface velocities for the southern Tyrrhenian Sea (Italy) with a viscoelastic model. *Negredo et al.* [1997] show in a three-dimensional modelling study that the combination of density-driven subduction and along strike convergence controls the arcuate shape of the subduction zone around the eastern side of Italy. The time scale of these simulations is on the order of 200 kyr. The modelling approach used in these studies has its limitations in case that surface displacements are examined which are due to forcings on geological time scale, like subduction. This is related to the choice of the initial model and model time scale. In the initial model stresses due to the previous geological history are not included. These should be incorporated by appropriate initialisation and/or integration over sufficiently long time (order Myr). In the above examples, the model evolution starts with an already bent subducted lithosphere in which flexural bending stresses are not taken into account. In reality, subducting lithosphere bends at the trench and unbends at depth. To achieve unbending on longer time scales, bending stresses have to be included in (visco)elastic models.

Ongoing subduction has been modelled with a viscoelastic rheology by *Gurnis et al.* [1996] who examine trench topography starting from a pre-defined subduction geometry and integrating the model for 5 Myr. They find that topography depends on lithospheric viscosity, subduction fault dip angle and slab dip angle. *Hassani et al.* [1997] simulate subduction initiation, continued subduction and subduction zone roll-back with a (visco)elastic model. Their results show that both stress in the plates and surface topography depend on the density contrast between the subducting plate and the mantle and on the coefficient of friction along the subduction fault. Their results are in good agreement with the analogue models of *Shemenda* [1993]. Our modelling approach is similar to the method of *Hassani et al.* [1997]. The main differences lie a) in the initiation phase, since we do not model subduction initiation, but initialise our model trough bending of a horizontal plate, and b) in the subduction forcing in which we group together the effects of slab pull and viscous and hydrostatic stresses exerted on the slab by the asthenosphere.

We present results of modelling of subduction zone roll-back caused by two different driving mechanisms: outward trench migration is caused by sinking of the negatively buoyant subducting plate [*Elsasser*, 1971] or it is forced by the motion of the overriding plate [*Cross and Pilger*, 1982].

4.2 Modelling method

4.2.1 Equations and rheology

We use a two-dimensional numerical model to study the effects of subduction on surface displacements near the convergent plate margin. The model is on the scale of the whole lithosphere. The mechanical evolution of lithosphere on geological time scales is governed by the equilibrium equations:

$$\nabla \cdot \sigma + \rho g = 0 \quad + \text{ boundary conditions} \tag{4.1}$$

where σ is the stress tensor, ρ mass density and g gravitational acceleration. In our models, the body force term (ρg) is replaced by boundary conditions on the model sides. These are discussed below. The implication of this approach is that the effects of lateral density variations inside the model plates are neglected. Equation 4.1 is solved using the finite-element code TECTON, which was originally written by *Melosh and Raefsky* [1980] [see also *Melosh and Raefsky*, 1983; *Melosh and Williams*, 1989]. We account for the effects of large deformations by using the formulation of *Wallace and Melosh* [1994]. We assume that no deformation occurs perpendicular to the plane of our model and, therefore, the plane strain approximation is adopted. The convention is used that compression is negative and tension positive.

In our simulations we use lithospheric plates with an effective elastic thickness. These result in a good approximation to the surface deflection behaviour at a subduction zone of lithosphere with a more appropriate rheology [e.g. *Watts and Talwani*, 1974; *Caldwell et al.*, 1976]. Therefore, the elastic plate approximation is warranted in our study in which we quantify surface deflections induced by changes in a subduction zone system. We use one

fixed value for the effective elastic thickness of the lithosphere. In case the evolution of a specific geological region were simulated this value would have to be varied or constrained by independent information, e.g. thermal and age data. In some of our models, we introduce a local zone of low viscosity in the overriding plate to simulate a zone of weakness. This part of the model has a Newtonian viscoelastic rheology.

4.2.2 Geometry

Our model consists of a subducting and an overriding lithospheric plate (Fig. 4.1). The asthenosphere is not included in the model domain for reasons of numerical efficiency. In lithosphere models which do incorporate the asthenosphere, lateral and bottom boundary conditions on the model domain sides have a large influence on the response of the lithosphere, especially for models with relatively small spatial dimensions. This is caused by the fact that viscous asthenosphere is incompressible on geological time scales. Rather than building a model with spatial dimensions that are (at least) an order of magnitude larger than the dimensions we are interested in, we choose to represent the effects of the asthenosphere on the lithosphere through appropriate boundary conditions. These are discussed below. Our model slab is relatively short and initially extends to 90 km depth (Fig. 4.1). Below we discuss the boundary conditions acting on the model slab end which represent that in reality the slab extends deeper into the mantle ('Boundary conditions' paragraph).

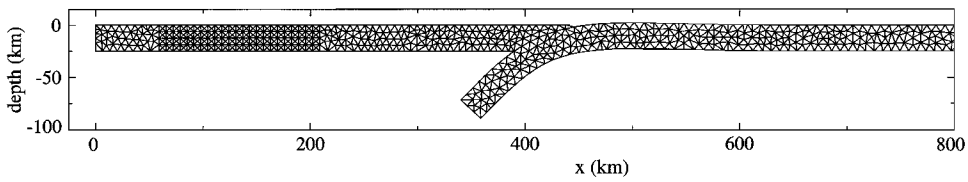

Figure 4.1: Finite element grid. The subducting plate initially extends to 1226 km and is not completely shown here. Discretisation in the subducting plate is slightly coarser towards the right edge.

In our model, the contact between the subducting and the overriding plate is a slippery fault [*Melosh and Williams*, 1989], which can deform and migrate. We have modified the slippery fault formulation in such a way that the fault slip is locally always parallel to the fault geometry. Initially, the subduction fault is curved and it follows the geometry of the subducting plate. The coefficient of friction on the fault is defined as $\mu = |\tau|/|\sigma_n|$ (where τ is shear stress and σ_n normal stress on the plate contact including gravitational pressure).

The model domain has been divided into 1557 isoparametric triangles built from 959 nodes (Fig. 4.1). The models are integrated with 1000 year time steps over several millions of years, until a total displacement in the range of 50-150 km is achieved. We have performed convergence tests with a finer mesh (2953 elements) or smaller time step (500 yrs) which confirmed that our results have converged for the chosen time and space discretisations.

4.2.3 Consistent initial geometry and pre-stresses

To avoid the implementation of a subduction initiation phase, our models are started from the geometry of an already bent subducting plate. Since we are interested in subduction on longer time scales this approach requires that bending pre-stresses are incorporated in a manner which is consistent with the initial geometry. These pre-stresses allow for unbending at depth of subducted lithosphere in case of a (partly) elastic rheology. Also, for large deformations the stresses influence the evolution of the model [*Wallace and Melosh*, 1994]. To compute bending stresses which are dynamically consistent with a subduction geometry, we include an initialisation phase in the modelling. A horizontal plate is bent to obtain the geometry of a subducted plate. The plate is flexed by stresses at one plate end while the other end is held fixed. We have verified that this approach leads to a geometry which agrees with existing subduction zone geometries as defined by Benioff zones. The overriding lithosphere is subsequently added to the subducted plate to complete our initial model (Figs. 4.1 and 4.2).

We remesh the grid after the initialisation phase to avoid too large deformations. All boundary conditions, rheological parameters and stresses are mapped onto the new grid and the calculations are restarted. We are aware that remeshing may introduce inaccuracies in the calculations. To minimise these, we enforce equilibrium between nodal forces and element stresses by calculating the initial nodal forces on the new grid from the stresses.

A solution of the equilibrium equations (4.1) gives the model geometry and stresses which balance the imposed boundary conditions. As a result, a boundary condition, for example a force, which acts on the model at some time instant, is represented in the model stresses and geometry from that time onward. Therefore, special care has to be taken when boundary conditions are changed at a later time. The old boundary condition has to be taken out of the system of equations and then replaced with the new condition. This also applies to the bending pre-stresses in the initial model after the remeshing step. The relaxation of these initial stresses has to be defined explicitly. We do this by allowing the initial bending stresses to relax with displacements along dip of the subducting slab.

4.2.4 Boundary conditions

Horizontal plates

Viewed on a large scale, plate motions are for a great part driven by slab pull and ridge push forces. These forces are counteracted by resistive forces, like transform resistance and basal drag. With our model we represent only part of this system. We include the net effect of forces outside the model domain through velocity boundary conditions at the left and right sides of the surface plates (Fig. 4.2c), since these are observationally constrained. Combinations of different magnitudes and orientations of the velocity boundary conditions allow us to simulate various plate tectonic settings.

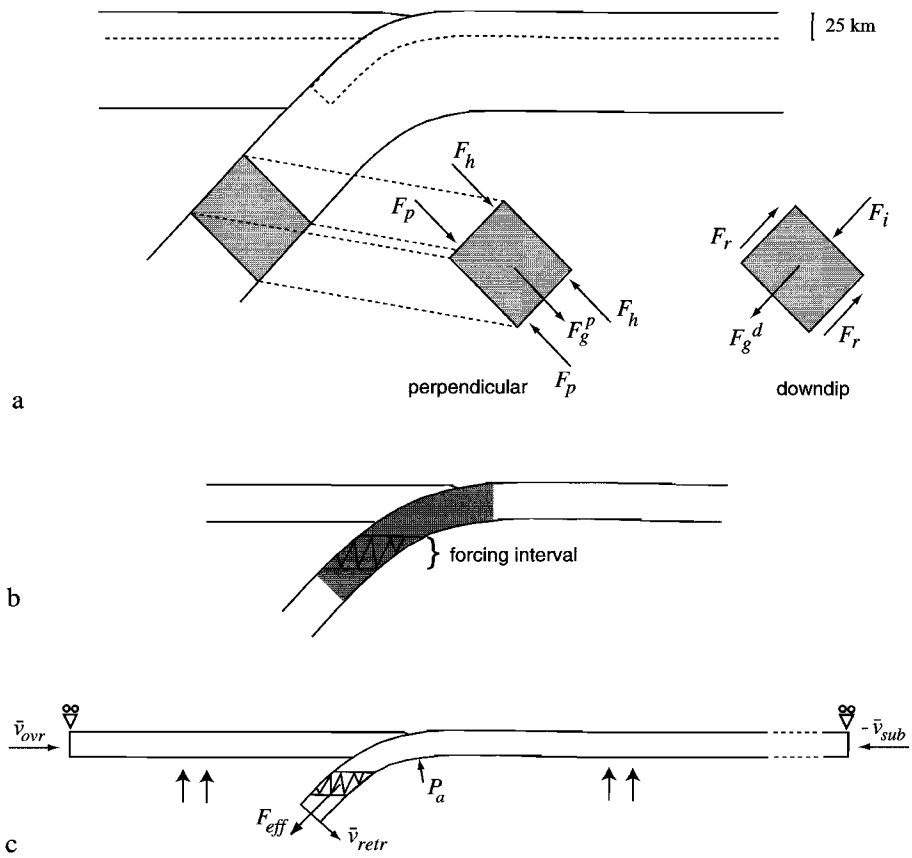

Figure 4.2: a) The behaviour of the thick lithosphere of the overriding and the subducting plates (drawn line) is in the model approximated by using plates with an effective elastic thickness (dotted line). Forces acting on a fully subducted segment of the subducting plate are indicated: F_g slab pull, F_h hydrostatic restoring force, F_p force due to pressure differences, F_i ridge push, and F_r resistive force. b) Shaded area indicates the depth interval in which a segment of the subducting plate accelerates, the zigzags denote the forcing interval in which an effective pull force is applied in the numerical model. c) Schematic illustration of the model and general boundary conditions. The subducting plate experiences an effective pull force (F_{eff}) oriented down the dip of the slab. Subduction zone roll-back is simulated through a slab normal velocity ($\bar{v}_{retr}$) applied at the model slab end. The right hand side boundary of the subducting plate and the left hand side of the overriding plate are held fixed laterally or move with a prescribed velocity. The orientation and magnitudes of the velocities can change. The rollers at the top left and right corners indicate that the corners are not allowed to move vertically. The black-arrows indicate the hydrostatic pressure which is exerted by the asthenosphere on the lithospheric plates. See text for definition of P_a.

Viscous asthenosphere

We have chosen to include the asthenosphere in our models through boundary conditions which simulate its interaction with the lithospheric plates. In our view, the main contributions to this interaction are hydrostatic pressure, dynamic pressures (e.g. corner flow) and (viscous) resistance.

At the viscosity of the asthenosphere (on the order of 10^{21} Pa s) the relaxation time of a viscoelastic (Maxwell) body is on the order of a few thousand years. This means that the asthenosphere can be considered to be in hydrostatic equilibrium on geological time scales. The pressure increases linearly with depth at a rate $\Delta p = \rho_a g \Delta z$, where p is pressure, ρ_a density of the asthenosphere and z depth. In this expression we neglect the compressibility of the asthenospheric material which would lead to only a small difference in the pressures in the shallow upper mantle, e.g. 3% at 200 km depth. The hydrostatic pressure effectively acts as a restoring pressure which opposes vertical displacement of lithospheric plates at the Earth's surface. Once material is fully subducted, the hydrostatic pressure acts on both sides of the subducting plate. If it is assumed that density does not change with depth (which is a reasonable approximation for the depths of 150-200 km in our models [e.g. PREM, *Dziewonski and Anderson*, 1981]), a vertical displacement leads to the same pressure increments on the upper and lower sides of the plate, when viewed in cross section. For the subducting plate, therefore, we have taken these forces out of the system of equations. This applies to the part of the subducting plate between the location of model parameter P_a (Fig. 4.2c) and the model slab end. In all simulations except two (models 5 and 10) the location of P_a is defined by the (perpendicular downward projection of the) point of contact of the overriding plate with the subducting plate at the surface. The location of P_a is, therefore, defined dynamically and will change during model evolution in case of trench migration. Note that it is assumed that the pressure exerted by the overriding plate on the subducting plate is hydrostatic. The balance in hydrostatic pressures near the contact with the overriding plate may be affected by dynamic processes in the mantle, changes in density of the overriding plate and changes in the amount of material lying on the subducting plate near the trench. These effects may be incorporated through variation of the location of P_a. A larger accretionary wedge, for example, will exert a downward pressure over a larger area and shift P_a oceanward.

During subduction, motions of the lithospheric plates induce flow of mantle material on both sides of the subducting lithosphere. This corner flow exerts a lifting pressure on the subducting slab, which may contribute to maintaining a non-vertical slab dip. It has been shown [*Stevenson and Turner*, 1977; *Tovish et al.*, 1978; *Dvorkin et al.*, 1993] that the moments due to corner flow and the negative buoyancy of the slab can be in equilibrium. In our models, the orientation of the subducted slab is determined by the balance between forces which act in a direction normal to the slab (Fig. 4.2a). In our models of steady non-migrating subduction, we assume that the slab normal component of slab pull and the dynamic and hydrostatic pressures balance each other. We assume that retrograde motion of the subducting plate can occur when the forces perpendicular to the slab no longer cancel each other. This can take place, for example, in the case of a narrow subduction zone (narrow in the along trench direction), a short subducting slab or a discontinuous slab, when

mantle material can more easily flow around the subducting plate [*Dvorkin et al.*, 1993]. In this way the building up of dynamic pressures is reduced and retrograde motion of the slab is facilitated.

There is no seismological evidence of thickening or thinning of subducted slabs during their descent in the shallow upper mantle (disregarding slab detachment). The inference is that slabs do not accelerate or slow down following subduction. As it moves in the mantle a subducting plate will experience a viscous resistance. This frictional drag exerted by the mantle on the sides and leading edge of the subducting lithosphere acts to reduce the effect of the along dip component of slab pull. In our model, we assume that once the slab has straightened out, the along dip component of slab pull is balanced by viscous resistive forces and internal stresses (due to the plate segment being attached to the rest of the subducting plate). The slab parallel velocity remains constant with time, i.e. the slab has reached its terminal velocity [e.g. *Marton et al.*, 1999].

Subduction forcing

The stress solution of the equilibrium equations (4.1) represents mechanical equilibrium between model geometry and forces acting in and on the model. Imposing a force on a constrained elastic body results in a solution of stress and geometry which does not change with time. However, during subduction, the boundary conditions acting on a specific lithosphere segment are a function of the position of the segment relative to the trench. This means that the forces working on a piece of subducting lithosphere are time dependent if the convergence velocity is non-zero. Far away from the trench, no net vertical force acts on the subducting plate. Here, the bathymetry has balanced at a level where the lithosphere is supported by the mantle below it. We assume that for the deeper, fully subducted part of the subducting plate all forces on the slab (e.g. slab pull, viscous resistance and internal stresses) balance each other in case of non-migrating subduction. In the zone between the plate at the Earth's surface and the fully subducted slab, the support changes from being dependent on vertical position to depending on subduction velocity.

During subduction a segment of the subducting plate accelerates from a zero vertical velocity before the trench to the vertical (component of) subduction velocity at depth below the overriding plate. In this depth interval, therefore, an effective downward force, F_{eff}, acts on the plate segment, i.e. the forces on the slab do not balance one another. The depth interval in which the effective pull force acts on the subducting plate is determined by the location of the trench and the depth where the terminal velocity has been reached (shaded area in Fig. 4.2b). We assume that no forces act on the slab below the force interval.

The effective pull force incorporates the effects of the density difference between the slab and its surroundings, resistive forces (e.g. friction along the subduction fault) and dynamic pressures due to flow in the asthenosphere. We realise that by parameterising these driving and resistive forces with a net pull force we may ignore important details of, for example, asthenospheric flow. The benefit of our approach is that we can efficiently simulate subduction of elastic plates. We determine the magnitude of F_{eff} for our numerical model by measuring the force on the slab for a velocity driven subduction model. For this particular case subduction is maintained through a velocity at the surface (v_{sub}) and an along dip

velocity at the model slab end of the same magnitude. Steady-state subduction (i.e. slab dip and velocity remain the same with time) results for a model in which the measured effective pull force, F^0_{eff}, and v_{sub} are applied. In our models, F_{eff} is acquired over a depth interval between 60 and 80 km. This forcing interval (Fig. 4.2b) lies below the region of largest bending of the subducting plate and above the initial model slab end. We have verified that a larger interval or a vertical shift within the limits imposed by the size of the initial model does not affect surface displacements.

When the slab normal component of slab pull and dynamic mantle pressures are not completely in balance, the subducting plate may show a tendency towards roll-back. We simulate the effect of the out-of-balance pressures with a velocity boundary condition (v_{retr}) applied at the model slab end in the slab normal direction (Fig. 4.2c). This boundary condition takes into account the effect of both the slab normal pressure difference along the model slab as well as along the deeper part of the slab which is not physically included in the model. We expect that the dip angle of long slabs can not easily change. Therefore, to simulate long slabs we locally fix the dip angle of the model slab end. In case of a short slab or a slab of limited along-strike extent, mantle material may more easily flow around the slab end, thereby reducing dynamic pressures differences and allowing for a change in dip angle. In these cases, therefore, the dip angle of the slab is free to adjust dynamically.

4.3 Modelling analysis

4.3.1 Model 1

For comparison purposes, we first simulate a relatively simple subduction situation with a non-migrating trench position. The subducting slab experiences an effective pull, F^0_{eff}, oriented along dip of the slab. The velocity of the right edge of the subducting plate at the surface is -4 cm/yr (v_{sub} in Fig. 4.2). The - sign indicates velocity directed towards the left. The overall rate of convergence between both side boundaries of the model is 4 cm/yr. Values of modelling parameters which remain the same for all models are shown in Table 4.1. Fig. 4.3 shows the results of model 1 (see also Table 4.2). The vertical displacement and horizontal velocity (averaged over 0.1 Myr) of the surface are shown at the top of the figure. The displacement is given relative to the surface of the initial model. During the evolution of the model the dip angle of the subducting plate remains near 45°, although it is allowed to change dynamically. The margin of the overriding plate is deflected downward. The

parameter	value
Effective plate thickness	25 km
Young's modulus	5×10^{10} Pa
Poisson's ratio	0.25
Gravitational acceleration	9.80 m s^{-2}
Viscosity weak zone	5×10^{21} Pa s

Table 4.1: Modelling parameters

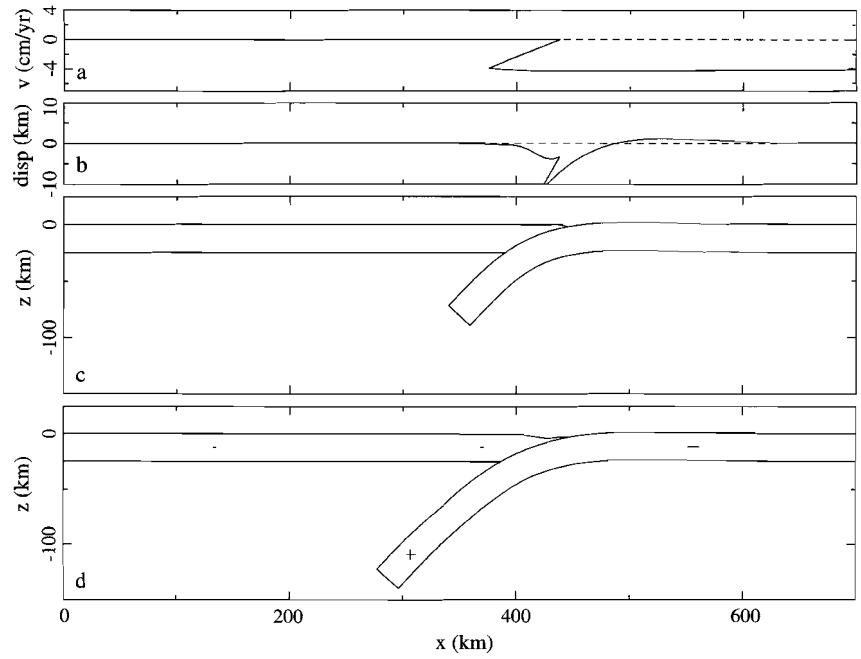

Figure 4.3: Model 1 (see also Table 4.2). Subduction of a negatively buoyant plate pushed at its right hand side with -4 cm/yr. In this and subsequent figures the subducting plate extends further to the right than shown here (initial model ends at 1226 km). Results are shown after 2 Myr. a) Horizontal surface velocity averaged over last 0.1 Myr (positive (negative) velocity indicates motion to the right (left)), b) total vertical surface displacement (relative to surface of initial model), c) initial model, d) model after 2 Myr, +/- signs indicate inplane tension/compression, respectively.

maximum subsidence is nearly 4 km after 2 Myr. The subducting slab is in tension due to the exerted pull. The surface plates are both in compression.

The evolution of vertical surface displacement is shown in Fig. 4.4. With time the overriding plate margin is deflected downward, until it obtains a maximum subsidence. The height of the flexural bulge of the subducting plate also achieves a maximum after approximately 2 Myr, after which it decreases slightly. Overall, there are no large changes in surface topography after 2 Myr (or 80 km of convergence). At this time the effects of initial conditions have disappeared and an equilibrium topography is reached. In comparing surface displacements between different models we will use these equilibrium results.

The observation that vertical surface displacement and slab dip do not change much with time indicates that the velocity $\overline{v}_{sub}$ of the subducting plate at the surface and F_{eff} are in equilibrium with each other for the elastic rheology which is used. In model 1 the magnitude of the subduction velocity was 4 cm/yr. For higher (lower) velocities equilibrium is maintained, since segments of the subducting plate pass the forcing interval at higher (lower) velocity. This implies that the total pull force experienced by the whole slab beneath

model	$\times F_{eff}^{0}$ [1]	v_{retr} (cm/yr)	dip [2]	v_{sub} (cm/yr)	v_{ovr} (cm/yr)	v_{conv} [3] (cm/yr)	μ	P_a shift (km)	weak zone	trench [4]	Fig.
1	1	0	free	-4	0	4	0	0	n	n	4.3, 4.4
2	2.0	0	free	-4	0	4	0	0	n	n	4.5
3	0.5	0	free	-4	0	4	0	0	n	n	4.5
4	0	0	free	-4	0	4	0	0	n	n	4.5
5	0	0	free	-4	0	4	0	40	n	n	4.5
6	1	0	free	-4	2	6	0	0	n	r	4.6
7	1	0	free	-4	-2	2	0	0	n	f	-
8	1	2	fix	-4	0	4+	0	0	y	r	4.7
9	1	2	free	-4	0	4+	0	0	y	r	4.7
10	1	2	fix	-4	0	4+	0	-40	y	r	4.7
11	1	2	fix	0	0	0+	0	0	y	r	4.8, 4.9
12	1	2	free	0	0	0+	0	0	y	r	-
13	1	0	free	-4	0	4	0.1	0	n	n	-
14	1	2	free	-4	0	4+	0.05	0	y	r	-

[1] Oriented along dip of the slab.

[2] Dip angle of model slab end is either free or held fixed.

[3] Measured between the model left and right side boundaries. In case of roll-back with back-arc extension the convergence rate locally across the plate boundary will be higher, this is indicated with a +.

[4] n: non-migrating, r: retreat, f: forward.

Table 4.2: Classification of models.

the forcing interval is linearly related to v_{sub}. For the same amount of plate convergence surface topography is the same. Therefore, we will not vary the magnitude of v_{sub} and use 4 cm/yr in the following models.

The surface topography of our reference model is similar to results of *Hassani et al.* [1997] (their Fig. 4). It differs from the results of *Gurnis et al.* [1996] in that we do not find an uplift on the order of 1 to 2 km of the edge of the overriding plate margin, next to the subduction fault. We speculate that this localised difference may be caused by a difference in shape of the subduction fault: *Gurnis et al.* [1996] use a straight fault, while ours is curved.

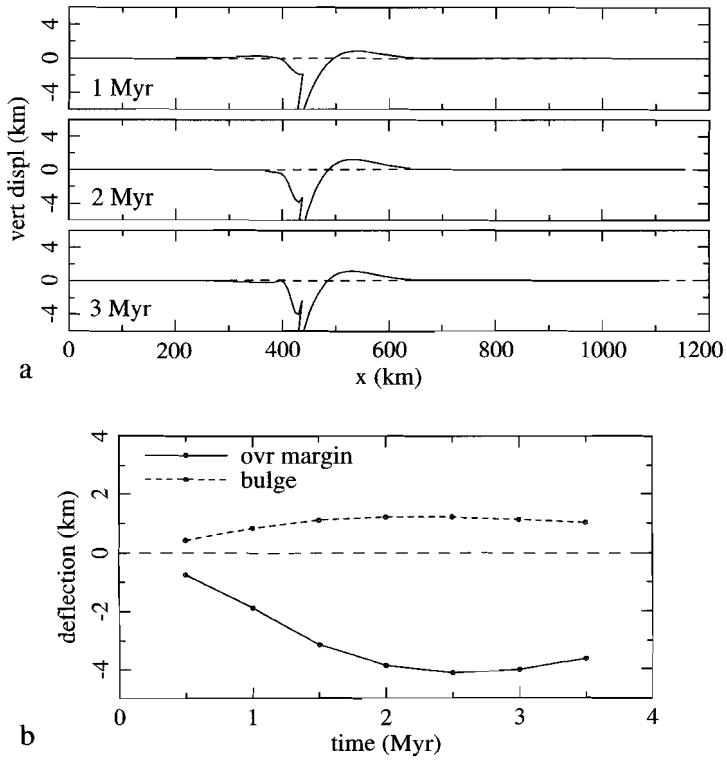

Figure 4.4: Evolution of vertical surface displacement of model 1 (Fig. 4.3) through time. a) Vertical surface displacement relative to surface of initial model at three stages during model evolution (after 1, 2 and 3 Myr). Vertical scale is 16 times exaggerated. b) Maximum downward deflection of overriding plate margin and maximum upward deflection of subducting plate (bulge) versus time. Small circles denote times for which values have been calculated.

In the next paragraphs we report the effects of parameter variations with respect to model 1. Changes in effective driving force (F_{eff}), velocity of the overriding plate (v_{ovr}), slab normal pressures and friction along the subduction fault are examined.

4.3.2 Variation in slab buoyancy

We expect that changes in buoyancy of the subducting plate will affect vertical surface displacements significantly. We study these effects by varying the effective pull F_{eff}. Variations in F_{eff} may result from changes in the density difference between slab and mantle or from changes in viscous resistance to subduction. Our parameterised forcing approach does not allow us to distinguish the two cases. This is in fact analogous to using the buoyancy number of *Houseman and Gubbins* [1997] in quantifying slab buoyancy. This buoyancy number includes the effects of gravitational driving force and viscous resistance. In Fig. 4.5 the vertical surface displacement is shown for 2 $\times F^0_{eff}$ (model 2), F^0_{eff} (model 1), 0.5 $\times F^0_{eff}$ (model 3) and $F_{eff} = 0$ (models 4 and 5). All profiles are for 80 km of plate convergence. There is a clear trend of increasing uplift of the overriding plate margin with decreasing F_{eff}. A magnitude of approximately 2 km is reached for model 3 (0.5 $\times F^0_{eff}$). An increase in F_{eff} deepens the deflection of the margin of the overriding plate (to -8 km in Fig. 4.5a, model 2). The development of vertical surface displacements is sensitive to dynamic processes in the mantle. We parameterise the effects of mantle dynamics through F_{eff} and the location of P_a (which defines the top of the depth interval in which pressures across the slab are in balance, Fig. 4.2). Pressure differences in the mantle or a change in density of the overriding plate, for example, may change the location of P_a. A shift in the oceanward direction in P_a of 40 km lowers the uplift of the overriding plate margin of model 4 with nearly 4.5 km (model 5). In the following simulations P_a is kept at the same location as in model 1, so resulting surface displacements can be compared between the models.

4.3.3 Trench migration

Trench retreat and advance forced by the overriding plate

The location of a subduction zone trench is not necessarily stationary as is evidenced by observed migrations of trenches in the direction perpendicular to their strike. In most cases the trench migrates in the direction opposite to the motion of the subducting plate. We first examine the surface effects of trench retreat (e.g. South America [*Chase,* 1978; *Gripp and Gordon*, 1990]) and advance (e.g. Makran, Himalayas [*Chase*, 1978; *Royden*, 1993]) forced by the motion of the overriding plate. The trench displacements are examined in an absolute reference frame. To simulate forced trench retreat a velocity v_{ovr} of 2 cm/yr is imposed at the left side of the model. Fig. 4.6 shows that after 80 km of convergence (at 1.35 Ma) the surface displacement for model 6 is the same as for model 1. In fact, the models are very similar, since the convergence obtained by moving both the overriding and subducting side boundaries can equally well be simulated by keeping the overriding plate fixed laterally and moving only the subducting plate. This also applies to the case of trench advance (model 7, not shown).

In models 6 and 7 the subducted slab is free to migrate laterally with respect to the mantle in response to the imposed surface velocities. It may, however, be possible that the slab feels a resistance to lateral migration through the mantle, for example, due to increased

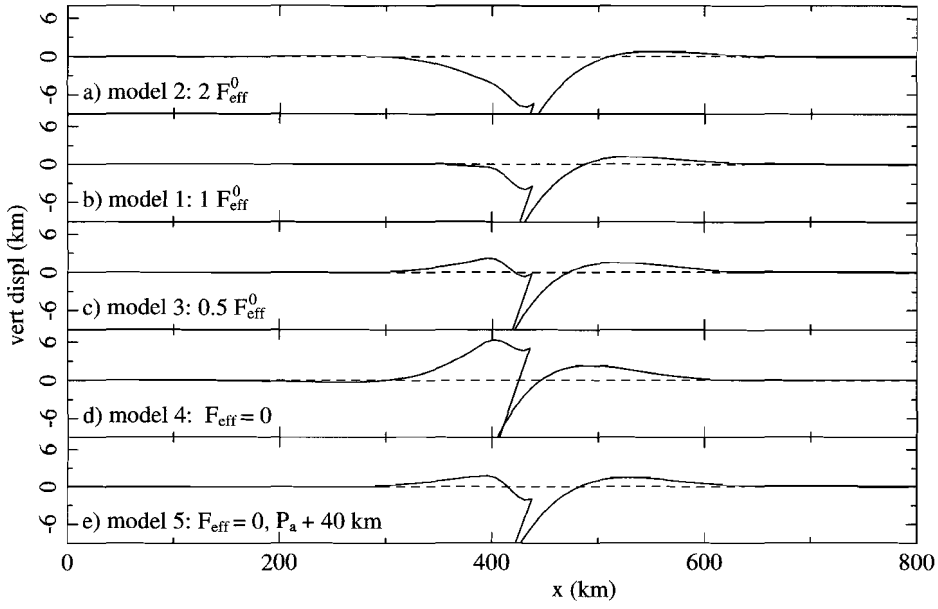

Figure 4.5: Effect of change in effective pull F_{eff} on vertical surface displacements after 80 km of convergence. Displacements are relative to surface of initial model. a) $F_{eff} = 2 \times F^0_{eff}$, b) $F_{eff} = F^0_{eff}$ (equal to Fig. 4.3), c) $F_{eff} = 0.5 \times F^0_{eff}$, d) $F_{eff} = 0$, e) $F_{eff} = 0$ and P_a + 40 km. Vertical scale is 6 times exaggerated.

mantle pressures in the direction of slab translation. Active overriding by a continent may then lead to a low dip angle at shallow depths followed by a steeper slab further down, similar to what is observed along parts of the South American subduction zone [*Barazangi and Isacks*, 1979; *Cahill and Isacks*, 1992]. Model 6b again simulates trench retreat forced by the overriding plate, only in this case it is assumed that the deeper part of the slab can not migrate laterally. Therefore, movement of the model slab end is constrained to the along dip direction. Since retrograde motion of the slab is prevented from relatively shallow depths downward, this can be considered as an end-member situation. Uplift of the overriding plate margin is induced which reaches a maximum magnitude of nearly 1.5 km after 80 km of convergence (Fig. 4.6b). With respect to models 1 and 6, the overriding plate experiences an increase in inplane compression.

Roll-back caused by negative buoyancy of slab

When the slab normal component of slab pull is not completely balanced by dynamic mantle pressures, the subducting plate displays a tendency towards roll-back. Subduction zone roll-back can only occur if the overriding plate allows it. Either the overriding plate must be able to follow the retreat of the subducting plate or it must be able to extend. In the latter case a

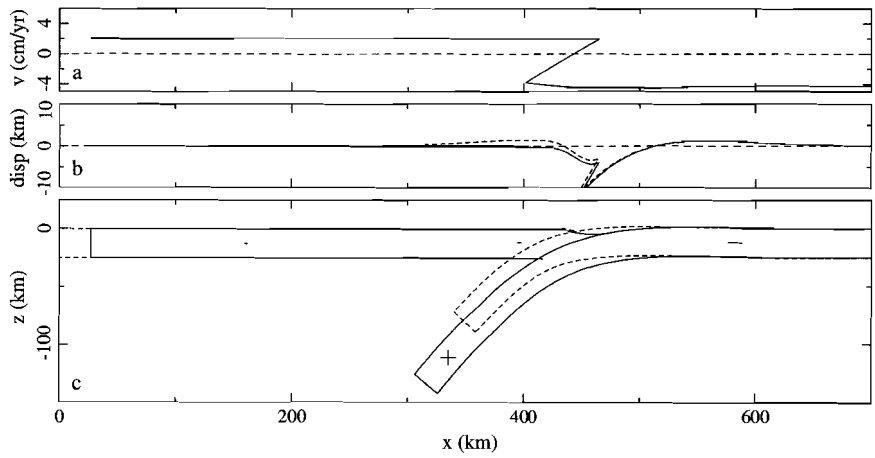

Figure 4.6: Model 6. Subduction zone roll-back forced by an advancing overriding plate. The velocity of the subducting plate is -4 cm/yr, the overriding plate moves with 2 cm/yr. Results are shown after 80 km convergence at 1.35 Ma. a) Horizontal surface velocity averaged over last 0.1 Myr, b) vertical surface displacement, dotted line is displacement for model 6b (see text), c) model configuration, dotted line is outline of initial model, +/- signs indicate inplane tension/compression, respectively.

back-arc basin develops. We allow for subduction zone retreat through the introduction of a 100 km long weak zone with a lower viscosity (5×10^{21} Pa s) in the overriding plate.

Model 8 simulates subduction zone retreat for a long slab. We assume that in this case the deeper part of the subducting slab will impede changes in dip angle. Therefore, we locally fix the dip angle of the model slab end. The magnitude of the slab normal velocity at the model slab end is 2 cm/yr, v_{sub} is -4 cm/yr. After 80 km of convergence, at 0.9 Ma, the trench has retreated with around 34 km. At this time, the subsidence of the overriding plate margin is approximately 9 km at maximum, while in the back-arc area a basin has developed (Fig. 4.7). The maximum subsidence of the overriding plate margin is reduced when the dip angle of the slab is allowed to change (Fig. 4.7). This applies to, for example, a short subducting slab, where dynamic pressure differences across the slab may be reduced by flow of mantle material around the slab end. In the case of model 9 the dip angle of the model slab end increases with around 13° in 1 Myr. The steepening of the slab is accompanied by an increase in the velocity of retreat. Overall, the average velocity of roll-back is lower than for model 8. In 1.35 Myr (80 km of convergence) the trench retreats with 24 km.

Subsidence of the overriding plate margin in models 8 and 9 is rather high (Fig. 4.7). This may be reduced by a change in the pressure-balance parameter P_a. For the case of non-migrating subduction we have shown that an oceanward shift in P_a lowers surface uplift. In a similar manner a shift towards the continent reduces subsidence of the overriding plate margin, as is shown in Fig. 4.7c (model 10). A continent-ward shift may, for example, be caused by a lower density of the overriding plate lithosphere.

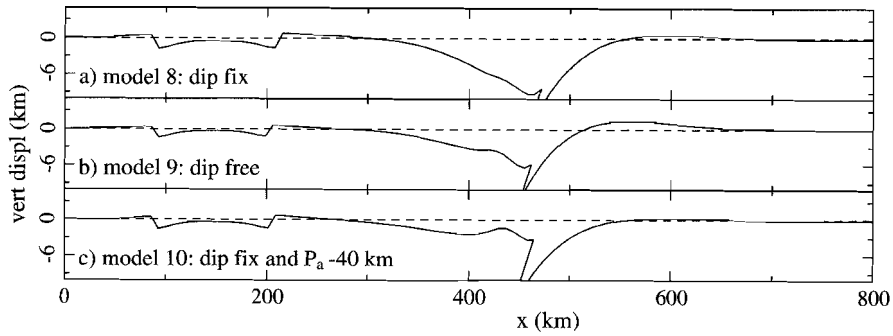

Figure 4.7: Vertical surface displacements for models in which the subducting slab retreats due to its negative buoyancy. Displacements are relative to surface of initial model and measured after 80 km of convergence. The viscosity of the weak zone in the overriding plate is 5×10^{21} Pa s. v_{retr} = 2 cm/yr, v_{sub} = -4 cm/yr. a) Dip of model slab end held fixed ('long slab'), b) dip of model slab end free ('short slab'), c) dip fixed and P_a -40 km. Vertical scale is 6 times exaggerated.

Roll-back in a land-locked basin setting

A land-locked basin [*Le Pichon*, 1982] refers to an oceanic basin trapped within a continental collision zone. In this case subduction of the basin can be achieved through roll-back of the trench and extension of the overriding plate. Model 11 simulates a land-locked basin setting. Both side boundaries of the model are not allowed to move laterally (v_{sub} = v_{ovr} = 0 cm/yr). The slab parallel driving force is again F^0_{eff}, while the slab normal velocity at the model slab end is 2 cm/yr. We assume a long subducting slab, therefore, the dip angle of the model slab end is held fixed. Fig. 4.8 shows the results of model 11 after 2.3 Myr. The amount of trench retreat is 74 km. The average rate of roll-back is, therefore, around 3.2 cm/yr. The velocity of the overriding plate margin depends strongly on the magnitude of the slab normal velocity v_{retr}. For example, for a slab normal velocity of 1 cm/yr the average rate of roll-back is 1.6 cm/yr. The velocity of roll-back is to a lesser extent sensitive to the value for the viscosity of the weak zone. A low value for viscosity facilitates roll-back. In case of a high viscosity the subducting plate is held back by the strong overriding lithosphere. In the latter situation the overriding plate margin will deepen as it is partly dragged along by the sinking subducting plate. We find that the surface topography after 80 km of convergence is the same for models in which the values for the viscosity of the weak zone and v_{retr} are inversely linearly related. This is due to the Maxwell viscoelastic behaviour of the weak zone. If the dip angle of the subducting plate is allowed to change during roll-back the slab steepens with 16° in 4 Myr (model 12). The average velocity of roll-back is lower in comparison with model 11 and amounts 2.1 cm/yr after 80 km of convergence at 3.6 Ma. The maximum subsidence of the overriding plate margin is reduced with around 2 km.

Extension in the overriding plate localises in the weak zone. A small amount of flank uplift and deepening of the basin adjacent to the flanks can be observed (Figs. 4.7 and 4.8). The uplift/deepening pair is probably caused by the variation in plate thickness across the

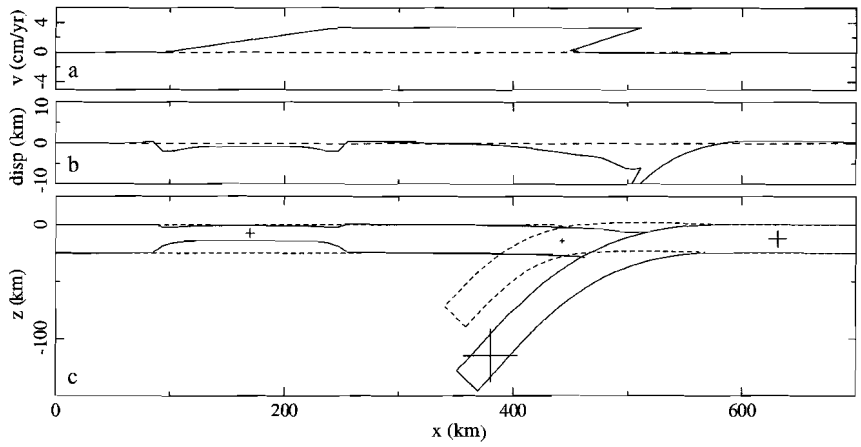

Figure 4.8: Model 11. Subduction zone roll-back in a land-locked basin setting. The side boundaries of the surface plates are fixed laterally. Viscosity of the weak zone in the overriding plate is 5×10^{21} Pa s. v_{retr} = 2 cm/yr. Results are shown after 80 km convergence at 2.3 Ma. Panels as in Fig. 4.6.

boundary of the basin. This results in a change in depth of the horizontal force, creating a moment which bends the plate [*Morgan et al.*, 1987]. Tension in the overriding plate is shown in Fig. 4.9. The small deviation of tension from the horizontal near the boundaries of the weak zone is in agreement with the postulated bending moments across these boundaries.

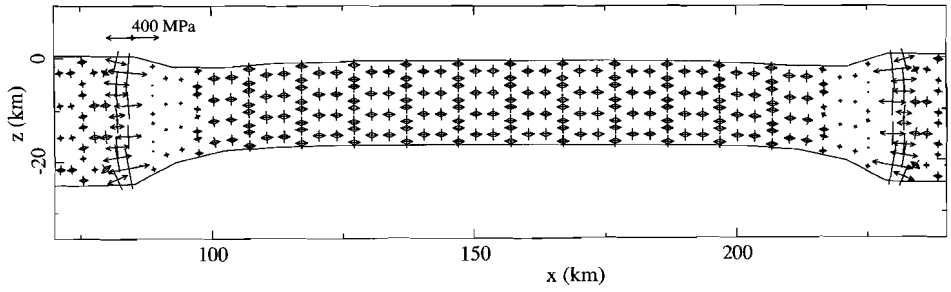

Figure 4.9: Deviatoric stresses in the back-arc region for subduction zone roll-back of model 11 (Fig. 4.8) at 1.5 Ma.

4.3.4 Friction

Friction along the interplate contact increases the resistance to subduction. In model 13 an average coefficient of friction of $\mu = 0.1$ is imposed on the subduction fault (model is not

shown separately). In all other aspects the model is the same as model 1. The friction leads to a deepening of the overriding plate margin. Relative to model 1 the extra subsidence is more than 1 km at 2 Ma. This result is in qualitative agreement with the results of *Cattin et al.* [1997] who report a deepening of the trench with higher values for the friction coefficient. *Hassani et al.* [1997] show that stresses in the overriding plate reverse from tension to compression with increasing coefficient of friction. In their model slab pull acts vertically, while slab dip increases during model evolution. Since in model 1 F_{eff} is directed along dip of the slab the overriding plate is already in compression for $\mu = 0$. When we include slab normal forcing (through v_{retr}) and allow for dip angle changes we also find a reversal in sign (from tension to compression) of deviatoric stresses in the overriding plate with increasing friction. Model 14 is the same as model 8 except for an average coefficient of friction of $\mu = 0.05$ on the subduction fault. Relative to model 8 tension in the back-arc area is reduced, while the velocity of trench retreat reduces. Subsidence of the overriding plate margin after 80 km of convergence increases with nearly 2.5 km. The increase in compression and reduction of trench retreat with increasing friction on the subduction fault is caused by the stronger coupling of the subducting to the overriding plate. The extreme would be the case in which the plates are fully coupled (i.e. locked contact) and no differential displacement occurs along the subduction fault. The horizontal velocity of the subducting plate ($\overline{v}_{sub}$) would then induce large compression in both surface plates.

4.3.5 Vertical motions induced by variations in a subduction zone system

Changes in a subduction zone system are reflected in horizontal and vertical surface displacements. The results we have obtained show that vertical surface displacements at a convergent plate margin are sensitive to buoyancy of the subducting plate, friction on the subduction fault, retrograde motion of the slab, and resistance to changes in dip angle. By comparing vertical displacements we can predict the effects which changes in the subduction zone parameters will have. To this purpose Fig. 4.10 shows vertical surface displacements relative to the surface of model 1. The topography of the models is compared after the same amount of convergence of 80 km. For model 1 this is obtained after 2 Myr. The topographic profiles are aligned to the same trench position, before the profile of model 1 is subtracted. These are surface displacements which would be induced if the subduction of model 1 would be changed with respect to one of the examined parameters. The maximum surface displacement varies between approximately -6 and 8 km. In all cases the displacements are largest near the plate margins. On average a region of around 200 km is affected. The lateral extent of this region is, however, determined by our choice for the effective elastic thickness of the lithospheric plates.

A change in the effective pull force (F_{eff}) can be due to a change in density of the subducting plate relative to the mantle or a change in the viscous resistance which is experienced by the slab. Our results show that an increase in F_{eff} leads to subsidence which amounts approximately -4 km at maximum for an increase by a factor of 2 (Fig. 4.10a). Decrease in F_{eff} leads to uplift. Subduction of a slab which has no effective buoyancy

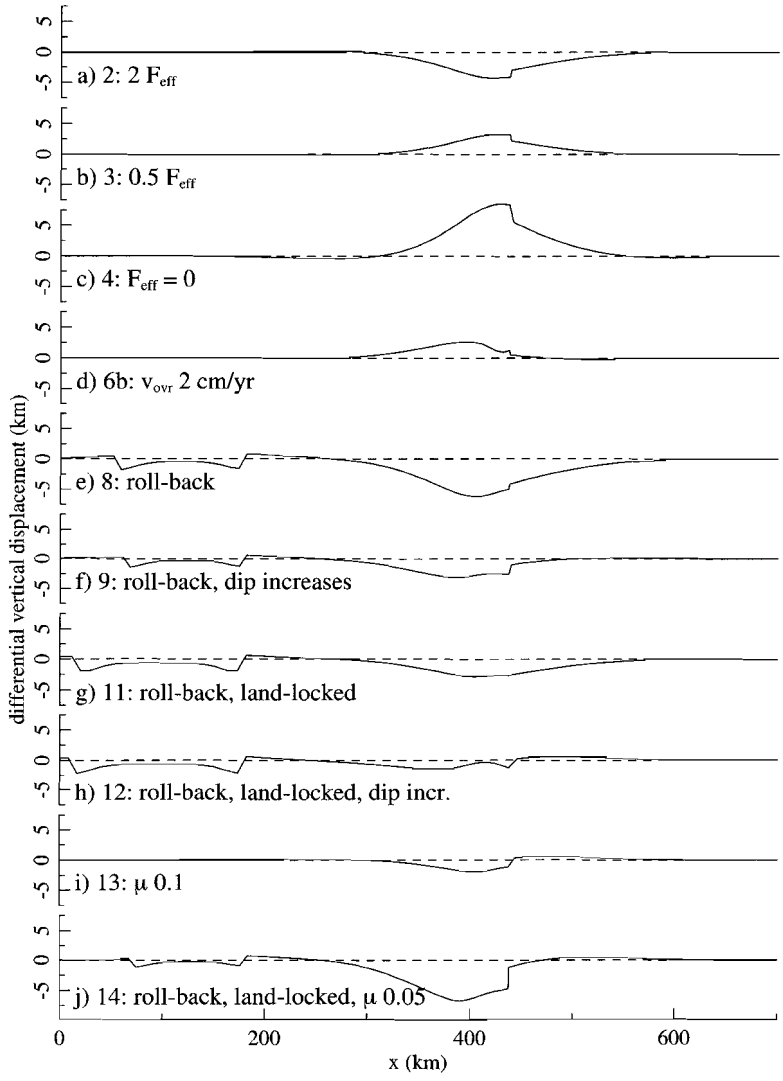

Figure 4.10: Differential vertical surface displacements resulting from changes in the subduction zone parameters. Displacements are relative to the reference model (model 1) (Fig. 4.3) after 80 km of convergence. Trench positions have been aligned before subtraction. Vertical scale is 6 times exaggerated. a) Increase in F_{eff}, b) decrease in F_{eff}, c) $F_{eff} = 0$, d) $v_{ovr} = 2$ cm/yr with resistance to lateral migration of deeper part of the slab, e) roll-back with dip of model slab end fixed, f) roll-back with dip free, g) roll-back in land-locked basin setting with dip of model slab end fixed, h) roll-back in land-locked basin setting with dip free, i) friction along the subduction fault, and j) roll-back in land-locked basin setting with friction along the subduction fault and dip free. Values of relevant parameters and model numbers are shown in the lower left corner of the panels.

leads to very large uplift (maximum around 8 km). A change in slab buoyancy might lead to a change in the velocity of the subducting plate at the surface as the system seeks a new equilibrium. In models 2, 3 and 4 we assume that such an adjustment does not occur and is, for example, prevented by the interaction with other lithospheric plates. A change in motion of the overriding plate with respect to the reference model leads to trench migration. When the motion of the overriding plate changes from zero to advancing, uplift of the overriding plate margin is induced only in case retrograde motion of the deeper part of the subducted slab is prevented (Fig. 4.10d). Fig. 4.10e shows that subsidence of the overriding plate margin may be expected in case of subduction zone retreat caused by the negative buoyancy of the slab. The maximum subsidence is reduced with more than 3 km when the dip angle of the subducting slab is allowed to increase (Fig. 4.10f). Subsidence of the overriding plate margin is (more than half) less for models of subduction zone roll-back in a land-locked basin setting than for models in which the retrograde motion is superposed on the 'normal' (non-migrating) subduction (Fig. 4.10g and h). Extension in the back-arc area leads to the development of a basin (Fig. 4.10e-h). Friction on the subduction fault will induce subsidence of the overriding plate margin (Figs. 4.10i and j).

In case the subducted plate is free to adjust to changes in the system (for example, through adjustment of velocity or dip angle), vertical surface displacements are not affected by variations in the velocity of the subducting plate or overriding plate at the surface.

4.4 Discussion

4.4.1 Trench retreat

Our results indicate that different driving mechanisms for trench retreat may have different expressions in vertical surface displacement of the overriding plate margin. For trench retreat forced by the motion of the overriding plate we expect higher topography than for the case of trench retreat due to the negative buoyancy of the slab. This signal would be superimposed on the topographic expressions of other processes active near a convergent plate margin, for example, magmatism and underplating. An example of trench retreat forced by the motion of the overriding plate may be found along the west coast of South America, where South America moves towards the subducting Nazca plate [*Chase,* 1978]. Naturally, a component of retreat may still be due to the negative buoyancy of the subducting plate. The average elevation of the Central Andes is near 4 km [*Froidevaux and Isacks,* 1984]. The back-arc region is characterised by a compressional stress regime [*Uyeda and Kanamori,* 1979; *Froidevaux and Isacks,* 1984] Models 6 and 6b (Fig. 4.6) describe continuing subduction with a component of slab roll-back which is caused by the motion of the overriding plate. In both cases the overriding plate is in compression. Compression is higher when retrograde motion of the deeper part of the slab is restricted (model 6b). Note that the amount of trench retreat will be reduced in case significant tectonic erosion occurs [*Lallemand,* 1995]. Large compression in the overriding plate may be induced by stronger coupling of the two plates along the subduction contact (models 13 and 14). Significant coupling, at least at seismogenic scales, is indicated by the large thrust earthquakes at the

Chilean margin [*Uyeda and Kanamori,* 1979]. We find that increased coupling (imposed by larger friction on the subduction fault) slows subduction, while reducing the amount of trench retreat. Also a component of subsidence is added to the overriding plate margin. The observations of continuing subduction and a high topography of the overriding plate margin in the Andes may indicate that very strong coupling is less likely.

Examples of trench retreat due to sinking of the subducting slab under its own negative buoyancy are the Mariana arc [e.g. *Molnar and Atwater,* 1978], Apennines (Italy) [e.g. *Malinverno and Ryan,* 1986] and the Aegean region [e.g. *Le Pichon,* 1982]. All are characterised by extensional back-arc basins.

4.4.2 Model aspects

In this paragraph we further discuss and motivate some aspects, e.g. boundary conditions, of our numerical modelling procedure.

In our modelling, the effects of dynamic processes in the asthenosphere are parameterised through the subducting forcing and the choice of the depth interval in which pressures across the subducted slab are in balance (below P_a in Fig. 4.2). Models 5 and 10 show that vertical surface displacements are especially sensitive to this latter aspect, the choice of P_a. It is assumed that in the depth interval below P_a pressure increments due to the hydrostatic pressure cancel each other. P_a is defined by the (perpendicular downward projection) of the point of contact of the overriding plate with the subducting plate at the surface. The location of P_a may be affected by the density of the overriding plate, the presence of a large accretionary wedge at the surface and pressure differences in the asthenosphere near the corner region. As shown by models 5 and 10 the formation of rather large surface displacements (e.g. Fig. 4.10c) may be prevented by shifting P_a. We prefer at this stage to define P_a in the same manner for the models of Fig. 4.10 and not define arbitrary shifts between the models.

The insensitivity of the model to variations in surface velocity can be explained by the partitioning of factors which drive deformation in a pull force acting on the slab and velocities at the surface side boundaries of the plates. In this way the slab is free to immediately adjust to changes in the system, for example, a higher convergence velocity at the surface leads to a higher velocity of the slab. It is to be expected that changes in topography will result if the slab needs a long time to react to changes (i.e. is relatively inert). As illustrated by model 6b for example, trench retreat forced by the overriding plate motion would then induce uplift of the overriding plate margin.

In our quantification of vertical displacements the effects of erosion and sedimentation have not been included. Sedimentation would lead to further subsidence, while the calculated subsidence for some of the models is already quite large. As mentioned above, pressure differences in the mantle, for example, may act to reduce surface displacements. The effect of gravity within the plates has also been neglected in the models. Therefore, gravitational spreading of topographic highs, which will reduce surface uplift, is not taken into account.

In our model formulation we assume that a shallow slab dip may result from dynamic equilibrium between slab and upper mantle, in contrast with *Becker et al.* [1999]. We do

agree with these authors that other processes as, for example, anchoring of the slab at the transition zone between upper and lower mantle or background mantle flow [*Doglioni*, 1993, 1994; *Olbertz et al.*, 1997] may contribute to maintaining a lower slab dip. Such processes were not included in our analysis.

4.5 Conclusions

We have shown that significant vertical surface displacements at convergent plate margins may occur during ongoing subduction. We have quantified these displacements using a two-dimensional (visco)elastic model. The model is used to study the surface effects of subduction zone dynamics on a time scale of a few million years. We conclude that vertical surface displacements induced by changes in a subduction system can reach a magnitude of a few (around 2-4) kilometres on the margins of both the overriding and the subducting plate. The displacements are sensitive to slab buoyancy, friction along the subduction fault, retrograde motion of the slab and (resistance to) changes in dip angle. A decrease in the buoyancy of the subducting plate leads to a deepening of the plate margins, while an increase in buoyancy leads to uplift. An increase in friction along the subduction fault deepens the overriding plate margin. Retrograde motion of the slab induces subsidence of the plate margins. This subsidence is reduced in case of steepening of the slab during roll-back. Roll-back in a land-locked basin setting results in relative uplift in comparison with roll-back imposed on non-migrating subduction. We expect that variations in velocity of the surface plates will induce vertical surface displacements if the subducted slab can not easily adjust to these velocity changes. The actual surface topography is sensitive to the dynamic influence of the asthenosphere.

Trench retreat forced by the motion of the overriding plate is characterised by higher topography on the overriding plate margin than in the case of retreat due to sinking of the negatively buoyant slab. Inplane stress in the back-arc region is compressive for trench retreat due to the overriding plate motion and tensional for trench retreat (roll-back) due to sinking of the slab. Our results confirm the findings of *Hassani et al.* [1997] that an increase in interplate friction can change tension in the overriding plate to compression.

Chapter 5

Two-dimensional simulations of surface deformation caused by slab detachment

5.1 Introduction

Various observations, from sites of former subduction and from present-day convergent plate margins, indicate that the deeper part of subducting lithosphere may mechanically decouple from the lithosphere at the surface. Such detachment of subducted lithosphere could occur after closure of an ocean. An example may be found in the Asian region [*Van der Voo et al.*, 1999]. In the Late Jurassic or Early Cretaceous Siberia and Mongolia collided, closing the ocean in between. The subducted slab sank into the mantle and at present may be found at depths of 1500 km and deeper. A reversal in arc polarity could also be indicative of slab detachment. A reversal requires that subduction on one side of the system stops. Detachment of this slab would make room for subduction of the previously overriding plate. Arc reversals have, among others, been suggested for the New Hebrides and Solomon Islands, Timor and New Britain [*Karig and Mammerickx*, 1972; *Carney and Macfarlane*, 1982; *Price and Audley-Charles*, 1987; *Hamilton*, 1979]. Polarity reversals generally seem to occur during collisional processes, although the example of the New Hebrides shows that this is not a necessary condition [*Karig and Mammerickx*, 1972].

At present, indications for slab detachment exist at various regions of plate convergence. For example, detachment of subducted lithosphere has been suggested on the basis of a noticeable gap in the hypocentra distribution associated with the subducting slab beneath Southern Italy [*Ritsema*, 1972], the New Hebrides [*Pascal et al.*,, 1973] and the Carpathians [*Fuchs et al.*, 1979]. From images of regional tomography studies, a gap in subducted lithosphere has been inferred beneath the Carpathians [*Oncescu et al.*, 1984], the Hellenic

[1] A manuscript based on this chapter has been submitted for publication to *Geophysical Journal International*

arc [*Spakman et al.*, 1988] and Italy [*Wortel and Spakman*, 1992].

The examples given above suggest two different tectonic settings in which slab detachment may occur: after collision (e.g. the Carpathians) or during ongoing convergence (e.g. the New Hebrides). In the latter case detachment may occur, for example, by subduction of a weak zone like a spreading ridge. For detachment in a collisional setting, we consider the closing of an ocean in which the continental margins are irregularly shaped (Fig. 5.1). The margins will collide first at promontories (section A in Fig. 5.1), while in between oceanic lithosphere may remain (section B). Subduction of the oceanic remnants may then take place through roll-back of the subduction zone. When convergence between the continents has stopped, roll-back occurs in a land-locked basin setting [*Le Pichon*, 1982]. An analogue of the closing of such an irregular ocean can be found in the closing of the Tethys ocean in the Mediterranean region. Based on the setting described above, we distinguish two cases in the subduction phase preceding detachment: non-migrating subduction (the promontories) or trench roll-back (the ocean remnants).

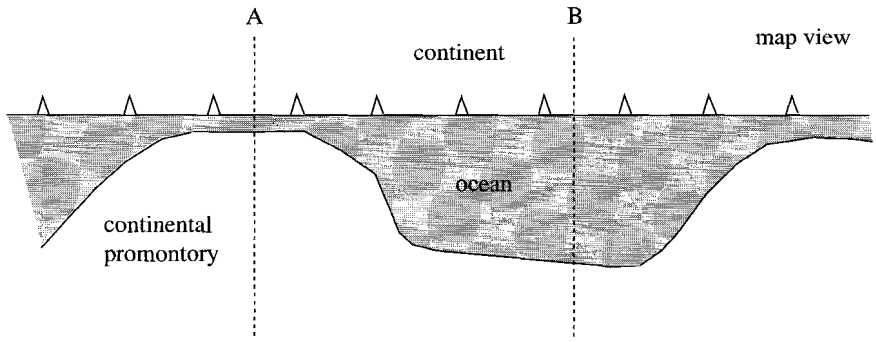

Figure 5.1: Sketch in map view of closing of an ocean with irregular continental margins. Collision takes place first at the promontories (section A). Subsequently, the ocean basin may be subducted through roll-back of the trench system (section B).

Detachment of subducted lithosphere causes changes in a subduction zone system which may be observed at the Earth's surface. Among the expected surface effects are surface uplift [*Westaway*, 1993; *Chatelain et al.*, 1992], a temporal change in stress regime [*Hippolyte et al.*, 1994; *Sorel et al.*, 1988; *Meijer and Wortel*, 1996], and magmatism, metamorphism and rapid exhumation [*Davies and Von Blanckenburg*, 1995; *Von Blanckenburg and Davies*, 1995]. These effects could be rapid and of large magnitude. Interpretation of observations in the context of slab detachment requires a knowledge of the magnitudes which may be expected. In this study, we quantify surface effects of detachment of subducted lithosphere. Our focus lies on displacements of the Earth's surface. Through numerical modelling, we aim to identify the range of displacement magnitudes which can be associated with slab detachment. To quantify surface displacements, we use a two-dimensional, elastic model. We compare the surface topography which develops during subduction with the topography shortly after instantaneous detachment.

A number of previous studies have quantified or estimated surface uplifts of 1 to 2 km resulting from slab detachment [*Mitrovica et al.,* 1989; *Chatelain et al.,* 1992; *Westaway,* 1993; *Schott and Schmeling,* 1998]. *Westaway* [1993] calculates uplift resulting from the immediate replacement in the detachment gap of subducted lithosphere with warmer mantle material. His use of the concept of local isostatic equilibrium is, however, not realistic in a dynamic subduction zone setting. *Chatelain et al.* [1992] focus on surface uplift caused by sinking of the detached part of lithosphere. We adopt their approach to take the effect on uplift into account. *Mitrovica et al.* [1989] and *Schott and Schmeling* [1998] use a dynamic viscous model. Our analysis differs from these two studies in the use of a dynamic model of subduction which includes elasticity in the rheology of the lithosphere. In our model lithospheric stresses may, therefore, remain at higher values. Using a two-dimensional, viscoelastic model, *Giunchi et al.* [1996] and *Carminati et al.* [1999] investigate surface velocities for a short time interval (on the order of 100 kyr) several Myr after detachment occurred. In these studies, detachment does not result in surface uplift. However, these authors do not include the process of detachment in their simulations. The difference with the present study is that we simulate the complete time evolution of subduction followed by slab detachment.

5.2 Modelling method

5.2.1 Subduction

Our approach for modelling ongoing subduction is the same as described in *Buiter et al.* [submitted to GJI/Chapter 4]. We refer to this study for modelling details and summarise only the main features of the method below. We solve the mechanical equilibrium equations using the finite-element code TECTON [*Melosh and Raefsky,* 1980, 1983; *Melosh and Williams,* 1989]. The effect of large deformations are taken into account through the formulation of *Wallace and Melosh* [1994]. We adopt the plane strain approximation. The rheology of our lithospheric plates is elastic. Therefore, the plate thickness in the models is an effective elastic thickness. Models employing plates with an effective elastic thickness adequately simulate surface deflection behaviour at subduction zones [e.g. *Watts and Talwani,* 1974; *Caldwell et al.,* 1976]. This is a support for the elastic plate approximation in our study of changes in surface topography at convergent plate margins. In simulations of trench roll-back, a zone of low viscosity is introduced in the overriding plate to allow for extension. This part of the model has a viscoelastic Newtonian rheology.

Our models are started with the geometry of a short subducted plate (Fig. 5.2). The initial model is set up in a consistent manner such that geometry, boundary conditions and internal stresses are in equilibrium with each other. It includes bending stresses in the subducting plate. The contact between the subducting and overriding plate is a slippery fault [*Melosh and Williams,* 1989], which is allowed to deform, while the differential displacements between the overriding and the subducting plate are locally always parallel to the fault geometry. The fault is free of friction.

We assume that the asthenosphere is an incompressible fluid which is in hydrostatic

equilibrium on the time scale of our model (several Myrs). It is not explicitly included in the model domain for reasons of numerical efficiency. We simulate the interaction of the asthenosphere with the lithospheric plates through a hydrostatic pressure boundary condition. This hydrostatic pressure effectively acts as a restoring pressure which opposes displacement of lithospheric plates at the Earth's surface. At the side boundaries of the surface plates velocity boundary conditions are imposed which simulate the effects of forces outside our model domain (Fig. 5.2).

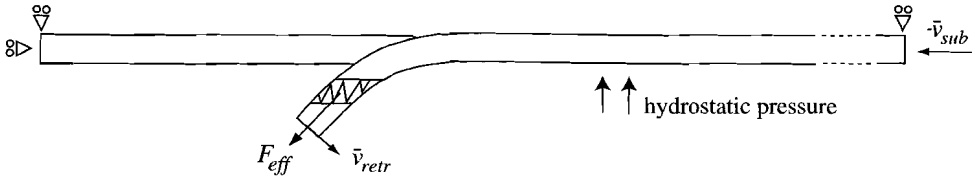

Figure 5.2: Model setup for the subduction phase. The side boundary of the overriding plate is held fixed laterally, while the subducting plate may move with a velocity v_{sub}. Both top corners at the left and right hand side are not allowed to move vertically. The subducting plate feels an effective pull force F_{eff} oriented along dip of the slab and distributed over the zigzag interval. In the models of subduction zone roll-back a slab normal velocity (v_{retr}) is applied at the model slab end.

We assume that for the deeper part of the subducted slab (below our initial model slab end) the along dip component of slab pull is balanced by viscous mantle stresses and by internal stresses in the subducted slab. No net force is, therefore, applied to the deeper slab. The slab parallel velocity remains constant with time. In our models of steady non-migrating subduction we assume that the slab normal component of slab pull and hydrostatic and viscous stresses exerted on the slab by the mantle balance each other. Retrograde motion of the slab can occur if these are not completely in balance. This can be due, for example, to a reduction in dynamic pressures caused by flow of mantle material around the slab in case of a short slab or a narrow (in the along strike direction) subduction zone. The effect of the out-of-balance pressures is simulated with a velocity boundary condition in the slab normal direction applied at the model slab end (v_{retr} in Fig. 5.2).

A driving force of subduction in our model is the effective pull force, F_{eff}, acting on the subducting plate (Fig. 5.2). This force includes the effects of gravitational pull due to the density difference between slab and mantle, resistive forces, and dynamic pressure differences caused by flow in the asthenosphere. It causes the acceleration of subducting lithosphere from zero vertical velocity at the trench to the (vertical component of) convergence velocity at greater depths [for a discussion see *Buiter et al.*, submitted to GJI/Chapter 4]. We determine the magnitude of the pull force by measuring the force on the slab which maintains subduction for a model which is driven by both a velocity at the surface side boundary of the subducting plate and a slab parallel velocity of the same magnitude at the model slab end. This defines F^0_{eff}. The effective pull force acts as a distributed (body type) force in the slab depth interval from 60 to 80 km.

5.2.2 Slab detachment

The topography which develops during the phase of subduction is compared with the topography after detachment. We impose instantaneous detachment through the introduction of a slippery fault [*Melosh and Williams,* 1989] in the subducted lithosphere. The relaxation of forces across the fault is taken to be complete. Detachment in the model is imposed at relatively shallow depths (80-130 km). These depths lie within the range of depths (around 50-300 km) determined from tomographic images [e.g. *Spakman,* 1990] and analyses of lithospheric strength [*Davies and Von Blanckenburg,* 1995; *Wong A Ton and Wortel,* 1997]. After detachment, a velocity boundary condition prescribes the detached part to sink vertically into the mantle. Sinking of the detached lithosphere will cause flow of the viscous mantle. The resulting pressure differences deflect overlying lithosphere downward. As the detached lithosphere sinks further the pressures reduce. As a result, the viscous flow will contribute to surface uplift on a longer time scale (order 100 kyr) [*Chatelain et al.,* 1992]. To obtain a first order estimate of the viscous effect of sinking of the detached part, we use the equivalent of a sphere sinking in an infinite viscous medium below a free surface [*Morgan,* 1965; *Chatelain et al.,* 1992]. The normal stress σ_n at the surface is:

$$\sigma_n(r, D) = 2ga^3\Delta\rho\frac{D^3}{(r^2 + D^2)^{\frac{5}{2}}} \tag{5.1}$$

where r and D are horizontal distance and depth, respectively, to the centre of the sphere, a is radius of the sphere and $\Delta\rho$ is the density difference between the sphere and its surrounding medium. The expression is independent of the viscosity of the viscous medium due to substitution of the sinking velocity which depends inversely on viscosity.

It should be realised that the results of our modelling experiments are constrained by the two-dimensional nature of the models. In the context of slab detachment, this means that our results describe detachment of subducted lithosphere which takes place at the same depth and time along the whole subduction zone. Also the model simulates immediate detachment, while in reality detachment may be expected to require a certain timespan.

In the quantification of surface displacements the effects of erosion, sedimentation or internal density differences are not included.

5.3 Modelling analysis

5.3.1 Subduction

We consider two cases of subduction before detachment: non-migrating subduction and rollback. In case of non-migrating subduction convergence is driven by the effective pull force and a velocity v_{sub} of -4 cm/yr at the surface side boundary of the subducting plate (Fig. 5.2). The negative value indicates motion directed towards the left. The overall convergence between both side boundaries of the model is 4 cm/yr. Our results are not sensitive to the assumed velocity since, for the adopted elastic rheology, time only enters the equations through this velocity boundary condition. We verified that neither topography nor model

stresses vary when evaluated at a given amount of convergence, which was achieved using different convergence velocities. Table 5.1 gives the adopted values for parameters used in the modelling. Fig. 5.3I shows the results of non-migrating subduction at 2 Ma after 80 km of convergence. At this time, the overriding plate margin has subsided nearly 4 km. The dip angle of the subducting slab approximately remains the same with time, although it is allowed to change dynamically.

Retrograde motion of the subducting slab may occur if the slab normal component of slab pull is not completely balanced by dynamic mantle pressures. In our model formulation, the effect of these out-of-balance pressures is simulated through a velocity v_{retr} of 2 cm/yr applied at the model slab end. To simulate roll-back in a land-locked basin setting [*Le Pichon,* 1982], both side boundaries of the surface plates are held fixed laterally. We introduce a 100 km wide weak zone (viscosity 10^{21} Pa s) in the overriding plate to allow for subduction zone roll-back. In this area, extension localises and a back-arc basin forms.

We simulate two cases of subduction zone roll-back. In the first case we assume that the subducted slab is relatively short. The dip angle of the slab is free to change, since resulting changes in dynamic mantle pressures can be accommodated by flow of mantle material around the slab end. In 3.5 Myr the dip angle of the slab increases by 16° (Fig. 5.4I). During this time the trench retreats horizontally with 80 km at an average rate of 2.3 cm/yr. The maximum subsidence of the overriding plate margin is around 2.5 km. In the second case we model a long slab. Changes in dip angle of the deeper part of the slab are unlikely in view of the large mantle pressures which have to be overcome. Therefore, the dip angle of the model slab end is held fixed. After 2.5 Myr, the maximum subsidence of the overriding plate margin is around 7 km (Fig. 5.5I). The average rate of trench retreat is 3.2 cm/yr. For both roll-back models the velocity of trench retreat falls well within the range of values for present-day subduction zones (up to around 5 cm/yr) [*Garfunkel et al.,* 1986; *DeMets et al.*, 1994].

We use these three models to study the effects of detachment of subducted lithosphere on vertical surface displacements. We examine how the surface displacements depend on depth of detachment, resistance to slip on the subduction fault after detachment, and viscous mantle flow due to sinking of the detached part.

5.3.2 Slab detachment

Surface uplift

During collision, convergence between the two approaching plates will slow down and finally stop. In our modelling, we simplify this evolution by simulating continued convergence until detachment, after which convergence stops. For a setting in which detachment occurs during ongoing subduction we, therefore, assume that convergence stops after detachment.

Instantaneous detachment is imposed after 80 km of convergence. For the case of non-migrating subduction this is after 2 Myr (model 1 in Table 5.2). The average depth of the detachment fault is 107 km. Stresses due to viscous flow resulting from sinking of the detached part of lithosphere are not included. Detachment of the deeper part of the

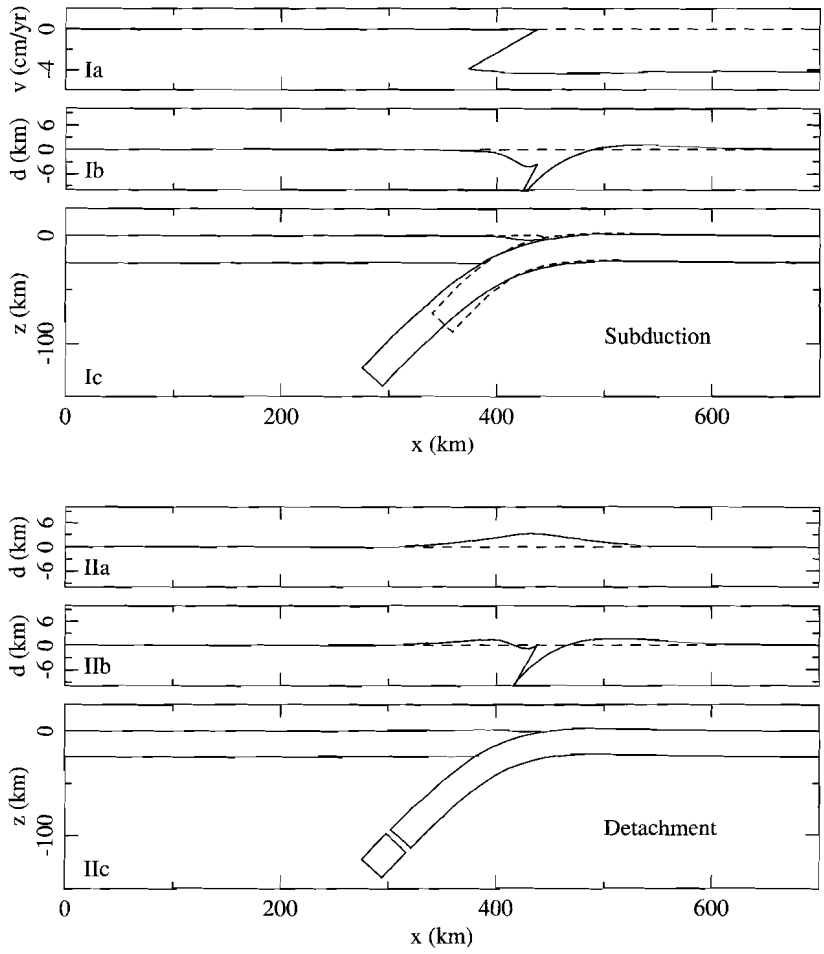

Figure 5.3: Model 1. I. Subduction of a negatively buoyant plate pushed at its surface right hand side with 4 cm/yr. The subducting plate extends further to the right than shown here (initially to 1226 km). The subduction fault is free of friction. Results are shown at 2 Ma after 80 km of convergence. Ia) Horizontal surface velocity averaged over 0.1 Myr (dotted line denotes v = 0 cm/yr), Ib) vertical surface displacement relative to surface of initial model, Ic) outline of model, dotted line is outline of initial model. II. Detachment at 2 Ma. IIa) Surface uplift due to detachment, displacement is relative to surface of model just before detachment; IIb) vertical surface displacement relative to surface of initial model; IIc) outline of model. The small detached lithospheric slab is a numerical feature which is caused by the fact that the deeper part of the subducted slab is not included in the model domain. Its effects are represented by appropriate boundary conditions at the model slab end.

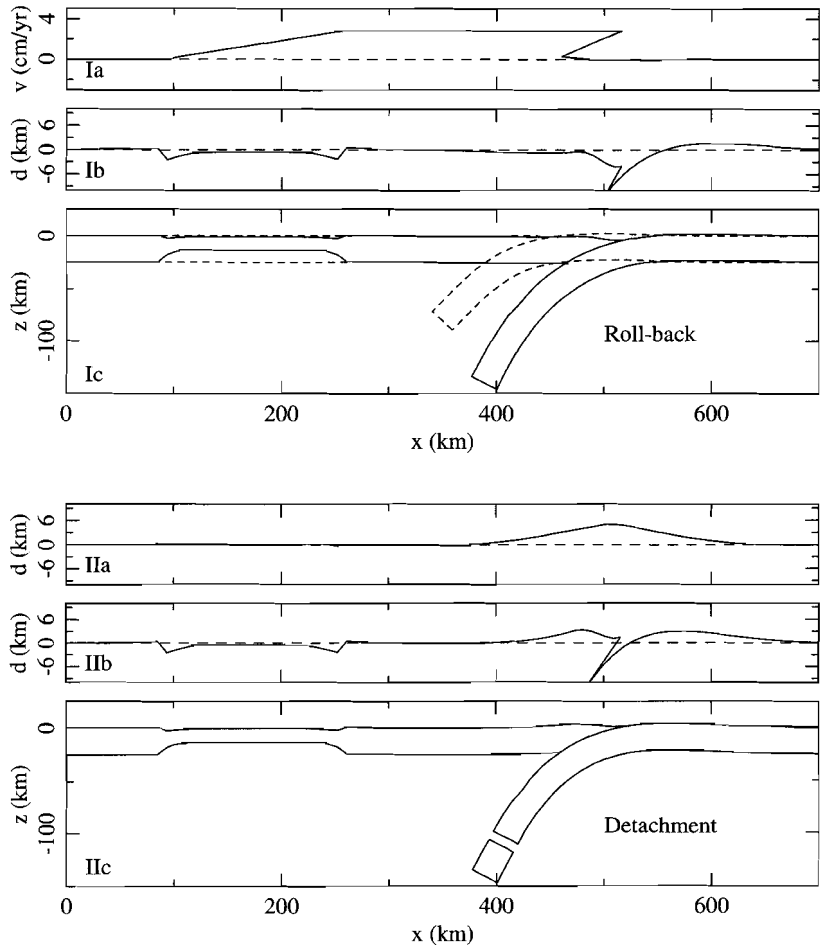

Figure 5.4: Model 10. As Fig. 5.3 for subduction zone roll-back in a land-locked basin setting. The side boundaries of the surface plates are fixed laterally. The dip angle of the slab is free to change. I. Roll-back results after 80 km of convergence at 3.5 Ma. II. Detachment at 3.5 Ma.

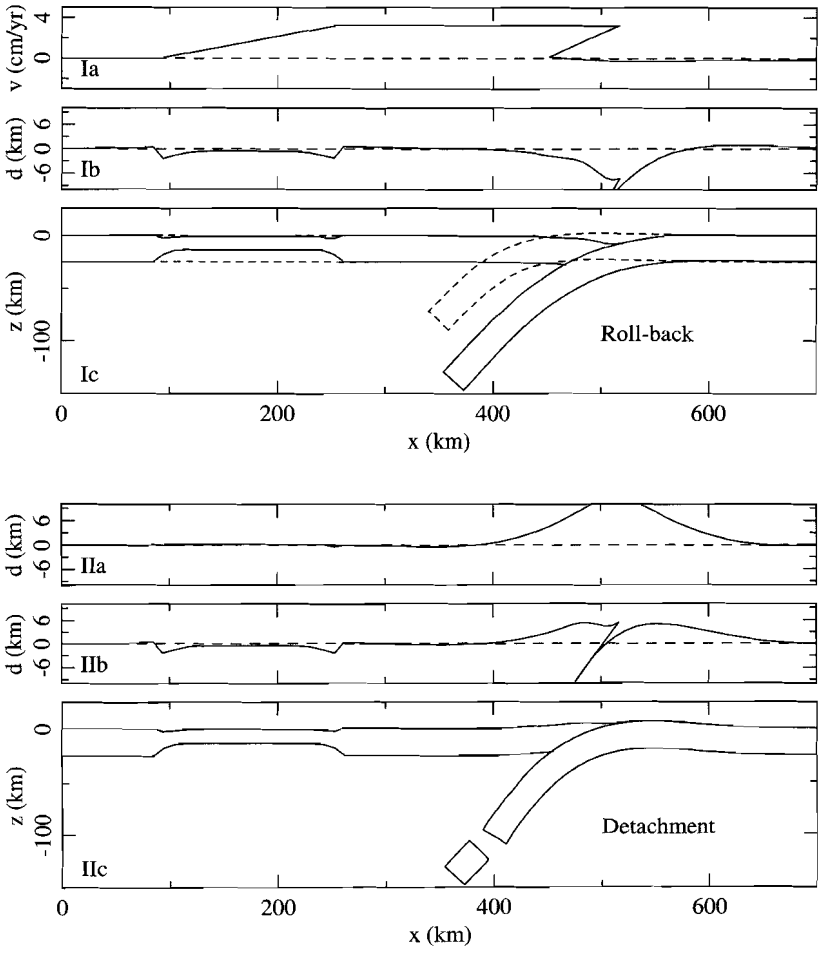

Figure 5.5: Model 12. As Fig. 5.3 for subduction zone roll-back in a land-locked basin setting. The dip angle of the model slab end is fixed to simulate roll-back of a long slab. I. Roll-back results after 80 km of convergence at 2.5 Ma. II. Detachment at 2.5 Ma.

subducted lithosphere leads to surface uplift which is 3 to 4 km at maximum (Fig. 5.3II). The topography on the overriding plate margin has a maximum height of around 1.5 km. The uplift remains at the same value with time after detachment (Fig. 5.6) since convergence has stopped and the elastic model is in equilibrium.

Maximum uplift for detachment in a roll-back situation is higher and amounts to approximately 5 km immediately after detachment for model 10 (Fig. 5.4II). The surface topography has a maximum height of around 3.5 km. The subducting slab steepens with time during the phase of subduction zone roll-back. This leads to bending stresses in the subducting plate which affect surface uplift due to detachment. Uplift decreases with time after detachment. This is caused by the low viscosity zone in the overriding plate which takes up motion of the overriding plate away from the trench. The extensional back-arc basin, therefore, experiences a phase of compression after detachment.

In case of roll-back of a long subducted slab, for which the dip angle can not easily change, uplift after detachment is more than 11 km (model 14, Fig. 5.5II). During the phase of roll-back the overriding plate margin subsided (Fig. 5.5I), therefore, the resulting topography on this plate margin is around 5 km at maximum. The high uplift results from high stresses which develop in the subducting slab during retrograde motion.

parameter	value
Effective plate thickness	25 km
Young's modulus	5×10^{10} Pa
Poisson's ratio	0.25
Viscosity weak zone	10^{21} Pa s
Gravitational acceleration	9.80 m s^{-2}

Table 5.1: Modelling parameters

Depth and orientation of detachment fault

In the above models, detachment occurs at an average depth of around 110 km. The region of the future detachment fault is located just above the forcing interval - the depth interval in which F_{eff} is applied - at the start of subduction. Fig. 5.7 (see also Table 5.2) shows that the depth of detachment largely affects surface uplift. In case detachment is imposed at deeper levels the magnitude of the inplane tensional stresses in the region around the detachment fault is reduced. This reduces surface uplift. Detachment at shallower levels leads to larger surface uplifts. Once the future detachment fault has passed the forcing interval, stresses in the slab around the fault hardly change during further subduction.

The uplift resulting from slab detachment is not very sensitive to the orientation of the detachment fault. For non-migrating subduction, detachment imposed on a slab normal fault, a horizontal fault or a vertical fault results in a variation in uplift of not more than 0.5 km.

Subduction fault locked

In a limited time interval after detachment (on the order of several kyrs) motions on the subduction fault may be reverse to those which occur during subduction. As noted above, this induces a phase of compression in the back-arc basin for the roll-back models. The reversed motion is limited if friction on the subduction fault increases after detachment. This could be due to changes in fault stresses related to the uplift experienced by the lithospheric plates. An end-member case is obtained when the subduction fault completely locks after detachment. This leads to a higher surface uplift after slab detachment, for example, 4.5 km immediately after detachment for the case of non-migrating subduction (model 2 in Table 5.2, compare with 3.2 km for model 1).

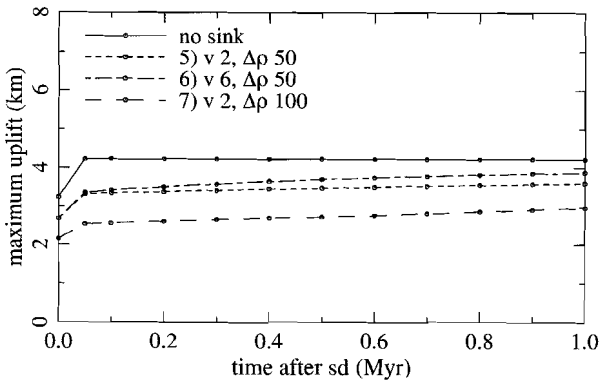

Figure 5.6: Effect of viscous stresses due to sinking of the detached part of lithosphere on maximum uplift versus time after detachment. Reference situation is non-migrating subduction of model 1 (drawn line) with stresses due to sinking not included (see Fig. 5.3). Three dash/dotted lines are for different values for sinking velocity (v) and density difference ($\Delta\rho$) of the sphere (models 5-7). Radius of the sphere is 50 km.

Viscous flow due to sinking detached part

Sinking of the detached part of lithosphere in the viscous mantle will induce flow of mantle material. This flow generates dynamic pressure differences which lead to a downward deflection of the overlying surface. This deflection is reduced as the detached lithosphere sinks further down. With time the Earth's surface will, therefore, be uplifted. To determine a first order of magnitude of this effect we use the equivalent of a sphere sinking in a viscous fluid below a free surface in the same manner as *Chatelain et al.* [1992] [see also *Morgan*, 1965]. We apply the normal stresses (equation 5.1) to lithosphere nearest to the sinking detached lithosphere. The sphere has a radius of 50 km and a density difference of 50 kg m^{-3}. Fig. 5.6 (model 5) shows that for the case of non-migrating subduction the maximum surface uplift after detachment is reduced with 0.5 to 0.9 km compared with model 1 in which the viscous flow pressures are not included. In the period following detachment,

uplift increases by approximately 0.3 km during 1 Myr. During this time the maximum uplift remains below the value for model 1. Uplift rate in the period after detachment is higher for a higher magnitude of the sinking velocity (model 6, Fig. 5.6). A larger density difference for the sphere further reduces the initial surface uplift (model 7). Using this simple analogue of a sinking sphere, we find that sinking of the detached part of lithosphere suppresses surface uplift due to detachment. The reduction is recovered in the period following detachment, leading to surface uplift on the order of several hundreds of metres, in agreement with *Chatelain et al.* [1992].

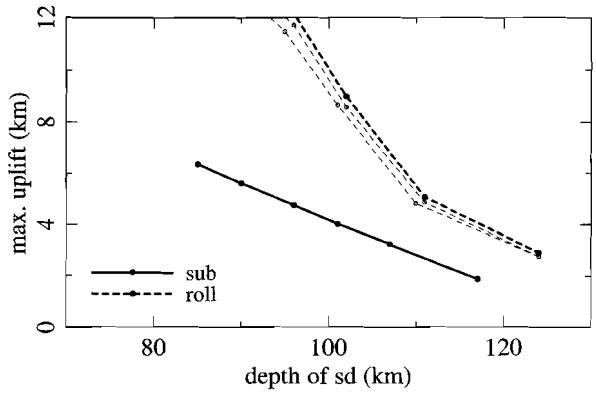

Figure 5.7: Maximum uplift versus depth of detachment. Drawn line: non-migrating subduction (model 1, Fig. 5.3), dotted line: roll-back (model 10, Fig. 5.4). For the roll-back model, viscosity of the weak zone in the overriding plate is 10^{21} Pa s (bold curve), 10^{20} Pa s (upper light curve) and 5×10^{21} Pa s (lower light curve). Detachment is imposed after 80 km of convergence (2 Myr for model 1 and 3.5 Myr for model 10.) Uplift is measured immediately after detachment. Small circles indicate obtained measurements.

Model sensitivity

The calculated surface uplifts are affected by the choice of values for some of the parameters and boundary conditions in the subduction models, for example, effective pull force (F_{eff}), velocity of the side boundary of the subducting plate (v_{sub}) and the viscosity of the weak zone for the roll-back models. As discussed before, stresses in the subducting plate are the same for different values of v_{sub} as long as the same amount of convergence is considered. Model surface uplift is, therefore, not sensitive to the magnitude of convergence velocity. In all models discussed so far F_{eff} is distributed over a depth interval of 60 to 80 km. The force interval is constrained to lie above the initial model slab end and below the region of large bending of the subducting plate. In case the force interval is extended to 60-100 km, surface uplift after detachment is somewhat higher (model 8). A change in slab buoyancy affects the dynamics of the subduction zone system leading to different surface topography [*Buiter et al.*, submitted to GJI/Chapter 4] and stresses in the subducting slab. For example,

model	mode	dip[1]	subd fault[2]	sd. depth[3]	sink param.[4]	uplift[5] (km)		remark
1	sub	free	f	106	–	3.2	4.2	Figs. 5.3, 5.7
2	sub	free	l	106	–	4.5	5.3	
3	sub	free	f	117	–	1.9	2.3	Fig. 5.7
4	sub	free	f	89	–	5.6	8.2	Fig. 5.7
5	sub	free	f	106	2 50 50	2.7	3.3	Fig. 5.6
6	sub	free	f	106	6 50 50	2.7	3.4	Fig. 5.6
7	sub	free	f	106	2 100 50	2.1	2.6	Fig. 5.6
8	sub	free	f	106	–	3.5	4.9	F^0_{eff} [-60,-100]
9	sub	free	f	102	–	2.2	3.2	$0.5 \times F^0_{eff}$
10	roll	free	f	111	–	5.1	4.0	Figs. 5.4, 5.7
11	roll	free	l	111	–	6.1	10.5	
12	roll	free	f	124	–	2.9	2.5	
13	roll	free	f	96	–	12.2	8.8	
14	roll	fix	f	113	–	11.6	20.5	Fig. 5.5

[1] Dip of model slab end is either free or held fixed
[2] After detachment, f: free, l: locked
[3] Average depth of slab detachment
[4] v_{sink} (cm yr^{-1}), $\Delta\rho$ (kg m^{-3}), a (km) (equation 5.1)
[5] Detachment after 80 km of convergence. Maximum uplift is measured at detachment (left value) and 0.1 Myr later (right value)

Table 5.2: Model experiments.

an increase in buoyancy - a decrease in F_{eff} in our model - decreases tensional stresses in the slab. This leads to lower uplift after detachment (model 9). For the roll-back models, the viscosity of the weak zone is one of the parameters which determine the velocity of trench retreat. In models with a high viscosity in the back-arc area trench retreat is slow. The resistance to retreat could induce increased stresses in the subducting slab leading to higher uplift after detachment. Fig. 5.7 shows that the effect of viscosity of the weak zone in the overriding plate is small for viscosities between 10^{20} and 5×10^{21} Pa s.

5.4 Discussion

5.4.1 Comparison with observations

We have found that slab detachment may lead to surface uplift of several kilometres. For the case of non-migrating subduction followed by detachment, maximum surface uplift is 2-6 kilometres. For subduction zone roll-back, uplift may be much higher. When applied to the closing of an irregularly shaped oceanic basin, as outlined in Fig. 5.1, this means that uplift after detachment will be lower at the promontories (section A in Fig. 5.1) in comparison with the area of the ocean remnants (section B).

Care should be taken in comparing our model uplifts with observations. Mountains at sites of continental collision indicate that high surface uplifts may accompany the final stages of a subduction zone system (e.g. the Alps, Carpathians, Himalayas). Such an uplift is the result of all processes active during collision, e.g. crustal thickening, thrusting and - possibly - slab detachment. Uplift due to detachment of subducted lithosphere, therefore, constitutes only part of the surface displacements which may be expected to occur during and after closure of an ocean. No region exists in which slab detachment has unambiguously been identified. We will, therefore, consider some examples of areas where surface uplift has been interpreted in the context of slab detachment. Since our calculated uplift does not include the effects of erosion, it should ideally be compared with rock (or basement) uplift data [*England and Molnar,* 1990]. Timor in the Southern Banda Arc experienced an uplift of around 5 km from Mid Pliocene to recent presumably related to detachment of the downgoing Australian plate [*Audley-Charles*, 1986b; *Price and Audley-Charles,* 1987]. This value is higher than other reported values of uplift after slab detachment. *Van der Meulen et al.* [2000a], for example, find an Early Pliocene uplift which is around 500 m for the Central Apennines foredeep (Italy) [see also *Van der Meulen et al.*, 2000b]. Their type of data is indicative of the minimum amount of uplift, so uplift could have been much higher. Calabria (Southern Italy) has experienced a surface uplift of approximately 700 m which may be due to detachment of the subducting Ionian lithosphere [*Westaway*, 1993]. *Chatelain et al.* [1992] relate Quaternary uplifts of up to 500-700 m at the New Hebrides to slab detachment. Within the uncertainties in observations and in our models, the values we have calculated for uplift due to detachment are, at least partly, within the range of reported values.

5.4.2 Implications for the back-arc region

Retrograde motion of a subducting slab can only occur if the overriding plate allows it. The overriding plate must either be able to follow trench retreat or it extends. In our land-locked basin setting, we allow for roll-back through the introduction of a weak zone in the overriding plate. In this region extension localises and a back-arc basin forms. Our modelling results indicate that in the period immediately following detachment, motion of the overriding plate may be reverse to motions occurring during the phase of roll-back. In that case, the back-arc basin experiences a phase of compression after detachment. This induces relative uplift of the basin surface which may lead to an erosional unconformity in the basin stratigraphy when back-arc subsidence subsequently continues. Further subsidence due to thermal relaxation may be expected for this overall extensional setting.

5.4.3 Displacements during ongoing subduction

Our results indicate that the surface uplift induced by detachment of subducted lithosphere is a characteristic surface observable. To determine just how characteristic it is, we compare it to displacements which can occur during ongoing subduction. In a previous study [*Buiter et al.*, submitted to GJI/Chapter 4] we quantified vertical surface displacements resulting from changes in a subduction zone system, for example, variations in slab buoyancy or

trench migration. We obtained a maximum surface uplift or subsidence on the order of 2 to 4 km. The displacements are mostly centred around the plate contact, on both the overriding and subducting plate margins. The surface uplift resulting from slab detachment is also centred around the plate contact. The range of magnitudes we have obtained encompasses the range of uplifts which can occur during ongoing subduction. Detachment at relatively shallow depths leads to uplifts which are much higher than can be expected during ongoing subduction. From our modelling results we conclude that interpretation of the cause of uplift at a convergent plate margin requires that observations of the regional tectonic setting are taken into account.

5.4.4 Comparison with previous work

Our uplift is substantially higher than the uplift calculated by *Schott and Schmeling* [1998] or *Mitrovica et al.* [1989]. One of the main differences between these dynamic models and our study is the lithospheric rheology which is viscous in the former models and elastic in ours. In our model stresses can remain at higher values with time. All deformation is elastic (except for the weak zone in the overriding plate) and is, therefore, recovered when forces are removed. This leads to larger uplift after detachment. Since the viscous models include the mantle in their computational domain, the effects of sinking of the detached part of lithosphere are taken into account in a consistent manner. Using the analogue of a sinking sphere [*Chatelain et al.,* 1992], we find that sinking of the detached slab only temporarily reduces surface uplift. Therefore, this is not a cause of the difference in surface uplift between our study and *Schott and Schmeling* [1998] or *Mitrovica et al.* [1989].

5.4.5 Model aspects

We have found that variations in calculated surface uplift after slab detachment are due to: a) depth of detachment, b) the effect of viscous stresses due to sinking of the detached part of lithosphere and their sensitivity to sinking velocity, c) resistance to movement along the subduction fault after detachment and d) the subduction model. Below we discuss a number of conceptual aspects of the modelling procedure which influence the uplift we have calculated:

i) Detachment occurs instantaneously. In reality, break-off will probably take some time. This does not affect surface uplift for our elastic rheology, but it can be important if a rheology with a viscous component were used. In that case, modelled surface uplifts may be reduced.

ii) Since the model is two-dimensional, it is implied that detachment occurs at the same time and depth along the whole subduction zone. Three-dimensional aspects like lateral propagation of the detachment fault [*Wortel and Spakman*, 1992] are not included.

iii) We use an effective elastic plate thickness to simulate the deflection behaviour of the lithosphere. Since our model is consistent in its definition of geometry, stresses and forces we believe that the calculated surface uplifts are a good first order approach to reality. However, we expect that the model uplifts will be affected when a different rheology (and plate thickness) would be used. In case permanent deformation occurs due to non-elastic (e.g.

brittle) behaviour, surface uplift after detachment may be reduced. The magnitude of the calculated uplifts is sensitive to the chosen value for the effective elastic thickness of the model plates. In this modelling study we have shown results for one value of elastic plate thickness (25 km). To estimate the effect of a different elastic thickness we have varied the effective thickness with $\pm 20\%$ (5 km). For both non-migrating subduction and roll-back the maximum uplift after detachment does not change with more than $\pm 10\%$.
iv) In a continental collision setting, convergence will slow down until finally the subducted slab dangles in the mantle beneath the suture. Since viscous resistive stresses acting on the slab diminish with the reduction in subduction velocity, the slab experiences an increase in slab pull. This would induce a deepening of the Earth's surface. However, this deepening disappears after detachment when the whole pull force is removed - including the extra pull which was build up during the last phases of collision. Neglecting this additional pull force should, therefore, not affect surface uplifts if considered relative to the topography during subduction.
v) The pull force F_{eff} is applied at a shallow depth interval. This results in tension in the slab which is constant for slab material which has passed through the force interval. An increase in resistance which the slab may experience at deeper depths, for example, due to the transition between upper and lower mantle, is not included in the model. It is, therefore, assumed that the compression which may be induced by such a resistance is not transferred to the depths of detachment. In support, we note that the very occurrence of slab detachment indicates that the subducted slab must have been in tension.

5.5 Conclusions

Our model calculations indicate that detachment of subducted lithosphere may lead to surface uplift of several kilometres near the plate margins. The exact amount of uplift is sensitive to a) the subduction phase preceding detachment, b) depth of detachment, c) resistance to movement along the subduction fault after detachment, and d) viscous stresses generated by sinking of the detached part of the slab. Our results are obtained for detachment at relatively shallow levels, i.e. around 100 km depth. For non-migrating subduction followed by detachment we find maximum uplifts of 2-6 km, while for the case of roll-back this may be higher by 1-4 km (free slab dip) or even more (constrained slab dip). In case of subduction zone roll-back, the back-arc basin may experience a phase of compression following detachment. Within the uncertainties in observations and in our models, the calculated uplift values are partly within the range of reported values. The surface uplift in part overlaps vertical displacements which result from variations in an ongoing subduction situation [*Buiter et al.*, submitted to GJI/Chapter 4]. The regional tectonic setting should, therefore, be taken into account when interpreting uplift observations in a convergent plate margin setting.

Chapter 6

Surface uplift due to slab detachment: A modelling study for Northern Italy

6.1 Introduction

From tomographic images for the Italian region (Fig. 6.1) it has been inferred that Adriatic lithosphere has subducted westward beneath Italy to depths of several hundreds of kilometres [*Spakman et al.,* 1993; *Amato et al.,* 1993]. At present, this subduction zone system may be in the final stages of its evolution. This is indicated by, for example, the continental nature of the Adriatic lithosphere, the lack of subduction related earthquakes, and the low convergence velocity [*Noomen et al.,* 1996]. Such a situation is favourable for detachment of subducted lithosphere to occur [*Yoshioka and Wortel,* 1995]. In the regional tomographic images of *Spakman* [1990] and *Spakman et al.* [1993] a gap exists at depths of approximately 150 to 250 km in the subducted Adriatic lithosphere. These authors infer the gap to result from slab detachment. However, *Piromallo and Morelli* [1997] and *Amato et al.* [1998] find no evidence in their tomographic results for slab detachment below Northern Italy. Tomographic studies are, therefore, not conclusive regarding the existence of slab detachment in this region. An alternative approach to this problem may be formed by analysis of observations. It is expected that slab detachment leads to uplift of the Earth's surface [*Wortel and Spakman,* 1992; *Westaway,* 1993]. In Northern Italy, indications exist for a significant Late Miocene uplift [*Ricci Lucchi,* 1986; *Van der Meulen et al.,* 2000b]. This uplift has been interpreted by *Van der Meulen et al.* [2000b] in the context of slab detachment. In this study, we adopt another approach and focus on mechanical aspects of the process of slab detachment. Our aim is to test whether slab detachment below Northern Italy may lead to a significant surface uplift. To this purpose we use a numerical model subject to constraints imposed by the geological setting of the region.

6.2 Geological setting

The islands of Corsica and Sardinia have remained at the same location relative to stable Europe since approximately the Early/Middle Miocene [*Dewey et al.,* 1989; *Boccaletti et al.,* 1990b]. The Tyrrhenian basin opened by eastward roll-back of the Italian subduction zone system from a position adjacent to Corsica-Sardinia [*Boccaletti et al.,* 1976; *Malinverno and Ryan,* 1986; *Doglioni,* 1991] (Fig. 6.1). In our area of study (schematically indicated in

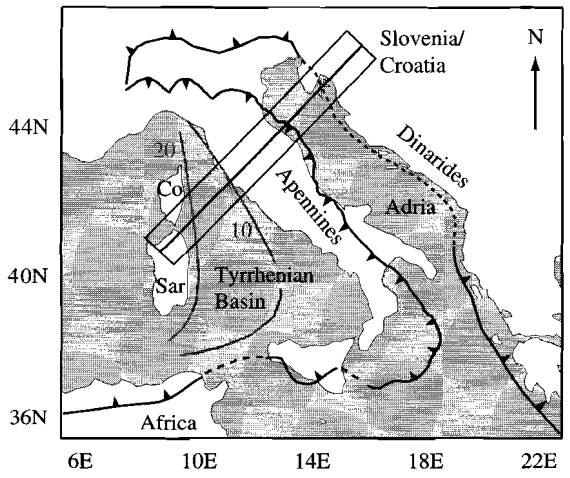

Figure 6.1: Map of the Italian region. Co = Corsica, Sar = Sardinia. Barbed line denotes convergent zones. Two older stages of the Italian subduction zone (with age in Ma) are schematically indicated. Line within the box indicates the location of a section for which our modelling results are representative.

Fig. 6.1), the distance between Corsica-Sardinia and Slovenia/Croatia (former Yugoslavia) hardly changed during this period. This is analogous to a land-locked basin setting [*Le Pichon,* 1982]. The land-locked basin setting does not conflict with the northern-central Dinarides subduction zone on the eastern side of Adria, since subduction here terminated in the Eocene-Oligocene [*Pamić et al.,* 1998]. Relative to Europe, the velocity of the Adriatic lithosphere in the direction of our section (Fig. 6.1) does not exceed 3.5 mm/yr. This is true either in case Adria is assumed to move as part of the African plate [*Channell et al.,* 1979; *Dercourt et al.,* 1986; rotation poles from *Royer et al.,* 1992; *Ricou,* 1994] or independently of Africa [*Platt et al.,* 1989; *Mantovani,* 1990; rotation pole from *Ward,* 1994]. This velocity is small compared with the average rate of roll-back of the Northern Italian subduction zone. From the tectonic reconstructions of *Dewey et al.* [1989], *Dercourt et al.* [1986] and *Boccaletti et al.* [1990b] we infer an average roll-back velocity from 16 Ma to present of nearly 1.5 cm/yr.

Wortel and Spakman [1992] suggest that detachment of the subducted Adriatic lithosphere occurred by lateral migration of a horizontal tear in the plate southward along strike of the Italian convergent plate margin. As lateral migration of slab detachment continues,

the resulting redistribution of slab-pull forces is hypothesised to result in an along strike migration of a surface deepening (which may act as a depocentre), followed by an uplift. The data of *Van der Meulen et al.* [1998] indicate a rapid southward shift of the depocentre of the Apenninic foredeep from the Northern to the Central Apennines area during the Late Miocene. When this lateral depocentre shift is interpreted as a surface signal of slab detachment, this indicates nearly simultaneous detachment below a considerable segment of the Apenninic arc. Therefore, we consider it to be justified to use a two-dimensional model to simulate the potential surface effects of slab detachment in this region.

We adopt the age of the observed lateral depocentre shift, around 9/8 Ma, as a first constraint on the timing of slab detachment. In the tomographic images of *Spakman* [1990], the gap in the subducted Adriatic lithosphere is seen at a depth of around 150 to 250 km. The amount of plate convergence in our study area since 8/9 Ma is approximately 100 km [*Dercourt et al.,* 1986; *Dewey et al.,* 1989; *Boccaletti et al.,* 1990b]. For a moderate slab dip this indicates that detachment initially may have occurred at a depth between 60 and 180 km. This depth is within the range (around 50-300 km) determined on the basis of analysis of lithospheric strength [*Davies and Von Blanckenburg,* 1995; *Wong A Ton and Wortel,* 1997].

6.3 Uplift data

There is evidence for a Late Miocene phase of uplift in the Northern Apennines which is remarkable both in magnitude and in its limited extent in space and time. *Ricci Lucchi* [1986] identified a Late Miocene phase of uplift and erosion for the External Ligurides in present-day middle Northern Italy. This uplift is probably not related to thrusting as there is no evidence for horizontal displacement of the Ligurian sheet during this period. The uplift is supported by the apatite fission-track data of *Balestrieri et al.* [1996] which suggest an exhumation of more than 3 km starting at around 8-9 Ma for the Internal Ligurides of Northwest Italy. This type of observation gives only part of the rock uplift [*England and Molnar,* 1990] for an uplifting region. From analysis of paleobathymetric data, *Van der Meulen et al.* [2000b] found a Late Miocene uplift of the Apenninic foredeep of around 500 m at minimum. In the same period the central Apenninic foredeep was a region of subsidence [*Van der Meulen et al.,* 1998]. The uplift of the Northern Apennines probably ended in the Messinian as is evidenced by a new phase of subsidence in the foredeep [*Van der Meulen et al.,* 1998] and the presence of lower Pliocene sediments on top of the External Ligurides [*Ricci Lucchi,* 1986]. The uplift of the Internal Ligurides probably continued until present [*Balestrieri et al.,* 1996]. In summary, the available data indicate an uplift of the Northern Apennines of 500 m at minimum, which may have been larger by 2-3 km.

6.4 Modelling method

We use a two-dimensional numerical model to simulate subduction zone roll-back followed by slab detachment. Below we give a summary of the modelling method. For a complete

description we refer to Chapters 4 and 5.

We solve the mechanical equilibrium equations with a finite element method using TECTON [*Melosh and Raefsky,* 1980, 1983; *Melosh and Williams,* 1989; *Wallace and Melosh,* 1994]. The deflection behaviour of the subducting and overriding lithosphere is simulated through the use of plates with an effective elastic thickness. These are well suited for the study of surface deflections at subduction zones [e.g. *Caldwell et al.,* 1976]. We use an effective elastic thickness of 25 km. which is within the range of values [10-40 km] obtained with plate flexure studies for this area [*Royden,* 1988; *Buiter et al.,* 1998/Chapter 3]. In a land-locked basin setting, subduction zone roll-back can occur only if the overriding plate extends. To allow for extension, a zone of low viscosity is introduced in the overriding plate. This part of the model has a viscoelastic Newtonian rheology. In the weak zone extension localises and a back-arc basin forms. The initial location and width of the weak zone are determined from the present geometry taking into account a stretching factor of approximately 4 for the Tyrrhenian area since the Middle Miocene.

The starting model for the roll-back phase (Fig. 6.2) includes bending stresses in the subducting plate. We assume that the asthenosphere is an incompressible fluid which is in hydrostatic equilibrium on the time scales we are interested in. The asthenosphere is not part of the model domain. Its interaction with the lithospheric plates is represented by a hydrostatic pressure boundary condition. Subduction is driven by an effective pull force. This is a net force which includes the effect of the density difference between slab and mantle, viscous resistance and dynamic pressure differences caused by flow in the asthenosphere. In our land-locked basin context, roll-back is taken to result from a net force acting in a direction perpendicular to the slab. This force will have a significant contribution from the deeper slab which is not part of our model domain. In the model, the slab normal force is approximated by a velocity (v_{retr}) acting at the model slab end.

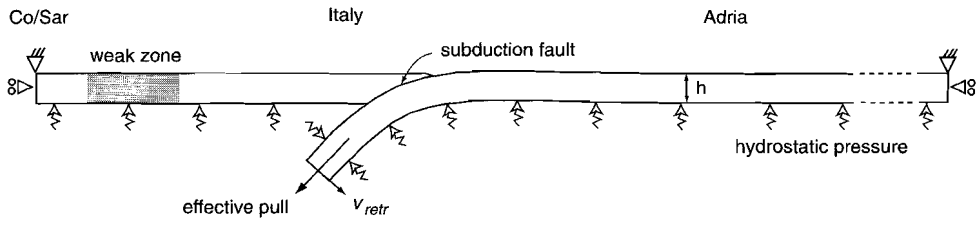

Figure 6.2: Model setup for subduction zone roll-back in a land-locked basin setting. Subduction is driven by a slab parallel effective pull force and a slab normal velocity (v_{retr}). Subduction fault is frictionless. Effective elastic plate thickness (h) is 25 km. Young's modulus 5×10^{10} Pa, Poisson's ration 0.25.

Instantaneous detachment of the subducting plate is imposed after a period of subduction zone roll-back which is sufficiently long in order for the model to overcome initialisation signatures (typically a few Myr). The effects of sedimentation or erosion are not included.

6.5 Roll-back and detachment

Fig. 6.3-I shows modelling results for 4.5 Myr of subduction zone roll-back for the section indicated in Fig. 6.1. During this time the trench has retreated approximately 65 km at an average rate of roll-back of 1.4 cm/yr. This value results from a slab normal velocity (v_{retr}) of 1.3 cm/yr and a viscosity of the weak zone of 10^{21} Pa s. These values have been selected in order to match the average velocity of roll-back for the Northern Italian subduction zone of nearly 1.5 cm/yr [*Dercourt et al.,* 1986; *Dewey et al.,* 1989; *Boccaletti et al.,* 1990b]. At 4.5 Ma the overriding plate margin has subsided approximately 2.8 km. Roll-back has resulted in extension in the back-arc area. The subducted slab is in tension due to the exerted effective pull force.

After 4.5 Myr of roll-back instantaneous detachment is imposed at an average depth of approximately 110 km. This depth is selected on the basis of the inferred depth of detachment for Northern Italy (see Geological setting section). Fig. 6.3-II shows that detachment leads to a maximum surface uplift of approximately 4.5 km centred around the plate contact. Maximum surface topography on the overriding plate margin is 3.6 km. In the period following detachment surface uplift reduces. The overriding plate moves away from the trench, in the direction opposite to the motions occurring during the phase of roll-back. As a result, the back-arc basin experiences a phase of compression after detachment. This leads to relative uplift of the basin surface which may be reflected by an unconformity in the basin stratigraphy when (thermal) subsidence subsequently continues.

6.6 Discussion

The calculated uplift is sensitive to various model parameters and assumptions. We briefly discuss the most important of these below. A different choice of effective elastic plate thickness affects the flexural behaviour of the lithospheric plates and, hence, vertical displacements. Our effective elastic thickness of 25 km is a representative value for the subducting Northern Adriatic plate [*Royden,* 1988; *Buiter et al.,* 1998/Chapter 3]. We cannot indicate how appropriate it is for the lithosphere of Northern Italy. However, we have found that a decrease or increase in elastic thickness of the whole model with $\pm 20\%$ (5 km) only changes the model uplift with around $\pm 10\%$ at maximum (approximately 0.5 km). The surface uplift resulting from detachment is not sensitive to the duration of the phase of subduction zone roll-back as long as initialisation signatures have been overcome. For our model this is after approximately 2 Myr. Including viscous stresses due to sinking of the detached part of lithosphere [*Chatelain et al.,* 1992] temporarily reduces the model surface uplift by 0.5 to 1 km [Chapter 5]. Friction on the subduction fault after detachment, for example due to changes in fault stress, leads to higher model uplifts (by possibly more than 1 km).

The uplifts determined in this study are valid for our parameterisation of the process of slab detachment. Conceptual aspects of the modelling procedure will affect model uplifts. For example, surface uplift may be enhanced by the replacement of colder lithosphere with warmer asthenosphere in the detachment gap. We expect that surface uplift will be reduced in case permanent deformation due to a non-elastic (e.g. brittle) rheology would be taken

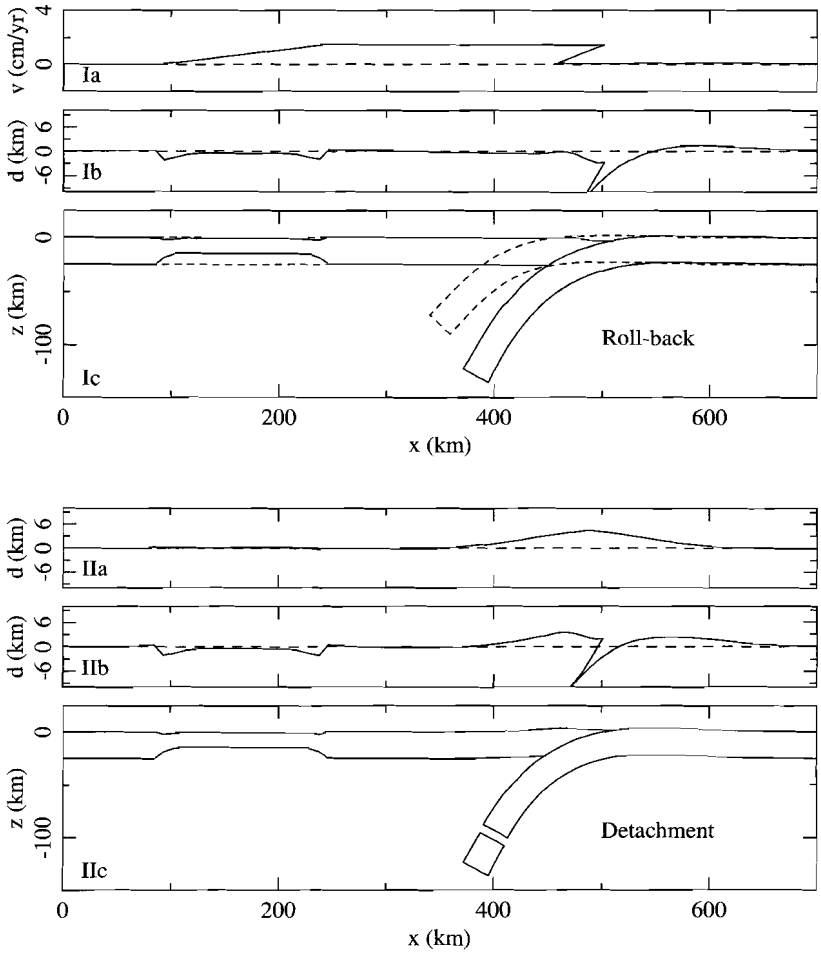

Figure 6.3: I. Subduction zone roll-back. The side boundaries of the surface plates are fixed laterally. Results are shown after 65 km of convergence at 4.5 Ma. Ia) horizontal surface velocity averaged over 4.5 Myr, Ib) vertical surface displacement relative to surface of initial model, Ic) model configuration, dotted line is outline of initial model. II. Detachment at 4.5 Ma. Results are shown immediately thereafter. IIa) surface uplift due to detachment, displacement is relative to surface of model just before detachment; IIb) vertical surface displacement relative to surface of initial model (IIb = Ib + IIa); IIc) outline of model. The deeper part of the subducted slab is not depicted, since it is not part of the model domain. The effects of the slab being longer are included through boundary conditions at the model slab end (Fig. 6.2).

into account.

In a related study for Northern Italy, *Carminati et al.* [1999] [see also *Giunchi et al.*, 1996] found that surface uplift rates after detachment are lower compared with rates occurring during subduction. These authors study a short period several Myrs after detachment occurred and, therefore, do not include the process of slab detachment. In our simulations we find that uplift occurs shortly after detachment.

6.7 Conclusions

The Italian region serves as an example of a subduction zone system in the terminal stages of its evolution. In this stage subducted lithosphere may become detached from the lithosphere at the surface. However, tomographic images for this region are not conclusive regarding the existence of a detachment gap. We find that significant vertical displacements of the Earth's surface are to be expected if slab detachment occurs. In the Late Miocene the Northern Apennines experienced an uplift which is clearly distinct in space and time from the vertical motions of the surrounding region. Geological data indicate that uplift was 0.5 km at minimum, up to 3.5 km at maximum. Using a numerical model subject to constraints imposed by the geological setting of the region, we have shown that uplifts in the observed magnitude range may have resulted from detachment of subducted lithosphere. Our modelling results indicate that detachment after a phase of subduction zone roll-back in a land-locked basin setting leads to a surface uplift of 4-5 km at maximum. We find that following detachment a stress inversion may occur in the back-arc basin.

References

Amato, A., B. Alessandrini, and G.B. Cimini, 1993, Teleseismic wave tomography of Italy, in *Seismic tomography: theory and practice*, edited by H.M. Iyer and K. Hirahara, Chapman & Hall, London, pp. 153-194.

Amato, A., L. Margheriti, R. Azzara, A. Basili, C. Chiarabba, M.G. Ciaccio, G.B. Cimini, M. Di Bona, A. Frepoli, F.P. Lucente, C. Nostro, and G. Selvaggi, 1998, Passive seismology and deep structure in Central Italy, *Pure appl. geophys., 151*, 479-493.

Ambrosetti, P., C. Bosi, F. Carraro, N. Ciaranfi, M. Panizza, G. Papani, L. Vezzani, and A. Zanferrari, 1987, Neotectonic map of Italy, *C.N.R., Quad. Ric. Sci., 4*.

Anderson, E. M., 1951, The dynamics of faulting and dyke formation with applications to Britain, *Oliver and Boyd*, Edinburgh, 206 pp.

Anderson, H., and J. Jackson, 1987, The deep seismicity of the Tyrrhenian Sea, *Geophys. J. R. astr. Soc., 91*, 613-637.

Audley-Charles, M.G., 1986a, Timor-Tanimbar Trough: the foreland basin of the evolving Banda orogen, *Spec. Publs. int. Ass. Sediment., 8*, 91-102.

Audley-Charles, M.G., 1986b, Rates of Neogene and Quaternary tectonic movements in the Southern Banda Arc based on micropalaeontology, *J. Geol. Soc. Lond., 143*, 161-175.

Balestrieri, M.L., E. Abbate, and G. Bigazzi, 1996, Insights on the thermal evolution of the Ligurian Apennines (Italy) through fission-track analysis, *J. Geol. Soc. Lond., 153*, 419-425.

Bally, A.W., L. Burbi, C. Cooper, and R. Ghelardoni, 1986, Balanced sections and seismic reflection profiles across the Central Apennines, *Mem. Soc. Geol. It., 35*, 257-310.

Barazangi, M., and B.L. Isacks, 1979, Subduction of the Nazca plate beneath Peru: evidence from spatial distribution of earthquakes, *Geophys. J. R. astr. Soc., 57*, 537-555.

Barberi, F., P. Gasparini, F. Innocenti, and L. Villari, 1973, Volcanism of the southern Tyrrhenian Sea and its geodynamic implications, *J. Geophys. Res., 78*, 5221-5232.

Becker, T.W., C. Faccenna, R.J. O'Connell, and D. Giardini, 1999, The development of slabs in the upper mantle: Insights from numerical and laboratory experiments, *J. Geophys. Res., 104*, 15,207-15,226.

Beekman, F., 1994, Tectonic modelling of thick-skinned compressional intraplate deformation, *Ph.D. thesis Vrije Universiteit*, Amsterdam, 152 pp.

Boccaletti, M., F. Horvath, M. Loddo, F. Mongelli, and L. Stegena, 1976, The Tyrrhenian and Pannonian basins: a comparison of two Mediterranean interarc basins, *Tectonophysics, 35*, 45-69.

Boccaletti, M., C. Conedera, P. Dainelli, and P. Gočev, 1982, The recent (Miocene-Quaternary) regmatic system of the western Mediterranean region. A new model of ensialic geodynamic evolution, in a context of plastic/rigid deformation, *J. Petr. Geol., 5*, 31-49.

Boccaletti, M., F. Calamita, G. Deiana, R. Gelati, F. Massari, G. Moratti, and F. Ricci Lucchi, 1990a, Migrating foredeep-thrust belt system in the northern Apennines and southern Alps, *Palaeo. Palaeo. Palaeo., 77*, 3-14.

Boccaletti, M., N. Ciaranfi, D. Cosentino, G. Deiana, R. Gelati, F. Lentini, F. Massari, G. Moratti, T. Pescatore, F. Ricci Lucchi, and L. Tortorici, 1990b, Palinspastic restoration and paleogeographic reconstruction of the peri-Tyrrhenian area during the Neogene, *Palaeo. Palaeo. Palaeo., 77*, 41-50.

Bodine, J. H., 1981, The thermal-mechanical properties of the oceanic lithosphere, *Ph.D. Thesis*, Columbia University.

Bodine, J.H., M.S. Steckler, and A.B. Watts, 1981, Observations of flexure and the rheology of the oceanic lithosphere, *J. Geophys. Res., 86*, 3695-3707.

Bott, M.H.P., 1991, Sublithospheric loading and plate-boundary forces, *Phil. Trans. R. Soc. Lond. A, 337*, 83-93.

Bott, M.H.P., 1993, Modelling the plate-driving mechanism, *J. Geol. Soc. Lond., 150*, 941-951.

Braun, J., 1988, Styles of continental extension: results from numerical experiments, *unpublished Ph.D. thesis*, pp. 352, Dalhousie University, Halifax, Nova Scotia.

Buiter, S.J.H., M.J.R. Wortel, and R. Govers, 1998, The role of subduction in the evolution of the Apennines foreland basin, *Tectonophysics, 296*, 249-268.

Burov, E.B., and M. Diament, 1992, Flexure of the continental lithosphere with multilayered rheology, *Geophys. J. Int., 109*, 449-468.

Burov, E.B., and M. Diament, 1995, The effective elastic thickness (T_e) of continental lithosphere: What does it really mean? *J. Geophys. Res., 100*, 3905-3927.

Byerlee, J., 1978, Friction of Rocks, *Pure appl. geophys., 116*, 615-626.

Cahill, T., and B.L. Isacks, 1992, Seismicity and shape of the subducted Nazca plate, *J. Geophys. Res., 97*, 17,503-17,529.

Calcagnile, G., and G.F. Panza, 1981, The main characteristics of the lithosphere-asthenosphere system in Italy and surrounding regions, *Pure appl. geophys., 119*, 865-879.

Calcagnile, G., F. D'Ingeo, P. Farrugia, and G.F. Panza, 1982, The lithosphere in the Central-eastern Mediterranean area, *Pure appl. geophys., 120*, 389-406.

Caldwell, J.G., W.F. Haxby, D.E. Karig, and D.L. Turcotte, 1976, On the applicability of a universal elastic trench profile, *Earth Planet. Sci. Lett., 31*, 239-246.

Carminati, E., C. Giunchi, A. Argnani, R. Sabadini, and M. Fernandez, 1999, Plio-Quarternary vertical motion of the Northern Apennines: Insights from dynamic modelling, *Tectonics, 18*, 703-718.

Carney, J.N., and A. Macfarlane, 1982, Geological evidence bearing on the Miocene to recent structural evolution of the New Hebrides arc, *Tectonophysics, 87*, 147-175.

Cattin, R., H. Lyon-Caen, and J. Chéry, 1997, Quantification of interplate coupling in subduction zones and forearc topography, *Geophys. Res. Lett., 24*, 1563-1566.

Čermák, V., 1979, Heat Flow Map of Europe, in *Terrestrial Heat Flow in Europe* edited by V. Čermák and L. Ryback, Springer-Verlag, Berlin, pp. 3-40.

Channell, J.E.T., and J.C. Mareschal, 1989, Delamination and asymmetric lithospheric thickening in the development of the Tyrrhenian Rift, in *Alpine Tectonics* edited by M.P. Coward, D. Dietrich and R.G. Park, Geol. Soc. Spec. Publ., 45, pp. 285-302.

Channell, J.E.T., B. D'Argenio, and F. Horvath, 1979, Adria, the African Promontory, in Mesozoic Mediterranean Palaeogeography, *Earth Science Rev., 15*, 213-292.

Chapman, D.S., 1986, Thermal gradients in the continental crust, *Geol. Soc. Spec. Publ.,*

24, 63-70.

Chapple, W.M., and D.W. Forsyth, 1979, Earthquakes and bending of plates at trenches, *J. Geophys. Res., 84*, 6729-6749.

Chase, C.G., 1978, Extension behind island arcs and motions relative to hot spots, *J. Geophys. Res., 83*, 5385-5387.

Chatelain, J., P. Molnar, R. Prévot, and B. Isacks, 1992, Detachment of part of the downgoing slab and uplift of the New Hebrides (Vanuatu) islands, *Geophys. Res. Lett., 19*, 1507-1510.

Chopra, P.N., and M.S. Paterson, 1981, The experimental deformation of dunite, *Tectonophysics, 78*, 453-473.

Christensen, U.R., 1996, The influence of trench migration on slab penetration into the lower mantle, *Earth Planet. Sci. Lett., 140*, 27-39.

Cloetingh, S., H. McQueen, and K. Lambeck, 1985, On a tectonic mechanism for regional sealevel variations, *Earth Planet. Sci. Lett., 75*, 157-166.

Comer, R.P., 1983, Thick plate flexure, *Geophys. J. astr. Soc. 72*, 101-113.

Comer, R.P., 1986, Comments on: 'Thick-plate flexure re-examined' by Detlef Wolf, *Geophys. J. astr. Soc.*, 85, 467-468.

Conrad, C.P., and B.H. Hager, 1999, Effects of plate bending and fault strength at subduction zones on plate dynamics, *J. Geophys. Res., 104*, 17,551-17,571.

Conte, S.D., and C. de Boor, 1965, Elementary numerical analysis: an algorithmic approach, *McGraw-Hill*, New-York, 432 pp.

Cross, T.A., and R.H. Pilger, Jr., 1982, Controls of subduction geometry, location of magmatic arcs, and tectonics of arc and back-arc regions, *Geol. Soc. Am. Bull., 93*, 545-562.

Crough, S.T., 1975, Thermal model of oceanic lithosphere, *Nature, 256*, 388-390.

Cucci, L., and F.R. Cinti, 1998, Regional uplift and local tectonic deformation recorded by the Quaternary marine terraces on the Ionian coast of Northern Calabria (southern Italy), *Tectonophysics, 292*, 67-83.

Davies, H.J., and F. Von Blanckenburg, 1995, Slab breakoff: A model of lithospheric detachment and its test in the magmatism and deformation of collisional orogens, *Earth Planet. Sci. Lett., 129*, 85-102.

De Jonge, M.R., and M.J.R. Wortel, 1990, The thermal structure of the Mediterranean upper mantle: a forward modelling approach, *Terra Nova, 2*, 609-616.

De Jonge, M.R., M.J.R. Wortel, and W. Spakman, 1994, Regional scale tectonic evolution and the seismic velocity structure of the lithosphere and upper mantle: the Mediterranean region, *J. Geophys. Res., 99*, 12,091-12,108.

DeMets, C., R.G. Gordon, D.F. Argus, and S. Stein, 1994, Effect of recent revisions to the geomagnetic reversal time scale on estimates of current plate motions, *Geophys. Res. Lett., 21*, 2191-2194.

Dercourt, J., L.P. Zonenshain, L.-E. Ricou, V.G. Kazmin, X. Le Pichon, A.L. Knipper, C. Grandjacquet, I.M. Sbortshikov, J. Geyssant, C. Lepvrier, D.H. Perchersky, J. Boulin, J.-C. Sibuet, L.A. Savostin, O. Sorokhtin, M. Westphal, M.L. Bazhenov, J.P. Lauer, and B. Biju-Duval, 1986, Geological evolution of the Tethys belt from the Atlantic to the Pamirs since the Lias, *Tectonophysics, 123*, 241-315.

De Rito, R.F., F.A. Cozzarelli, and D.S. Hodge, 1986, A forward approach to the problem

of nonlinear viscoelasticity and the thickness of the mechanical lithosphere, *J. Geophys. Res., 91*, 8295-8313.

Dewey, J.F., M.L. Helman, E. Turco, D.H.W. Hutton, and S.D. Knott, 1989, Kinematics of the western Mediterranean, in *Alpine Tectonics* edited by M.P. Coward, D. Dietrich, and R.G. Park, Geol. Soc. Lond. Spec. Publ., 45, pp. 265-283.

Doglioni, C., 1991, A proposal for the kinematic modelling of W-dipping subductions - possible applications to the Tyrrhenian-Apennines system, *Terra Nova, 3*, 423-434.

Doglioni, C., 1993, Some remarks on the origin of foredeeps, *Tectonophysics, 228*, 1-20.

Doglioni, C., 1994, Foredeeps versus subduction zones, *Geology, 22*, 271-274.

Dvorkin, J., A. Nur, G. Mavko, and Z. Ben-Avraham, 1993, Narrow subducting slabs and the origin of backarc basins, *Tectonophysics, 227*, 63-79.

Dziewonski, A.M., and D.L. Anderson, 1981, Preliminary reference Earth model, *Phys. Earth Planet. Inter., 25*, 297-356.

Elsasser, W.M., 1971, Sea-floor spreading as thermal convection, *J. Geophys. Res., 76*, 1101-1112.

England, P., and P. Molnar, 1990, Surface uplift, uplift of rocks, and exhumation of rocks, *Geology, 18*, 1173-1177.

Faccenna, C., P. Davy, J. Brun, R. Funiciello, D. Giardini, M. Mattei, and T. Nalpas, 1996, The dynamics of back-arc extension: an experimental approach to the opening of the Tyrrhenian Sea, *Geophys. J. Int., 126*, 781-795.

Froidevaux, C., and B.L. Isacks, 1984, The mechanical state of the lithosphere in the Altiplano-Puna segment of the Andes, *Earth Planet. Sci. Lett., 71*, 305-314.

Fuchs, K., K.-P. Bonjer, G. Bock, I. Cornea, C. Radu, D. Enescu, D. Jianu, A. Nourescu, G. Merkler, T. Moldoveanu, and G. Tudorache, 1979, The Romanian earthquake of March 4, 1977. II. Aftershocks and migration of seismic activity, *Tectonophysics, 53*, 225-247.

Garfunkel, Z., C.A. Anderson, and G. Schubert, 1986, Mantle circulation and the lateral migration of subducted slabs, *J. Geophys. Res., 91*, 7205-7223.

Giardini, D., and M. Velonà, 1991, The deep seismicity of the Tyrrhenian Sea, *Terra Nova, 3*, 57-64.

Giunchi, C., R. Sabadini, E. Boschi, and P. Gasperini, 1996, Dynamic models of subduction: geophysical and geological evidence in the Tyrrhenian Sea, *Geophys. J. Int., 126*, 555-578.

Gripp, A.E., and R.G. Gordon, 1990, Current plate velocities relative to the hotspots incorporating the Nuvel-1 global plate motion model, *Geophys. Res. Lett., 17*, 1109-1112.

Gurnis, M., 1992, Rapid continental subsidence following the initiation and evolution of subduction, *Science, 255*, 1556-1558.

Gurnis, M., C. Eloy, and S. Zhong, 1996, Free-surface formulation of mantle convection – II. Implication for subduction-zone observables, *Geophys. J. Int., 127*, 719-727.

Hamilton, W., 1979, Tectonics of the Indonesian region, *Geol. Survey Prof. Paper, 1078*, U.S. Gov. printing office, Washington, 345 pp.

Hassani, R., D. Jongmans, and J. Chéry, 1997, Study of plate deformation and stress in subduction processes using two-dimensional models, *J. Geophys. Res., 102*, 17,951-17,965.

Hetényi, M., 1946, Beams on elastic foundation. Theory with applications in the fields of

civil and mechanical engineering, *Ann Arbor: the University of Michigan Press.*

Hippolyte, J.-C., J. Angelier, and F. Roure, 1994, A major geodynamic change revealed by Quaternary stress patterns in the Southern Apennines (Italy), *Tectonophysics, 230*, 199-210.

Houseman, G.A., and D. Gubbins, 1997, Deformation of subducted oceanic lithosphere, *Geophys. J. Int., 131*, 535-551.

Hughes, T.J.R., 1987, The finite element method, linear static and dynamic finite element analysis, *Prentic-Hall, Inc.*, Englewood Cliffs, New Jersey, 803 pp.

Hughes, T.J.R., and R.L. Taylor, 1978, Unconditionally stable algorithms for quasi-static elasto/visco-plastic finite element analysis, *Comput. Struct.* 8, 169-173.

Jaeger, J.C., and N.G.W. Cook, 1979, Fundamentals of rock mechanics, *John Wiley and Sons*, New York, 585 pp.

Jordan, T.E., 1981, Thrust loads and foreland basin evolution, Cretaceous, Western United States, *Am. Ass. Petr. Geol. Bull., 65*, 2506-2520.

Karig, D.E., and J. Mammerickx, 1972, Tectonic framework of the New Hebrides island arc, *Marine Geology, 12*, 187-205.

Karner, G.D., and A.B. Watts, 1983, Gravity anomalies and flexure of the lithosphere at mountain ranges, *J. Geoph. Res., 88*, 10,449-10,477.

Karner, G.D., M.S. Steckler, and J.A. Thorne, 1983, Long-term thermo-mechanical properties of the continental lithosphere, *Nature, 304*, 250-253.

Keating, P., 1995, Error estimation and optimization of gravity surveys, *Geophys. Prospecting, 43*, 569-580,

Kooi, H., 1991, Tectonic modelling of extensional basins: the role of lithospheric flexure, intraplate stress and relative sea-level change, *Ph.D. Thesis*, Vrije Universiteit Amsterdam.

Kruse, S.E., and L.H. Royden, 1994, Bending and unbending of an elastic lithosphere: The Cenozoic history of the Apennine and Dinaride foredeep basins, *Tectonics, 13*, 278-302.

Lallemand, S., 1995, High rates of arc consumption by subduction processes: Some consequences, *Geology, 23*, 551-554.

Laubscher, H.P., 1988, The arcs of the Western Alps and the Northern Apennines: an updated view, *Tectonophysics, 146*, 67-78.

Le Pichon, X., 1982, Land-locked oceanic basins and continental collision: the Eastern Mediterranean as a case example, in *Mountain building processes* edited by K.J. Hsü, Academic Press, London, pp. 201-211.

Loddo, M., and F. Mongelli, 1979, Heat Flow in Italy, in *Terrestrial Heat Flow in Europe* edited by V. Čermák, and L. Ryback, Springer-Verlag, Berlin, pp. 221-231.

Lundberg, N., and R.J. Dorsey, 1988, Synorogenic sedimentation and subsidence in a Plio-Pleistocene collisional basin, Eastern Taiwan, in *New perspectives in basin analysis*, edited by K.L. Kleinspehn and C. Paola, Springer-Verlag, New-York, U.S., pp. 265-280.

Malinverno, A., and W.B.F. Ryan, 1986, Extension in the Tyrrhenian Sea and shortening in the Apennines as result of arc migration driven by sinking of the lithosphere, *Tectonics, 5*, 227-245.

Mantovani, E., D. Babbucci, D. Albarello, and M. Mucciarelli, 1990, Deformation pattern in the central Mediterranean and behavior of the African/Adriatic promontory, *Tectono-*

physics, 179, 63-79.

Mantovani, E., D. Albarello, D. Babbucci, and C. Tamburelli, 1993, Post-Tortonian deformation pattern in the central Mediterranean: a result of extrusion tectonics driven by the Africa-Eurasia convergence, in *Recent evolution and seismicity of the Mediterranean region* edited by E. Boschi, E. Mantovani, and A. Morelli, Kluwer, Dordrecht, pp. 65-104.

Marton, F.C., C.R. Bina, S. Stein, and D.C. Rubie, 1999, Effects of slab mineralogy on subduction rates, *Geophys. Res. Lett., 26*, 119-122.

McAdoo, D.C., J.G. Caldwell, and D.L. Turcotte, 1978, On the elastic-perfectly plastic bending of the lithosphere under generalized loading with application to the Kuril Trench, *Geophys. J. R. astr. Soc., 54*, 11-26

McAdoo, D.C., C.F. Martin, and S. Poulouse, 1985, Seasat observations of flexure: evidence for a strong lithosphere, *Tectonophysics, 116*, 209-222.

McKenzie, D.P., 1969, Speculations on the consequences and causes of plate motions, *Geophys. J. R. astr. Soc., 18*, 1-32.

McNutt, M.K., M. Diament, and M.G. Kogan, 1988, Variations of elastic plate thickness at continental thrust belts, *J. Geophys. Res., 93*, 8825-8838.

Meijer, P.Th., and M.J.R. Wortel, 1996, Temporal variations in the stress field of the Aegean region, *Geophys. Res. Lett., 23*, 439-442.

Meissner, R., Th. Wever, and E.R. Flüh, 1987, The Moho in Europe - Implications for crustal development, *Annales Geophysicae, 5B*, 357-364.

Melosh, H.J., and A. Raefsky, 1980, The dynamical origin of subduction zone topography, *Geophys. J. R. astr. Soc., 60*, 333-354.

Melosh, H.J., and A. Raefsky, 1983. Anelastic response of the earth to dip slip earthquakes, *J. Geophys. Res., 88*, 515-526.

Melosh, H.J., and C.A. Williams, Jr., 1989, Mechanics of graben formation in crustal rocks: A finite element analysis, *J. Geophys. Res., 94*, 13,961-13,973.

Meulenkamp, J.E., M. Kováč, and I. Cicha, 1996, On Late Oligocene to Pliocene depocentre migrations and the evolution of the Carpathian-Pannonian system, *Tectonophysics, 266*, 301-317.

Mitrovica, J.X., C. Beaumont, and G.T. Jarvis, 1989, Tilting of continental interiors by the dynamical effects of subduction, *Tectonics, 5*, 1079-1094.

Molnar, P., and T. Atwater, 1978, Interarc spreading and Cordilleran tectonics as alternates related to the age of subducted oceanic lithosphere, *Earth Planet. Sci. Lett., 41*, 330-340.

Morelli, C., M.T. Carrozzo, P. Ceccherini, I. Finetti, C. Gantar, M. Pisani, and P. Schmidt di Friedberg, 1969, Regional geophysical study of the Adriatic Sea, *Boll. Geof. Teor. Appl., 11*, 3-48.

Moretti, I., and L. Royden, 1988, Deflection, gravity anomalies and tectonics of doubly subducted continental lithosphere: Adriatic and Ionian Seas, *Tectonics, 7*, 875-893.

Morgan, W.J., 1965, Gravity anomalies and convection currents, *J. Geophys. Res., 70*, 6175-6187.

Morgan, J. P., E.M. Parmentier, and J. Lin, 1987, Mechanisms for the origin of mid-ocean ridge axial topography: Implications for the thermal and mechanical structure of accreting plate boundaries, *J. Geophys. Res., 92*, 12,823-12,836.

Mostardini, F., and S. Merlini, 1986, Appennino Centro Meridionale, Sezioni Geologiche e

Proposta di Modello Strutturale, *Mem. Soc. Geol. It., 35*, 177-202.

Negredo, A.M., R. Sabadini, and C. Giunchi, 1997, Interplay between subduction and continental convergence: a three-dimensional model for the Central Mediterranean, *Geophys. J. Int., 131*, F9-F13.

Nolet, G., G.F. Panza, and R. Wortel, 1978, An Averaged Model for the Adriatic Subplate, *Pure appl. geophys., 116*, 1284-1298.

Noomen, R., T.A. Springer, B.A.C. Ambrosius, K. Herzberger, D.C. Kuijper, G.-J. Mets, B. Overgaauw, and K.F. Wakker, 1996, Crustal deformations in the Mediterranean area computed from SLR and GPS observations *J. Geodyn., 21,* 73-96.

Olbertz, D., M.J.R. Wortel, and U. Hansen, 1997, Trench migration and subduction zone geometry, *Geophys. Res. Lett., 24,* 221-224.

Oncescu, M.C., V. Burlacu, M. Anghel, and V. Smalbergher, 1984, Three-dimensional P-wave velocity image under the Carpathian arc, *Tectonophysics, 106*, 305-319.

Ori, G.G., M. Roveri, and F. Vannoni, 1986, Plio-Pleistocene sedimentation in the Apennnic-Adriatic foredeep (Central Adriatic Sea, Italy), *Spec. Publs. in. Ass. Sediment., 8*, 183-198.

Ori, G.G., G. Serafini, C. Visentin, F. Ricci Lucchi, R. Casnedi, M.L. Colalongo, and S. Mosna, 1991, The Pliocene-Pleistocene Adriatic foredeep (Marche and Abruzzo, Italy): an integrated approach to surface and subsurface geology, 3rd E.A.P.G. Conference, Adriatic foredeep field trip guide book, AGIP.

Owen, D.R.J. and E. Hinton, 1980, Finite elements in plasticity: Theory and Practice, *Pineridge Press Limited*, Swansea, UK, 594 pp.

Pamić, J., I. Gušić, and J. Vladimir, 1998, Geodynamic evolution of the Central Dinarides, *Tectonophysics, 297*, 251-268.

Panza, G.F., and P. Suhadolc, 1990, Properties of the lithosphere in collisional belts in the Mediterranean - a review, *Tectonophysics, 182*, 39-46.

Pascal, G., J. Dubois, M. Barazangi, B. L. Isacks, and J. Oliver, 1973, Seismic velocity anomalies beneath the New Hebrides island arc: evidence for a detached slab in the upper mantle, *J. Geophys. Res., 78*, 6998-7004.

Peper, T., 1993, Tectonic control on the sedimentary record in foreland basins, *Ph.D. Thesis*, Vrije Universiteit Amsterdam.

Pirazzoli, P.A., M. Arnold, P. Giresse, M.L. Hsieh, and P.M. Liew, 1993, Marine deposits of late glacial times exposed by tectonic uplift on the east coast of Taiwan, *Mar. Geology, 110*, 1-6.

Piromallo, C., and A. Morelli, 1997, Imaging the Mediterranean upper mantle by P-wave travel time tomography, *Ann. di Geof., 40*, 963-979.

Platt, J.P., J.H. Behrmann, P.C. Cunningham, J.F. Dewey, M. Helman, M. Parish, M.G. Shepley, S. Wallis, and P.J. Weston, 1989, Kinematics of the Alpine arc and the motion history of Adria, *Nature, 337*, 158-161.

Price, N.J., and M.G. Audley-Charles, 1987, Tectonic collision processes after plate rupture, *Tectonophysics, 140*, 121-129.

Ranalli, G., 1987, Rheology of the earth, *Allen and Unwin Inc.*, Winchester, USA, 366 pp.

Ranalli, G., 1994, Nonlinear flexure and equivalent mechanical thickness of the lithosphere, *Tectonophysics, 240*, 107-114.

Ravnik, D., D. Rajver, M. Poljak, and M. Živić, 1995, Overview of the geothermal fields of Slovenia in the area between the Alps, the Dinarides and the Pannonian basin, *Tectonophysics, 250*, 135-149.

Ricci Lucchi, F., 1986, The Oligocene to recent foreland basins of the Northern Apennines, *Spec. Publs. in. Ass. Sediment., 8*, 105-139.

Ricou, L-E., 1994, Tethys reconstructed: plates, continental fragments and their Boundaries since 260 Ma from Central America to South-eastern Asia, *Geod. Acta, 7*, 169-218.

Ritsema, A.R., 1972, Deep earthquakes of the Tyrrhenian Sea, *Geol. en Mijnbouw, 51*, 541-545.

Royden, L., 1988, Flexural behavior of the continental lithosphere in Italy: constraints imposed by gravity and deflection data, *J. Geophys. Res., 93*, 7747-7766.

Royden, L.H., 1993, The tectonic expression slab pull at continental convergent plate boundaries, *Tectonics, 12*, 303-325.

Royden, L., and G.D. Karner, 1984, Flexure of the lithosphere beneath Apennine and Carpathian foredeep basins: evidence for an insufficient topographic load, *Am. Ass. Petr. Geol. Bull., 68*, 704-712.

Royden, L., E. Patacca, and P. Scandone, 1987, Segmentation and configuration of subducted lithosphere in Italy: An important control on thrust-belt and foredeep-basin evolution, *Geology, 15*, 714-717.

Royer, J.Y., R.D. Mueller, L.M. Gahagan, L.A. Lawver, C.L. Mayes, D. Nuernberg, and J.G. Sclater, 1992, A global isochron chart, *Technical Report, 117*, University of Texas Institute for Geophysics.

Savostin, L.A., J.-C. Sibuet, L.P. Zonenshain, X. Le Pichon, and M.-J. Roulet, 1986, Kinematic evolution of the Tethys belt from the Atlantic oocean to the Pamirs since the Triassic, *Tectonophysics, 123*, 1-35.

Schott, B., and H. Schmeling, 1998, Delamination and detachment of a lithospheric root, *Tectonophysics, 296*, 225-247.

Serri, G., F. Innocenti, and P. Manetti, 1993, Geochemical and petrological evidence of the subduction of delaminated Adriatic continental lithosphere in the genesis of the Neogene-Quaternary magmatism of central Italy, *Tectonophysics, 223*, 117-147.

Shelton, G., and J. Tullis, 1981, Experimental flow laws for crustal rocks, *EOS, 62*, 396.

Shemenda, A.I., 1993, Subduction of the lithosphere and back arc dynamics: insights from physical modelling, *J. Geophys. Res., 98*, 16,167-16,185.

Sibson, R.H., 1974, Frictional constraints on thrust, wrench and normal faults, *Nature, 249*, 542-544.

Sorel, D., J. Mercier, B. Keraudren, and M. Cushing, 1988, The role of slab-pull force in the Plio-Pleistocene geodynamic evolution of the Aegean arc: subsidence and uplift of the external arc and changes in the tectonic regime, *C.R. Acad. Sci. Paris, t. 307*, 1981-1986.

Spakman, W., 1990, Tomographic images of the upper mantle below central Europe and the Mediterranean, *Terra Nova, 2*, 542-553.

Spakman, W., M.J.R. Wortel, and N.J.Vlaar, 1988, The Hellenic subduction zone: a tomographic image and its geodynamic implications, *Geophys. Res. Lett., 15*, 60-63.

Spakman, W., S. van der Lee, and R. van der Hilst, 1993, Travel-time tomography of the European-Mediterranean mantle down to 1400 km, *Phys. Earth Planet. Int., 79*, 3-74.

Stevenson, D.J., and J.S. Turner, 1977, Angle of subduction, *Nature, 270*, 334-336.

Suhadolc, P., and G.F. Panza, 1989, Physical properties of the lithosphere-asthenosphere system in Europe from geophysical data, in *The lithosphere in Italy, advances in Earth science research* edited by A. Boriani, M. Bonafede, G.B. Piccordo, and G.B. Vai, Acc. Naz. Lincei, Roma, pp. 15-40.

Talwani, M., J.L. Worzel, and M. Landisman, 1959, Rapid gravity computations for two-dimensional bodies with application to the Mendocino fracture zone, *J. Geophys. Res., 64*, 49-59.

Taylor, R.L., P.J. Beresford, and E.L. Wilson, 1976, A non-conforming element for stress analysis, *Int. J. Num. Meth. Eng., 10*, 1211-1219.

Tovish, A., G. Schubert, and B.P. Luyendyk, 1978, Mantle flow pressure and the angle of subduction: non-newtonian corner flows, *J. Geophys. Res., 83*, 5892-5898.

Turcotte, D.L., and G. Schubert, 1982, Geodynamics: applications of continuum physics to geological problems, *John Wiley and Sons, New York*, 450 pp.

Turcotte, D.L., D.C. McAdoo, and J.G Caldwell, 1978, An elastic-perfectly plastic analysis of the bending of the lithosphere at a trench, *Tectonophysics, 47*, 193-205.

Uyeda, S., and H. Kanamori, 1979, Back-arc opening and the mode of subduction, *J. Geophys. Res., 84*, 1049-1061.

Van der Meulen, M.J., J.E. Meulenkamp, and M.J.R. Wortel, 1998, Lateral shifts of Apenninic foredeep depocentres reflecting detachment of subducted lithosphere, *Earth Planet. Sci. Lett., 154*, 203-219.

Van der Meulen, M.J., S.J.H. Buiter, J.E. Meulenkamp, and M.J.R. Wortel, 2000a, An early Pliocene uplift of the central Apenninic foredeep and its geodynamic significance, *Tectonics, 19*, 300-313.

Van der Meulen, M.J., T.J. Kouwenhoven, G.J. van der Zwaan, J.E. Meulenkamp, and M.J.R. Wortel, 2000b, Late Miocene uplift in the Romagnan Apennines and the detachment of subducted lithosphere, *Tectonophysics, 315*, 315-331.

Van der Voo, R., W. Spakman, and H. Bijwaard, 1999, Mesozoic subducted slabs under Siberia, *Nature, 397*, 246-249.

Von Blanckenburg, F., and J.H. Davies, 1995, Slab breakoff: A model for syncollisional magmatism and tectonics in the Alps, *Tectonics, 14*, 120-131.

Wallace, M.H., and H.J. Melosh, 1994, Buckling of a pervasively faulted lithosphere, *Pure appl. Geophys., 142*, 239-261.

Ward, S.N., 1994, Constraints on the seismotectonics of the central Mediterranean from Very Long Baseline Interferometry, *Geoph. J. Int., 117*, 441-452.

Waschbusch, P.J., and L.H. Royden, 1992, Spatial and temporal evolution of foredeep basins: lateral strength variations and inelastic yielding in continental lithosphere, *Basin Res., 4*, 179-196.

Watts, A.B., and J.R. Cochran, 1974, Gravity anomalies and flexure of the lithosphere along the Hawaiian-Emperor seamount chain, *Geophys. J. R. astr. Soc., 38*, 119-141.

Watts, A.B., and M. Talwani, 1974, Gravity anomalies seaward of deep-sea trenches and their tectonic implications, *Geophys. J. R. astr. Soc., 36*, 57-90.

Wessel, P., and A.B. Watts, 1988, On the accuracy of marine gravity measurements, *J. Geophys. Res., 93*, 393-413.

Westaway, R., 1993, Quaternary uplift of southern Italy, *J. Geophys. Res., 98*, 21,741-21,772.

Whittaker, A., M.H.P. Bott, and G.D. Waghorn, 1992, Stresses and plate boundary forces associated with subduction plate margins, *J. Geophys. Res., 97*, 11,933-11,944.

Williams, C.A., and R.M. Richardson, 1991, A rheologically layered three-dimensional model of the San Andreas Fault in Central and Southern California, *J. Geophys. Res., 96*, 16,597-16,623.

Wilson, E.L., R.L. Taylor, W.P. Doherty, and J. Ghaboussi, 1973, Incompatible displacement models, in *Numerical and computer methods in structural mechanics*, edited by Fenves, S.J., N. Perrone, A.R Robinson, and W.C. Schnobrich, Academic Press, New York and London, 43-57.

Wolf, D., 1985, Thick-plate flexure re-examined, *Geophys. J. R. astr. Soc., 80*, 265-273.

Wong A Ton, S.Y.M., and M.J.R. Wortel, 1997, Slab detachment in continental collision zones: An analysis of controlling parameters, *Geophys. Res. Lett., 24*, 2095-2098.

Wortel, M.J.R., and W. Spakman, 1992, Structure and dynamics of subducted lithosphere in the Mediterranean region, *Proc. Kon. Ned. Akad. v. Wetensch., 95*, 325-347.

Wortel, M.J.R., M.J.N. Remkes, R. Govers, S.A.P.L. Cloetingh, and P.Th. Meijer, 1991, Dynamics of the lithosphere and the intraplate stress field, *Phil. Trans. R. Soc. Lond. A, 337*, 111-126.

Yoshioka, S., and M.J.R. Wortel, 1995, Three-dimensional numerical modeling of detachment of subducted lithosphere, *J. Geophys. Res., 100*, 20,223-20,244.

Zhong, S., and M. Gurnis, 1994, Controls on trench topography from dynamic models of subducted slabs, *J. Geophys. Res., 99*, 15,683-15,695.

Zienkiewicz, O.C., 1977, The finite element method, *McGraw-Hill Book Company (UK) Limited*, Maidenhead, UK, 787 pp.

Zienkiewicz, O.C., and I.C. Cormeau, 1974, Visco-plasticity, plasticity, and creep in elastic solids - a unified numerical solution approach, *Int. J. Num. Meth. Eng., 8*, 821-845.

Summary

Convergence of lithospheric plates is accommodated at active margins by one plate moving beneath the other into the Earth's mantle. Changes in this subduction process may cause variations in the topography of the Earth's surface near a convergent plate margin. The focus of this thesis lies on surface displacements which occur during ongoing subduction and in the final stages of a subduction process. During continuing subduction, surface displacements may, for example, be due to changes in buoyancy or plate velocity. In the last phase of a subduction process, surface uplift may result from detachment of subducted lithosphere from the lithosphere at the surface. This study was motivated by indications of slab detachment in regional tomographic images of the Mediterranean region. In general, study of the dynamics of subduction may add to understanding the origin of processes at the Earth's surface, for example, the formation of mountains and basins. Vice versa, analysis of surface data may contribute to insight in the physics of subduction.

Because subduction processes occur at time and depth scales which limit the possibility of direct observation, numerical experiments are used to study the associated surface effects. Two numerical methods form the basis for the models used in Chapters 3-6: a finite difference and a finite element method. In Chapter 2 it is verified that these methods are well suited for simulating the bending (or flexure) of a lithospheric plate during subduction. With the finite element method the equations of mechanical equilibrium are solved. The finite difference method solves the differential flexure equation and, therefore, the method is subject to the assumptions associated with this equation. It is found that the constraints of small deflections and a thin plate pose no serious limitations to the accuracy of the solution for values of plate thickness and deflections typically used in models for flexure of the lithosphere. A horizontal force on a plate with a yield envelope (brittle-plastic) rheology increases the effective elastic flexural rigidity of the plate. Therefore, the plate behaves stiffer.

Detachment of subducted lithosphere may occur by lateral migration of a tear in the slab along strike of the convergent plate margin. In this case, variations in vertical loads are to be expected. In Chapter 3 it is investigated if such variations can be inferred from the deflection date recorded in the Plio-Pleistocene foredeep on the eastern side of Italy. All vertical loads are quantified for two-dimensional sections perpendicular to the strike of the plate margin. The flexural down-bending of the Adriatic plate resulting from known loads, such as topography and sediments, is obtained using a finite difference method (Chapter 2). The unknown slab pull is inferred by constraining the model to fit the base of Pliocene level. For both an elastic and a depth-dependent rheology a trend in vertical loads along strike of the plate margin can not be resolved. Therefore, the hypothesis of lateral migration of slab detachment can neither be shown to be consistent nor inconsistent with the Plio-Pleistocene deflection data.

Vertical surface displacements resulting from slab detachment are referenced to displacements which can occur during the phase of ongoing subduction. In Chapter 4 the effects of variations in a subduction zone system on vertical surface displacements are quan-

tified. To this purpose a two-dimensional elastic finite-element model is used (Chapter 2). First a model is defined in which the subducting plate is driven by its negative buoyancy and a velocity at its surface side boundary. Its equilibrium topography (after around 2 Myr) is the reference level for examination of surface displacements resulting from variations in slab buoyancy, velocity of the surface plates, friction along the interplate contact and subduction zone roll-back. The conclusion of this chapter is that vertical surface displacements during ongoing subduction may reach a magnitude of a few kilometres (2-4) on the overriding and subducting plate margins. Specifically, trench retreat forced by the motion of the overriding plate is characterised by higher topography of the overriding plate margin than the case of retreat due to sinking of the negatively buoyant slab.

Surface uplift resulting from slab detachment is quantified in Chapter 5. The two-dimensional method which is used implies the assumption that the whole subducted plate detaches at the same moment and at the same depth. The surface topography which develops during a phase of subduction is compared with the topography shortly after instantaneous detachment is imposed. Detachment of subducted lithosphere may lead to surface uplift of several kilometres. For non-migrating subduction followed by detachment a maximum surface uplift of 2-6 km is found, while this may be higher for the case of roll-back preceding detachment. Within the context of the models, uplift is sensitive to depth of detachment, resistance to movement on the subduction fault after detachment and viscous stresses generated by sinking of the detached part of the slab. Overall, the surface uplift resulting from slab detachment encompasses the range of vertical displacements which result from variations during ongoing subduction.

In Northern Italy a Late Miocene uplift occurred which can be clearly distinguished in space and time from the geological evolution of the surrounding region. Previous studies linked this uplift to detachment of subducted lithosphere. Using a numerical model subject to constraints imposed by the geological setting of the region, it is shown in Chapter 6 that the uplift in this area can indeed have resulted from slab detachment.

Samenvatting (Summary in Dutch)

De buitenste schil van de aarde – de lithosfeer, met een dikte van ca. 100 tot 200 kilometer – bestaat uit platen die ten opzichte van elkaar bewegen. Beweging van platen naar elkaar toe wordt opgevangen bij subductiezones waar een plaat onder de ander de aardmantel inschuift. Gesubduceerde lithosfeer kan vervolgens honderden kilometers diep wegzakken. Het onderschuivingsproces gaat samen met aardbevingen die in de bovenmantel het traject van de gesubduceerde lithosfeer aangeven. Aan het aardoppervlak kan een actieve plaatgrens worden gemarkeerd door zowel een gebergteketen als een depressie van de (zee)bodem (een bekken).

Veranderingen in het subductieproces kunnen aanleiding geven tot veranderingen in de topografie van het aardoppervlak rond een convergente plaatgrens. Dit proefschrift behandelt verplaatsingen van het aardoppervlak die optreden gedurende voortgaande subductie en in de laatste stadia van een subductieproces. Over het algemeen bedragen horizontale convergentiesnelheden van lithosfeerplaten enige centimeters per jaar. Uit geologische waarnemingen blijkt dat verticale bewegingen gemiddeld een orde van magnitude kleiner zijn: rond enkele millimeters per jaar. Verticale verplaatsingen van het oppervlak tijdens voortgaande subductie kunnen het gevolg zijn van bijvoorbeeld veranderingen in dichtheid of plaatsnelheid. In de laatste fase van een subductieproces kan gesubduceerde lithosfeer mogelijk afbreken van de lithosfeer aan het aardoppervlak. Dit kan leiden tot opheffing van het aardoppervlak. Inzicht in de relatie tussen subductie en de daarmee samenhangende effecten aan het aardoppervlak vormden de algehele motivatie voor dit onderzoek. Studie van de dynamica van subductie kan bijdragen aan het begrijpen van de oorzaak van processen aan het aardoppervlak, zoals bijvoorbeeld het ontstaan van gebergten en bekkens. Andersom kan analyse van oppervlakte data bijdragen aan inzicht in de fysica van het subductieproces.

De regio rond Italië is geselecteerd als gebied voor de studie van de effecten van het afbreken van gesubduceerde lithosfeer. Gedurende miljoenen jaren is de lithosfeer onder de Adriatische Zee westwaarts onder Italië geschoven. Het is te verwachten dat deze subductiezone nu in de laatste fase van zijn ontwikkeling is. Aanwijzingen hiervoor zijn bijvoorbeeld de lage convergentie snelheid, de afwezigheid van subductie-aardbevingen en de continentale aard van de Adriatische plaat. Verder zijn er aanwijzingen in tomografische afbeeldingen van dit gebied voor een onderbreking in de gesubduceerde plaat op een diepte van een paar honderd kilometer. Deze onderbreking kan het gevolg zijn van het afbreken van het diepere deel van de plaat.

Subductie vindt plaats op een tijd- en diepteschaal die de mogelijkheid van directe observaties inperkt. Om deze reden worden hier numerieke experimenten gebruikt om de aan subductie gerelateerde oppervlakte-effecten te bestuderen. De basis voor de modellen in hoofdstuk 3 t/m 6 wordt gevormd door twee numerieke methoden die worden beschreven en geanalyseerd in hoofdstuk 2: een eindige differentie en een eindige elementen methode. Uit hoofdstuk 2 blijkt dat beide methoden goed bruikbaar zijn voor het simuleren van de doorbuiging (of flexuur) van een lithosfeerplaat gedurende subductie.

Het afbreken van gesubduceerde lithosfeer zou kunnen plaatsvinden door laterale mi-

gratie van een min of meer horizontale scheur in de plaat. In deze situatie zouden veranderingen in verticale belasting van de lithosfeerplaat kunnen optreden. In hoofdstuk 3 wordt onderzocht of dergelijke veranderingen bepaald kunnen worden voor de Italiaanse subductiezone. Met een eindige differentie methode (hoofdstuk 2) wordt de doorbuiging van de Adriatische plaat berekend in tweedimensionale secties loodrecht op de plaatgrens. De verticale belastingen van de plaat worden bepaald uit het model dat de beste overeenkomst geeft met doorbuigingsdata uit het Plio-Pleistocene bekken (niveau van ongeveer 3 tot 5 miljoen jaar oud) aan de oostzijde van Italië. Voor zowel een elastische als een diepte-afhankelijke rheologie kunnen variaties in verticale belasting langs de plaatgrens van Italië niet worden opgelost. Daarom kan niet worden geconcludeerd of de hypothese van het lateraal propageren van een scheur in de gesubduceerde plaat overeenkomt met de Plio-Pleistocene doorbuigingsdata of niet.

In hoofdstuk 4 t/m 6 wordt de ontwikkeling in de tijd van subductie en uiteindelijk het afbreken van gesubduceerd materiaal gesimuleerd om te kunnen voorspellen wat de effecten van deze processen op het aardoppervlak zullen zijn. Aangezien het doel is inzicht te krijgen in de ontwikkeling van deze processen wordt niet geprobeerd om een model te vinden dat aan geologische data voldoet. Data kunnen achteraf gebruikt worden om te bepalen of het idee dat ten grondslag ligt aan een model van toepassing kan zijn op een bepaald gebied.

Het is te verwachten dat afbreken van gesubduceerde lithosfeer leidt tot verticale bewegingen van het aardoppervlak, ongeacht of de scheur in de plaat lateraal propageert of niet. Deze verticale verplaatsingen worden vergeleken met verplaatsingen die kunnen optreden gedurende voortgaande subductie. In hoofdstuk 4 worden verticale verplaatsingen van het aardoppervlak die het gevolg zijn van variaties in het subductiesysteem gekwantificeerd. Hiertoe wordt een tweedimensionaal elastisch eindige elementen model gebruikt (hoofdstuk 2). In het eerste model wordt de subducerende plaat aangedreven door een negatief drijfvermogen ten opzichte van de aardmantel en een snelheid aan de zijkant van de modelplaat. De evenwichtstopografie (na ongeveer 2 miljoen jaar) vormt het referentieniveau voor bepaling van verplaatsingen van het aardoppervlak ten gevolge van, onder andere, veranderingen in drijfvermogen van de plaat, snelheid van de platen aan het aardoppervlak en weerstand tegen beweging langs het plaatcontact. De conclusie van dit hoofdstuk is dat verticale verplaatsingen van enkele kilometers (2-4) mogelijk zijn rond een actieve plaatgrens. Beweging van het plaatcontact in de richting tegengesteld aan de subductierichting ('trench retreat') leidt tot hogere topografie van de bovenliggende plaat in het geval dat de terugtrekking veroorzaakt wordt door de beweging van de bovenliggende plaat vergeleken met de situatie waarin terugtrekking het gevolg is van gravitationeel zinken van de subducerende plaat.

De magnitude van de opheffing van het aardoppervlak ten gevolge van het afbreken van gesubduceerde lithosfeer wordt bepaald in hoofdstuk 5. Aangezien een tweedimensionale methode gebruikt wordt is impliciet aangenomen dat de hele gesubduceerde plaat op hetzelfde moment en op dezelfde diepte afbreekt. De topografie van het aardoppervlak die ontstaat gedurende de fase van voortgaande subductie wordt vergeleken met de topografie vlak nadat instantaan afbreken van de plaat is opgelegd. Afbreken van gesubduceerde lithosfeer kan leiden tot opheffing van het aardoppervlak met enkele kilometers. In het geval van niet-migrerende subductie gevolgd door afbreken van de plaat is de maximale opheffing

2-6 kilometer. Dit kan hoger zijn voor de situatie waarin het afbreken voorafgegaan wordt door een fase waarin de plaatgrens zich terugtrekt. De grootte van de opheffing is gevoelig voor de diepte waarop het afbreken plaatsvindt, weerstand tegen beweging langs het plaatcontact na afbreken en visceuze spanningen in de mantel die veroorzaakt worden door het zinken van de afgebroken plaat. De opheffing van het aardoppervlak ten gevolge van het afbreken van gesubduceerde lithosfeer is deels van gelijke grootte als verplaatsingen die optreden gedurende voortgaande subductie.

In Noord-Italië vond in het Laat Mioceen (rond 8-9 miljoen jaar geleden) een opheffing van het aardoppervlak plaats die in plaats en tijd duidelijk te onderscheiden is van de geologische ontwikkeling van het omringende gebied. Voorgaande studies hebben deze opheffing, van 0.5 tot mogelijk 3.5 kilometer, gerelateerd aan het afbreken van gesubduceerde lithosfeer. Met behulp van een numeriek model onder randvoorwaarden die voorgeschreven worden door de geologische ontwikkeling van het gebied, laat hoofdstuk 6 zien dat de opheffing in dit gebied inderdaad het gevolg kan zijn van het afbreken van gesubduceerde lithosfeer. De magnitude van de opheffing van het aardoppervlak duidt erop dat dit proces een belangrijke rol kan hebben gespeeld in de geologische ontwikkeling van het schiereiland Italië.

Acknowledgements

Several people contributed to this thesis, either directly or sometimes more implicit, and I am happy that I have here the opportunity to say thank you. First of all, I would like to thank my promotor Rinus Wortel. During my project, he was first dean of the Earth Sciences Faculty and then director of VMSG, however, with good agenda-management he always could free some time at the moments it was needed. My work benefitted from his critical questions concerning (modelling) assumptions and I appreciate his improvements on the structure of my writing. With Rob Govers I spent a lot of time unravelling the various (numerical) problems I ran into in the course of years. I am impressed by his enthusiastic approach to Earth Sciences and the way he manages to see the bright side of things. I am glad that he became my co-promotor.

Rinus and Johan Meulenkamp together formulated the research project between Stratigraphy and Tectonophysics. This resulted in a challenging and fun project in which geological feedback kept my modelling down to Earth. I thank Johan for his interest in my progress and for updating my geological knowledge on excursions in Greece and Italy. My co-member on this project, Michiel van der Meulen, is thanked for all (scientific) discussions, reading the last chapter, a clear structural/stratigraphic excursion (Italy in four days) and keeping close track of my progress this last year. Thanks to Wim Spakman for answering all questions concerning Mediterranean tomography, his interest in my research and the computation time on mossel. Paul Meijer helped me along on the Andes (chapter 4) and provided his plate rotation routines (chapter 6). I am grateful to the members of my dissertation committee, Profs. Nick Kusznir, Johan Meulenkamp, Roberto Sabadini, Chris Spiers and Reinoud Vissers. The excursion in the Alps led by Reinoud was great fun and might even become of more direct use in the near future. The warm interest and motivation of Chris helped a lot at a certain time.

Chapter 3 benefitted from reviews by G. Panza, P. Waschbusch and an anonymous reviewer. Reini Zoetemeijer provided part of the finite difference code used in chapters 2 and 3. Most figures in this thesis were created with plot-program p, written by Wim Spakman, Marc de Jonge, Rob Govers and Maarten Remkes. I appreciate all efforts of Joop and Theo in helping with computer-related problems.

I like to thank my (ex-)colleague's for the good working atmosphere and all (non-) scientific discussions: Harmen Bijwaard, Eugenio Carminati, Hana Čížková, Charon Duermeijer, Saskia Goes, Jeroen van Hunen, Marc de Jonge, Yvo Kok, Joor Loohuis, Paul Meijer, Marleen Nyst, Dagmar Olbertz, Gualbert Oude Essink, Sandra Richwalski, Axel Röhm, Jörg Schmalzl, Stan Schoofs, Jeroen de Smet and Pièrre Vacher.

Thank you to my friends for all sincere interest and keeping me off my work with nice activities. In the latter Milieudefensie Utrecht was especially quite successful. To my parents I am grateful for their interest and implicit trust. Dear Harald, thank you for all your love, patience and support.

Curriculum Vitae

De auteur van dit proefschrift werd op 30 juli 1970 geboren in Meppel. Voorafgaand aan de middelbare schoolopleiding bezocht ze een jaar een Engelse school op La Palma, Canarische Eilanden. In 1989 werd het VWO diploma aan de RSG in Meppel verkregen. In hetzelfde jaar begon ze aan de studie Geofysica aan de Universiteit Utrecht. Het afstudeeronderzoek betrof het modelleren van de temperatuur- en snelheidsstructuur van de bovenmantel onder Indonesië. In november 1994 werd het doctoraal examen behaald met judicium cum laude. Aansluitend is het onderzoek dat beschreven is in dit proefschrift uitgevoerd aan de faculteit Aardwetenschappen van de Universiteit Utrecht.

de wereld dreijt wel deur
en de mensen ook
ach we zullen 't wel zien

Skik, we zullen 't wel zien